Effect of Interweaving on the Axial Compressive Strength and Modulus of Filament-Wound Composite Cylinders

by

Barry J. Berenberg

Submitted to the Department of Aeronautics and Astronautics
in partial fulfillment of the requirements for the degree of

Master of Science in Aeronautics and Astronautics

at the

MASSACHUSETTS INSTITUTE OF TECHNOLOGY

February 1991

Author.........................
Department of Aeronautics and Astronautics
18 January 1991

Certified by.........................
James W. Mar
Professor, Aeronautics and Astronautics
Thesis Supervisor

Accepted by.........................
Professor Harold Y. Wachman
Chairman, Department Graduate Committee

Effect of Interweaving on the Axial Compressive Strength and Modulus of Filament-Wound Composite Cylinders

by

Barry J. Berenberg

Abstract

The effect of interweaving on the strength and modulus of filament-wound composites is investigated. Simple models based on lamination theory and modifications made for woven fabric composites are developed. More complex models are outlined but not fully developed.

Forty-five composite cylinders with different wind angles and degrees of interweaving were made and tested to failure under axial compression. Test results show that, for wind angles of 30° and 60°, axial compressive strength can be increased by 50% or more simply by changing the interweaving. However, interweaving has little or no effect on cylinders with 45° wind angles.

The failure modes appear to be localized shell buckling for the 30° and 60° cylinders, and outer ply buckling for the 45° cylinders. In all cases, a crack propagates from the initial failure point, and the interweaving seems to act as a barrier to crack growth.

The theoretical models do not adequately predict the effect of interweaving. More complex theoretical models need to be developed. A buckling model which incorporates local imperfections looks promising.

Thesis Supervisor: James W. Mar
Title: Professor, Aeronautics and Astronautics

Acknowledgments

I would like to thank the following people who in some way helped me complete this thesis:

Professor James Mar, my thesis advisor, for both his help and his patience through many delays.

Los Alamos National Laboratory, and in particular the Plastics and Composites Section of MST-7, for their sponsorship of this project. Although the entire group was helpful, I would particularly like to thank Collin Sadler for his general assistance and Charlie Hosford for his help in winding the cylinders. Thanks also to MST-6 for running the tests.

Current and past workers in the MIT Bindery (Kate, Frank, Emmett, Jennifer, MP, Armando, Chris, Stephen, Peter, and all the others) for their friendship and for putting up with me for six years. Just make sure you spell my name correctly when you send this off to be bound.

My parents, Fred and Edie, and my brothers, Scott and Jason.

Contents

List of Figures

7

List of Tables

Nomenclature

English

a undulation dimension

$\mathbf{a}$, $\mathbf{b}$, $\mathbf{d}$ partial inverses of $\mathbf{A}$, $\mathbf{B}$, $\mathbf{D}$

$\mathbf{A}$, $\mathbf{B}$, $\mathbf{D}$ composite stiffness matrices

$\bar{\mathbf{A}}$, $\bar{\mathbf{B}}$, $\bar{\mathbf{D}}$ effective $\mathbf{A}$, $\mathbf{B}$, $\mathbf{D}$ after area averaging

A cylinder cross-sectional area

A_T area of major crossovers

A_{ru} area of repeating unit

b_a, b_c axial, circumferential bandwidths

D cylinder diameter

E, E_{11}, etc. Young's modulus

$\mathbf{E}^*$ plane orthotropic elasticity matrix, principal coordinates

$\mathbf{E}^{[\theta]}$ $\mathbf{E}^*$ in coordinate system at angle θ to principal coordinate system

G, G_{12}, etc. shear modulus

h laminate thickness, $h = k t_{ply}$

h_i y^3 coordinate of ith ply

h_t undulation thickness coordinate

H_i buckling parameters, $i = 1, \ldots, 6$

k number of plies in laminate

k_f, k_m fiber, matrix volume fractions

l_1, l_2 repeating unit dimensions

IDAVG, ODAVG average cylinder inner diameter, outer diameter

ℓ cylinder length

$\ell_{\tilde{\alpha}\beta}$ direction cosine

L distance between bands

m_1 integer part of $\mathcal{M}$

m_2 factor related to repeat

$N_{\alpha\beta}$, $M_{\alpha\beta}$ stress, moment resultants

$N_{11_{cr}}$ shell buckling load, simple models

P_{cr} Euler buckling load

r cylinder radius

R_i buckling parameters, $i = 1, \ldots, 13$

t_{cyl} cylinder thickness

t_{ply} ply thickness

u^0 mid-plane displacement

U Airy stress function

U_i elasticity invariant, $i = 1, \ldots, 5$

V_f fiber payout rate

V_h eye or carriage speed

x^α ply coordinates

y^α laminate coordinates

z^α repeating unit coordinates

Calligraphic

$\mathcal{B}$ bandwidth (tow width)

$\mathcal{D}$ mandrel diameter

$\mathcal{I}$ degree of interweaving

$\mathcal{L}_{eye}$, $\mathcal{L}_f$, $\mathcal{L}_{spin}$ characteristic lengths in winding calculations

$\mathcal{L}_{st}$, $\mathcal{L}_{min}$, $\mathcal{L}_{maj}$ winding pattern dimensions

$\mathcal{M}$ number of mandrel revolutions in one circuit, $\mathcal{M} = m_1 + m_2/\mathcal{N}$

$\mathcal{N}$ number of circuits per layer

$\mathcal{R}$ repeat

$\mathcal{R}_{max}$ maximum repeat

Greek

α, β, γ, ν, ξ, κ, λ, ψ, ρ, ϕ buckling parameters

γ empirical correction factor

Δh height differences around endcaps

$\Delta \ell$ change in cylinder length

$\epsilon_{\alpha\beta}$ strains

$\epsilon^0_{\alpha\beta}$ mid-plane strains

θ wind angle, fiber angle

$\kappa_{\alpha\beta}$ curvatures and twist

$\bar{\mu}$ buckling wavelength ratio

ν, ν_{12}, *etc.* Poisson's ratio

ξ^α shell coordinates

$\sigma_{\alpha\beta}$ stresses

σ_{cl} classical buckling load

$\bar{\sigma}_{cl}$ $\sigma_{cl} = (\bar{\sigma}_{cl} r/2)(a_{1111}/d_{2222})^{1/2}$

ϕ local undulation angle

ω mandrel rotational velocity; buckling parameter

Superscripts/Subscripts

, differentiation

f fiber property

L longitudinal direction (parallel to fibers)

m matrix property

T transverse direction (perpendicular to fibers)

Chapter 1

Introduction

Composite materials are being used in an increasing number of applications. Many industries, from sporting goods to automotive to aerospace, use composites on a regular basis. Of particular interest to the aerospace engineer are composite shells, such as tubes for space trusses, or pressure vessels for aircraft fuselages and manned space vehicles.

When designing a shell, or any structure, one major goal is to minimize weight while maximizing strength. Filament-wound shells should be considered because they are less expensive to manufacture than comparable laminated shells. Both money and time are saved because filament winding is a highly automated process.

In filament winding, a bundle of fibers, or a tow, is laid down on a rotating mandrel. The tow can be purchased pre-impregnated (towpreg) with a thermoset or thermoplastic matrix (dry winding), or it can be impregnated as it is laid down on the mandrel (wet winding). The machine motions can be programmed in advance, and thus the actual manufacturing process requires only minimal supervision. For a more detailed discussion, see [31] and [30].

To achieve the best performance, designers need accurate models of the mechanical and physical properties of the materials they work with. For metals, these models are well developed, and are backed by years of empirical verification. But advanced composites, being a relatively new material, are not as easily analyzed.

To analyze the mechanical properties of a composite laminate or structure, engineers generally turn to Classical Laminated Plate Theory, or CLPT, sometimes modified to include edge effects, interlaminar stresses, or nonlinear effects (see, for example, [40] and Section 4.3). To

15

analyze the strength properties, engineers have several choices. The most common choices are the following criterion [42]:

- Maximum Stress

- Maximum Strain

- Interactive Critera

  - Tsai-Hill

  - Tsai-Wu

  - Chamis

  - Hoffman

Like CLPT, these criterion can also be modified in several ways.

It is important to remember that all of these theories have certain limitations. For the purpose of this study, the most critical limitation is that these theories were developed for laminated composites, with the fibers in each ply lying in a single direction (Figure 1-1). Filament-wound composites are both laminated *and* woven, with the fibers in each ply lying in two *different* directions (see Chapter 3 and Figure 1-2; there are some exceptions in extreme cases).

Does this unique layup affect the properties of the finished composite? The purpose of this thesis is to provide an answer to that question. It does so by looking at the axial compressive strength of filament-wound cylinders. The specific goals of this work are to:

1. Provide a summary of the literature dealing with the structural analysis of filament-wound composites.

2. Develop a mathematical description of the "degree of interweaving."

3. Show experimentally the effects of interweaving on the compressive strength and modulus of filament-wound cylinders.

4. Determine if a simple model, based on CLPT, can be used to predict these effects.

5. Provide recommendations for developing more complex models in future projects.
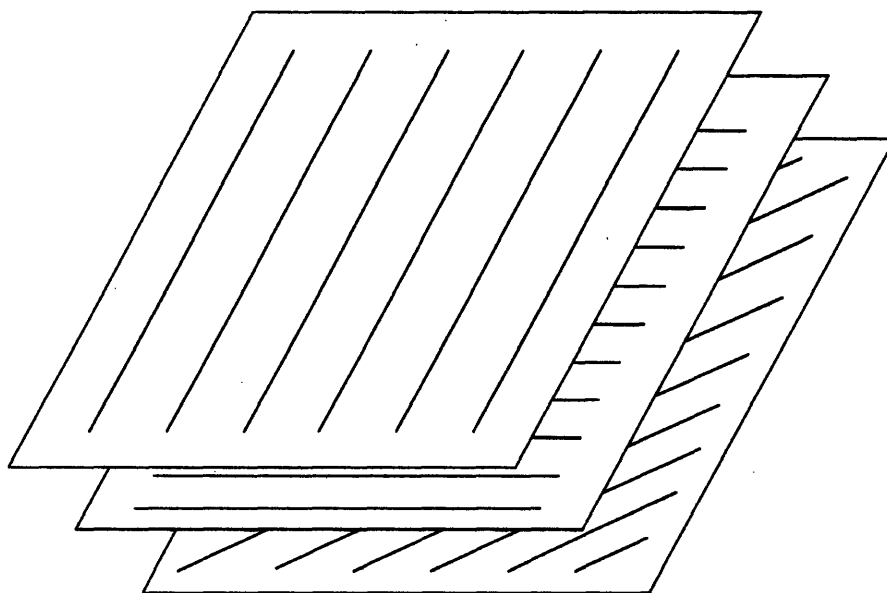
Figure 1-1: Laminated Composite Showing Fiber Directions in Individual Plies
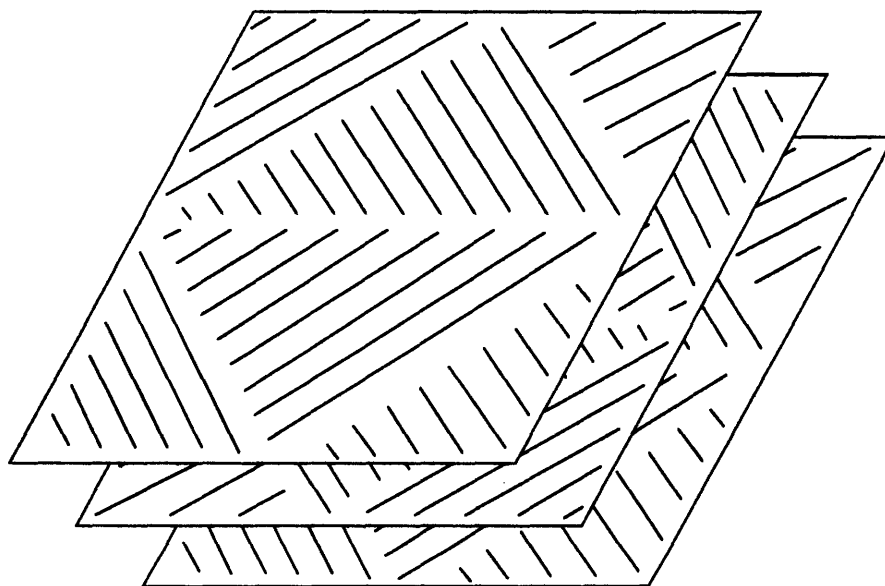
Figure 1-2: Wound Composite Showing Fiber Directions in Individual Plies

Chapter 2 reviews the available literature on wound composites, and answers these questions as well as the current data allows. Chapter 3 then goes into the mechanics of filament-winding, beginning with a description of machine motions and ending with a mathematical description of interweaving.

Chapter 4 presents the theoretical background. Sections 4.2, 4.3, and 4.5 present overviews of micromechanics, lamination theory, and shell theory. Sections 4.4.1 and 4.4.2 contain two methods for modifying lamination theory to include interweaving. Section 4.5 also discusses the different buckling models considered.

Chapter 5 presents the experimental results, and compares these to the theoretical models. Finally, Chapter 6 shows what conclusions can be drawn from these results, and gives recommendations for future work.

Chapter 2

Literature Review

Although articles dealing with composite analysis have proliferated over the past twenty years or so, the number of articles dealing specifically with wound composites has remained small. In this thesis, I have attempted to compile a comprehensive bibliography on wound composites. This is probably not a complete bibliography, but should serve as a good starting point for further research.

2.1   False Assumptions

One of the greatest difficulties in finding articles about wound composites is finding articles which *truly* deal with wound composites. Often, an article with the phrase "filament-wound" in its title will simply treat the wound composite as a laminated composite.

I should point out here that it is possible to wind a cylinder such that it is a true laminate. This is achieved by varying the width of the tow: for a given diameter and wind angle, there is a unique tow width which produces a laminated composite (see Chapter 3). In the articles discussed below, the authors may have been referring to this type of winding. But few if any wound composites are made this way in practice; interweaving almost always remains an important factor.

For example, the title of an early article by Sherrer [35] derives the shell equations for an orthotropic material. The title begins with "Filament-Wound Cylinders ...," but almost immediately makes the assumption that "...each layer [has] a constant angle of wrap ...."

Thus, the analysis more accurately applies to a laminated composite.

Similarly, two other general reports make the same assumption: Pagano and Whitney [29] define "thin-walled cylinder" for anisotropic materials, by finding appropriate ℓ/r and r/h ratios; and Takahashi *et al.* [38] look at the mechanical properties (using CLPT) and strength properties (using the Tsai-Wu criterion) of filament-wound pipes.

Other papers which make the same assumption deal with specific loading conditions. Pagano *et al.* [28] look at tension buckling and the effects of end constraints. Garde and Lakkad [14] match axial buckling loads obtained from experiments to the model in [27]. This model uses an empirical factor obtained from isotropic materials, and contains the warning that "it should be applied with discretion to new and unusual geometries and proportions." Another article on compression, Khitrov and Katarzhnov [22], looks mostly at failure mechanisms and end-cap design.

Pressure and torsional loading have also been written about. Three papers which look at pressure loading are those by Uemura and Fukunaga [41], who use a probabilistic model; by Prater and Hackett [32], who develop a viscoelastic/damage model; and by Kiselev *et al.* [24], who use simple shell equations. The torsional papers have been more concerned with the strength of lap joints, but the modelling of the composite must still be considered. Chon [7] uses laminated shell theory; Hipol [15] uses a finite element method.

An approach which looks promising has been used in strength/weight optimization. Filipenko *et al.* [13] characterize the structure by a set of parameters $\vec{x}_0$ for which an objective function $\Phi(\vec{x})$ takes an extremum value

$$\Phi(\vec{x}_0) = \text{extr } \Phi(\vec{x}) \tag{2.1}$$

Protasov and Ermolenko [33] take a similar approach. Although neither paper mentions interweaving, it may be possible to include interweaving in the set of parameters $\vec{x}$.

Finally, Hoa *et al.* [16] use a finite element approach. Their element allows several layers to be modeled by a single element, resulting in a major reduction in computation time. Although the finite element approach may be a good way to model wound composites (Appendix C), this article again makes the "one layer/one angle" assumption.

This assumption is one of the main reasons that the above articles do not truly apply to

wound composites. Wound composites will have two angles per ply except in the extreme cases, when they are identical to laminated composites.

2.2 Woven Fabrics

Woven fabric composites have two things in common with wound composites: each ply contains fibers lying at two angles; and the composite is woven. But in a woven composite, the fibers are oriented only at angles of $0°$ and $90°$, which makes the regions of interweaving much simpler than in wound composites. Still, models developed for woven composites may give some clues for developing models for wound composites.

Ishikawa [19] presents both a simple analytical and a finite element model of woven fabric composites. The simple model is called a "mosaic" model, and basically ignores the details of the weaving. Changes in fiber angle are assumed to occur abruptly, as shown in Figure 2-1. This model can be applied to wound composites as shown in Figure 2-2 and discussed in Section 4.4.1.

To more accurately model the weaving, Ishikawa and Chow [21] develop the fiber undulation model. This is still a one-dimensional model, but it takes into account the curving of the fibers when they are woven. In [18], the same authors slightly refine the undulation model; they also develop the bridging model, a two-dimensional extension of the undulation model. Finally, in [20], they extend the work to hybrid composites—composites formed from two or more types of fibers.

2.3 Wound and Interwoven Composites

The first step in analyzing a wound composite is to describe the machine motions and fiber patterns. Chapter 3 discusses this topic in detail, and some of the references below also cover this subject. Of greater importance, however, are the conclusions reached regarding the behavior of wound composites under different loadings.

Seleznev *et al.* [34] devote their entire article to filament winding patterns. In addition to the simple helical winding covered in this thesis, they also discuss windings where neighboring tows can overlap or have gaps between them, and the even more complicated case where several
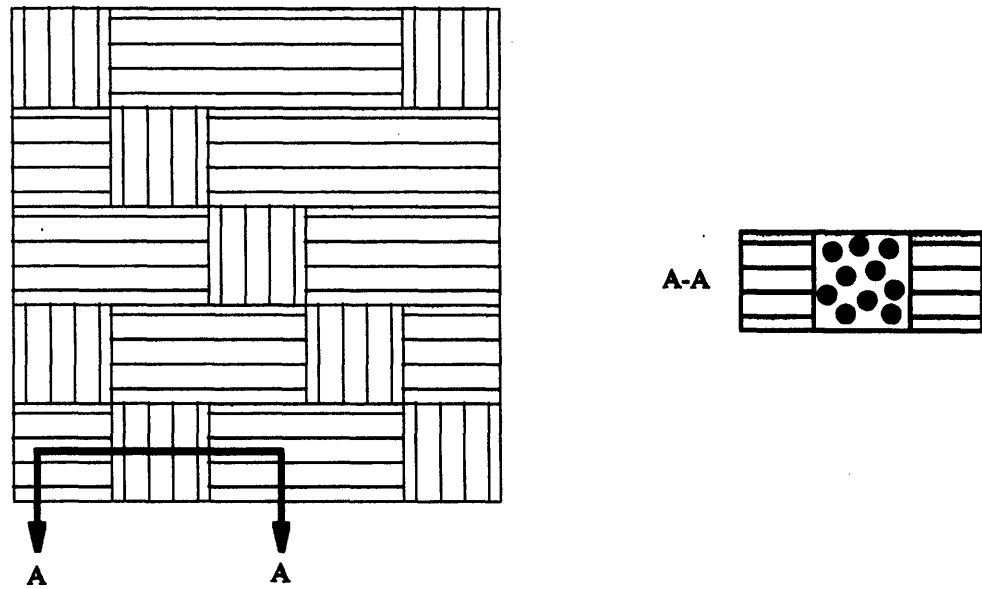
Figure 2-1: Mosaic Model of Woven Composite
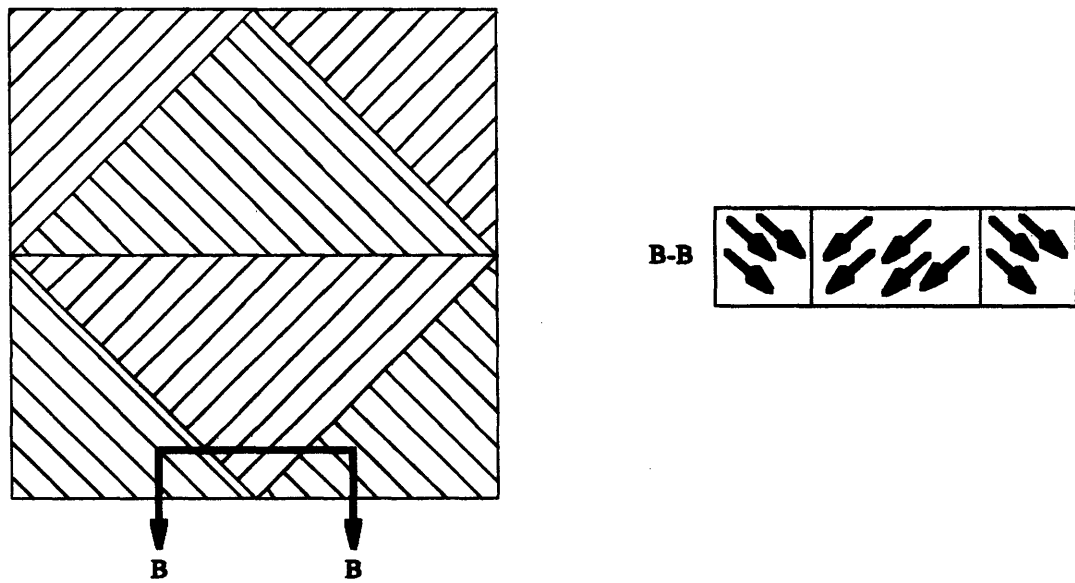
Figure 2-2: Mosaic Model of Filament-Wound Composite

strands are laid down at once (multiple winding eyes).

Zakrzhevskii and Khitrov [44] derive some of the equations found in [34]. More importantly, they empirically document the effect of interweaving on the torsional strength of wound rods. In particular, they found that:

1. As interweaving increases to moderate values, strength also increases because of the creation of a more uniform material and barriers to crack growth.

2. As interweaving approaches its maximum value, the strength begins to decrease because the material contains almost no straight fibers.

3. The magnitude to which interweaving affects torsional strength depends on the failure mode.

4. By carefully selecting the amount of interweaving, the torsional strength of the tubes could be increased by 50%.

Bulmanis and Gusev [2] test filament-wound tubes in axial tension. Though interweaving is mentioned in the paper, they do not document its effects. In a later paper [3], however, they do look at the effects of interweaving on the axial tensile strength. Instead of varying the winding pattern to achieve different degrees of interweaving, they vary the tow width. They conclude that both interweaving and tow width have an effect on the strength of their cylinders. The effects of each factor considered individually cannot be determined from this study, but two of their conclusions are important for this work:

1. Increasing the degree of interweaving causes a reduction in tensile strength; failure occurs in the regions of greatest interweaving.

2. Neither tow width nor interweaving have an effect on the elastic properties of $\pm 45°$ wound tubes.

Brito [1] looks at wound tubes subject to axial tension, internal pressure, and torsion. The main purpose of his study was to find the effect of interweaving on the engineering constants E_L, E_T, ν_{LT}, ν_{TL}, and G_{LT} of wound tubes. He also looks briefly at the rupture strength from internal pressure loading. His important conclusions are:

1. As interweaving increases, the elastic and shear moduli also increase, whereas the Poisson's ratio decreases.

2. The elastic moduli and Poisson's ratios do not satisfy the reciprocity relation

$$\frac{\nu_{LT}}{E_L} = \frac{\nu_{TL}}{E_T} \tag{2.2}$$

   i.e. the elastic matrix is not symmetric. As the interweaving increases, the elastic matrix approaches symmetry.

3. As interweaving increases the behaviour of the wound tube goes from that of an anti-symmetric angle-ply laminate to that of a macroscopically homogeneous and orthotropic material.

That last statement is particularly important, because it will form the basis of the simple model considered in this thesis.

Finally, Eckold [11] develops both strength and elastic models of filament-wound composites. He points out that interweaving has an effect on properties and must be accounted for, and his models incorporate it. Unfortunately, he does use interweaving as an experimental variable. As a result, his results cannot be used for comparison with this work.

This thesis adds to the conclusions of the above authors by looking at filament-wound composites in axial compression. Based on the results above, we should expect interweaving to have some effect on the compressive strength of wound tubes, though it is not clear whether that effect will be positive or negative.

Aside from the loading condition, this thesis also differs from these earlier works in two important ways:

1. More than one wind angle is tested. The studies above, except for [11], examine only a single wind angle.

2. The width of the tow is held constant. In at least one of the studies [3], interweaving is varied by changing the tape width. Thus, the effect of interweaving is separated from the effect of tow width.

Chapter 3

Mechanics of Filament Winding

Modern computer controlled filament winders are capable of winding complex parts with minimal setup effort. Tape-laying machines, and thermoplastic towpreg, now allow winding on concave mandrels. Advanced pattern generation software, such as Silma Corp's CimStation, can even predict layer thicknesses and slippage problems. For this work, however, we will only be discussing simple helical-wound cylinders.

The basic filament winder consists of a control panel, a creel or rack for holding the spools of tows (usually with some kind of tension controller), a set of redirects which terminate in a payout or delivery eye, a resin bath for wetting the tows (if necessary), and a rotating chuck which holds the mandrel (Figure 3-1). As the mandrel rotates, the delivery eye moves back and forth parallel to the axis of the mandrel's rotation, and the tow gets wrapped around the mandrel (Figure 3-2).

As mentioned in the introduction, this method of fabrication creates a much more complicated laminate geometry than does simple lamination. A laminated composite consists of several plies, each ply having a unique fiber angle (Figure 3-3). A wound composite, however, has two fiber angles, $+\theta$ and $-\theta$, in each ply (Figure 3-4). Furthermore, as Figure 3-5 shows, the wound composite has regions where the fibers are interwoven (major crossovers), regions where the fiber angle changes abruptly (minor crossovers), and regions similar to the simple laminated composite.

The effect of all of these regions is a diamond-shaped or triangular pattern on the finished composite, as shown in Figure 3-6. The relative sizes of these triangles depends on a number

of factors, most of which are set by mechanical design requirements. One factor, however, the *repeat*[1] , is chosen arbitrarily, usually by the machine programmer or operator. As shown in the literature review, repeat can have a significant effect on the stiffness and strength properties of a wound composite. Thus, the repeat should be chosen with more care.

In order to derive a rule for choosing the repeat, or at least incorporating it into the analysis, we must first find a way to characterize it; *i.e.* we need a mathematical model which describes the triangular pattern shown above (Figure 3-6). In the past, these models have been developed using the gear ratios of the winders [44]. Most winders now, however, are electrically or hydraulically actuated. A more general approach, which I will employ herein, is to begin with the speeds of the delivery eye carriage and the rotating mandrel.

---

[1]Repeat will be related to degree of interweaving later in this chapter.

Spool
Rack

Redirect

Resin
Bath

Delivery
Eye

Control
Panel

Chuck
(Headstock)

Mandrel

Tailstock

Resin
Bath

Redirects

Delivery
Eye

Fiber
Spools
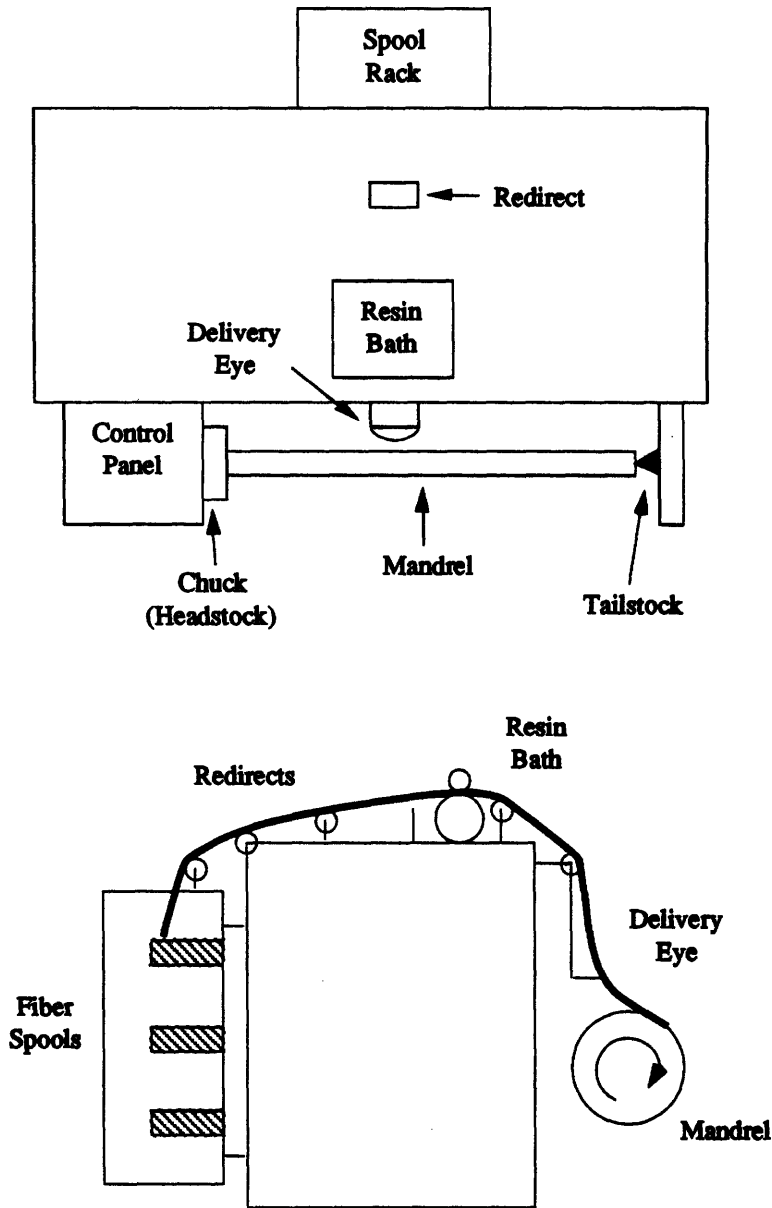
Mandrel

Figure 3-1: Typical Filament-Winder Schematic
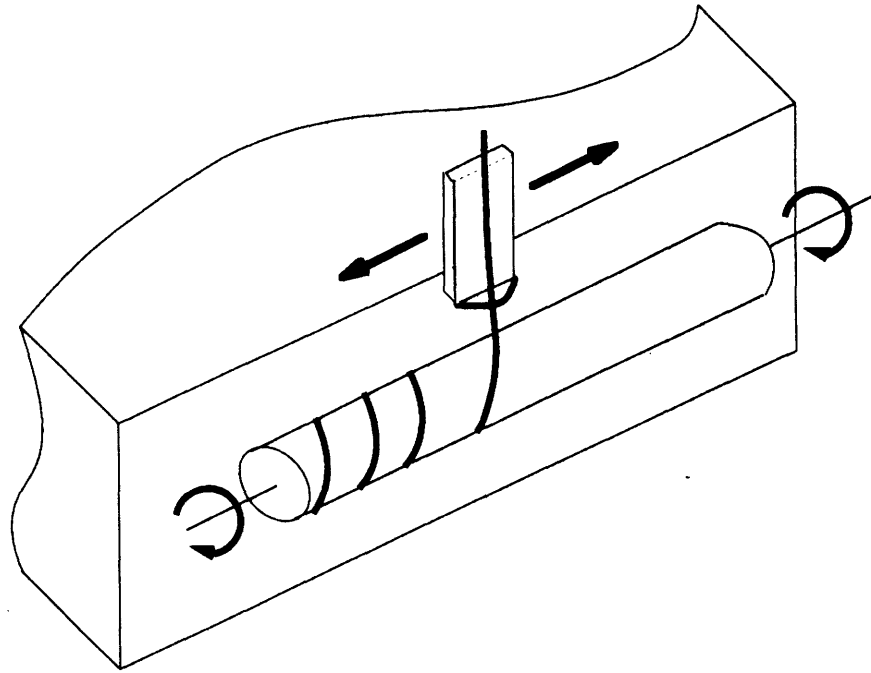
Figure 3-2: Tow Being Wrapped on a Mandrel
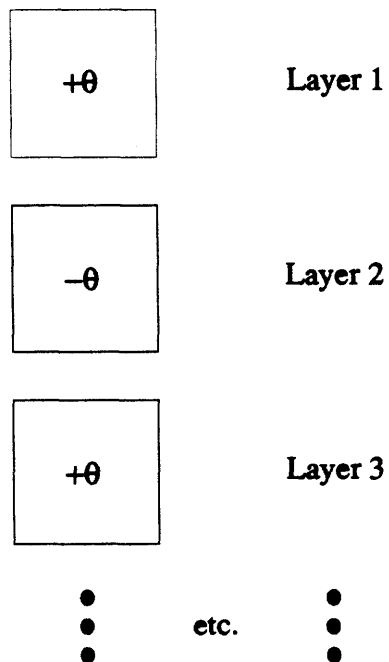
Figure 3-3: Fiber Angles in a Laminated Composite
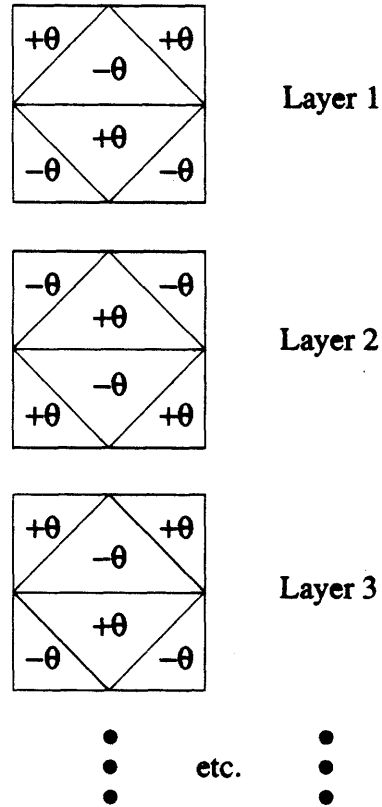
Figure 3-4: Fiber Angles in a Wound Composite
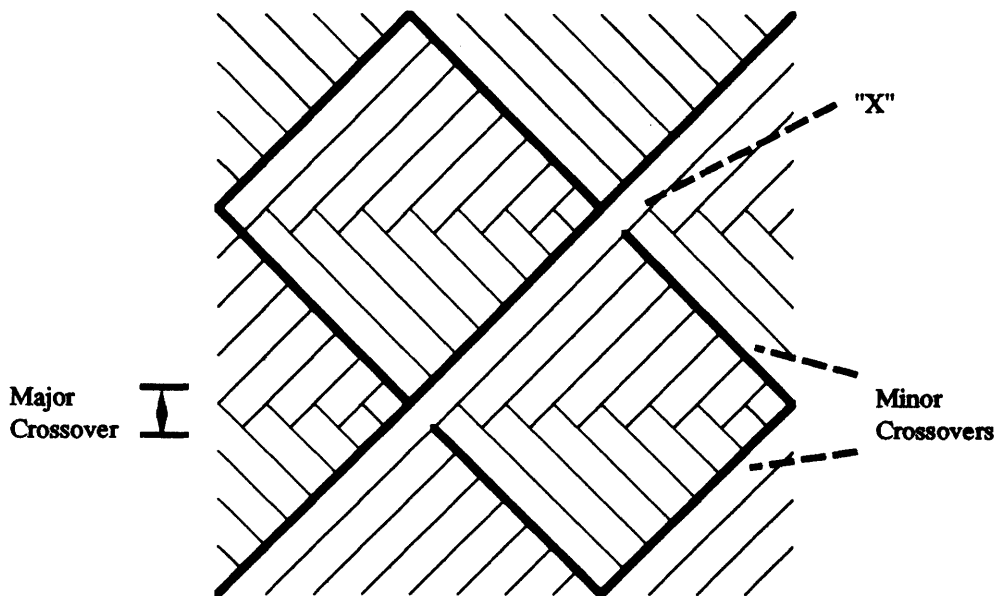
Figure 3-5: Different Regions on a Wound Composite
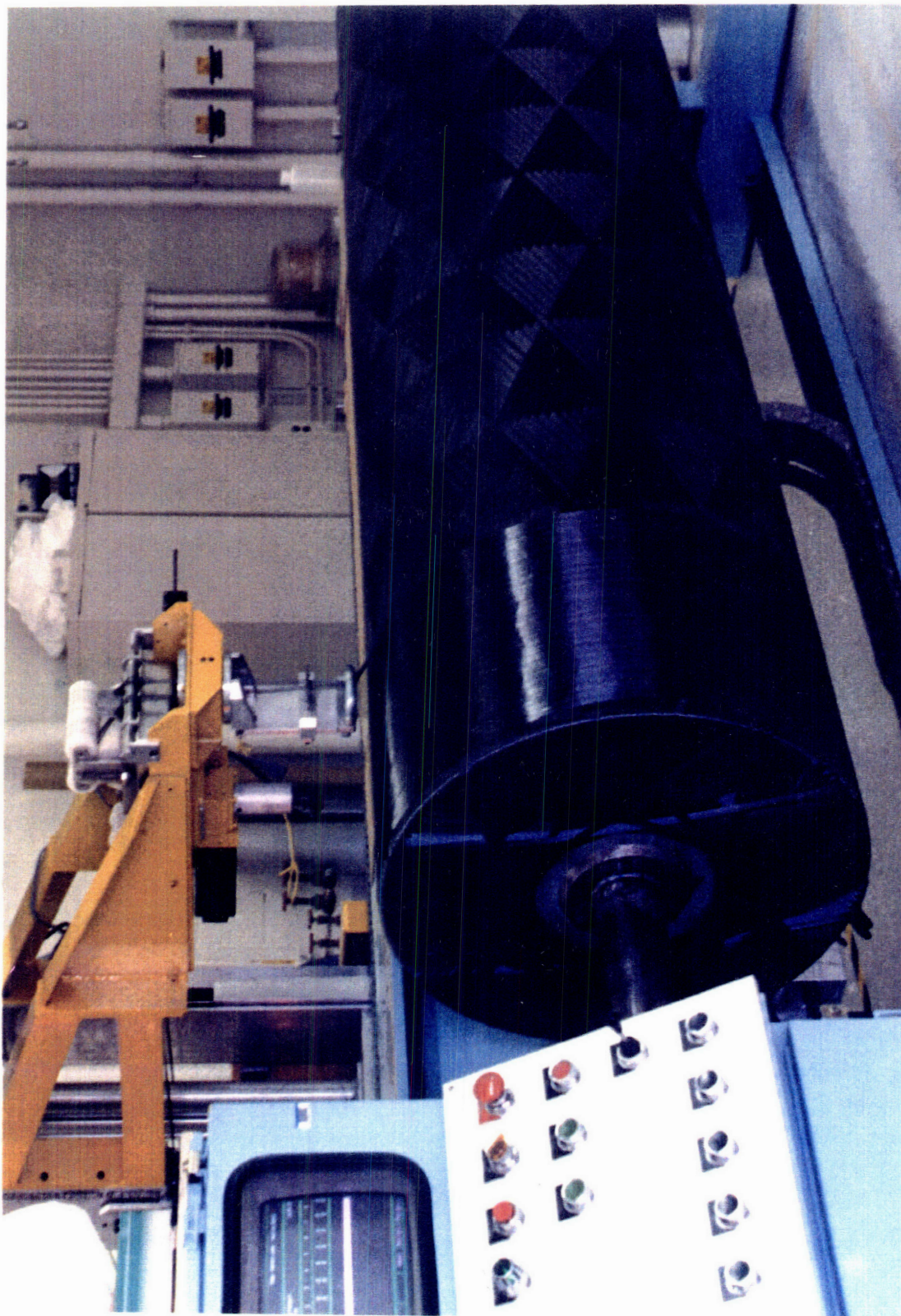
Figure 3-6: Triangular Pattern of a Wound Composite

3.1 Tow Path

We begin by assuming that the part diameter $\mathcal{D}$ (the mandrel outer diameter), the wind angle θ, and the bandwidth or tow width[2] B have already been determined—the former two by design requirements, the latter by the availability of material. Furthermore, we will also choose a payout rate for the tows, V_f. This should be as high as possible to minimize production time, but must be low enough to prevent fiber damage from the redirects and to assure adequate wetting in the resin bath.

To calculate the machine speeds, look at a small piece of the mandrel, flattened out into a rectangle. This mandrel piece contains a single length of tow lying along its diagonal (Figure 3-7), which has been laid down in some arbitrary time t[3]. The length of this tow is $\mathcal{L}_f$[4], and the angle it makes with the mandrel axis is the wind angle, θ. The dimensions of the rectangle are:

- $\mathcal{L}_{eye}$ = linear distance delivery eye has travelled in time t, and

- $\mathcal{L}_{spin}$ = linear distance mandrel has rotated in time t.

In terms of the appropriate speeds,

$$\mathcal{L}_{eye} = V_h t \tag{3.1}$$

$$\mathcal{L}_{spin} = \omega t \left(\frac{1}{2\pi}\right) \pi \mathcal{D}$$

$$= \frac{\omega \mathcal{D} t}{2} \tag{3.2}$$

From Figure 3-7,

$$\tan \theta = \frac{\mathcal{L}_{spin}}{\mathcal{L}_{eye}}$$

$$= \frac{\omega \mathcal{D} t}{2} \cdot \frac{1}{V_h t}$$

---

[2] Bandwidth and tow width are used interchangeably.

[3] This term will soon disappear from the equations. For a simple cylinder, t should include up to one full revolution of the mandrel. For a more complex shape, t should include a portion of the mandrel with an approximately constant diameter, and again less than one revolution. In such a case, this analysis is only approximate. For a more detailed discussion of winding on complex mandrels see, for example, [26] and [43].

[4] In Figure 3-7 and following figures, Roman letters are used in place of calligraphic letters, so that $L_f = \mathcal{L}_f$, etc. This substitution is made solely for software compatibility reasons.
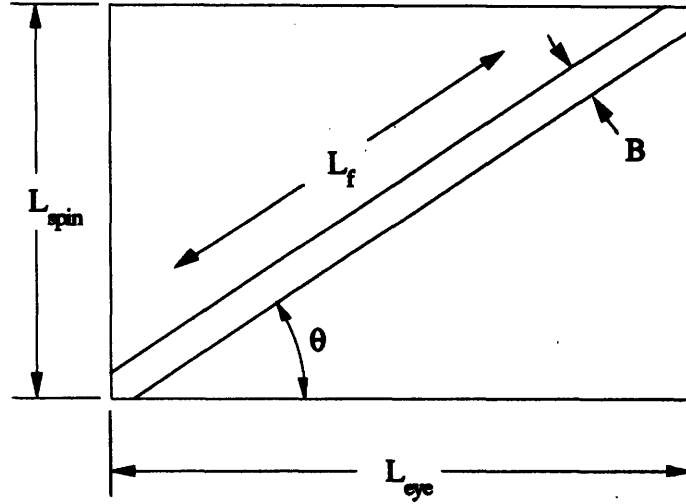
Figure 3-7: Small Portion of Mandrel Containing Single Tow

$$= \frac{\omega \mathcal{D}}{2V_h} \qquad (3.3)$$

Equation 3.3 has two unknowns, ω and $\mathcal{D}$. For a second equation, use either of:

$$\sin \theta = \frac{\mathcal{L}_{spin}}{\mathcal{L}_f} = \frac{\omega \mathcal{D}}{2V_f} \qquad (3.4)$$

or

$$\cos \theta = \frac{\mathcal{L}_{eye}}{\mathcal{L}_f} = \frac{V_h}{V_f} \qquad (3.5)$$

The latter equation immediately gives V_h:

$$V_h = V_f \cos \theta \qquad (3.6)$$

The mandrel rotational velocity is found by substituting equation 3.6 back into equation 3.3:

$$\tan \theta = \frac{\omega \mathcal{D}}{2V_f \cos \theta} \qquad (3.7)$$

or

$$\omega = \frac{2V_f \sin \theta}{\mathcal{D}} \qquad (3.8)$$
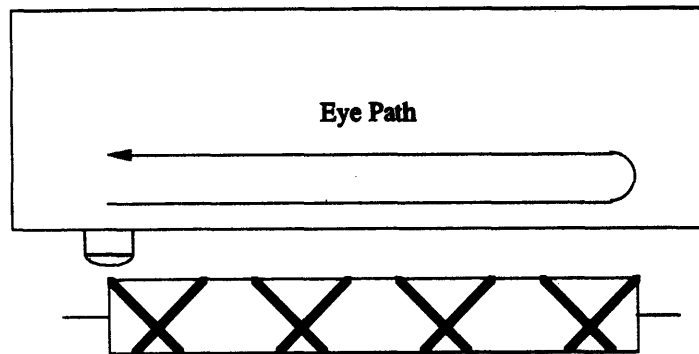
Figure 3-8: Eye and Tow Path After One Circuit

Equations 3.6 and 3.8 completely define the tow path for a single circuit. A circuit is defined as a double-pass of the delivery eye, or the path the eye traverses from one end of the mandrel to the other and back again. Figure 3-8 shows the eye path for a single circuit, and also shows the tow that has been laid down during this circuit.

3.2 Repeat

At this point, we cannot tell what the repeat is going to be. This should be evident from the math, because the repeat does not enter into any of the equations. But to lay down more than one circuit, we must choose a repeat. In practice, the winding software presents a list of repeat values and the operator selects one. But we need to know how that list is generated.

The eye is back at its starting point, and the winding pattern is in the middle of the first turn-around region. The amount of this turn-around, or dwell rotation, must be at least large enough to prevent tow slippage. This may require a dwell rotation greater than 360°, which is more than we need to define repeat. All we really need to know is where the tow path in the next circuit should lie in relation to the tow path from the first circuit. In other words, we are only concerned with the fractional part of the dwell rotation, as measured in mandrel revolutions.

Let $\mathcal{M}$ be the number of revolutions the mandrel makes in one circuit. Then [44]

$$\mathcal{M} = m_1 + \frac{m_2}{\mathcal{N}}$$ (3.9)
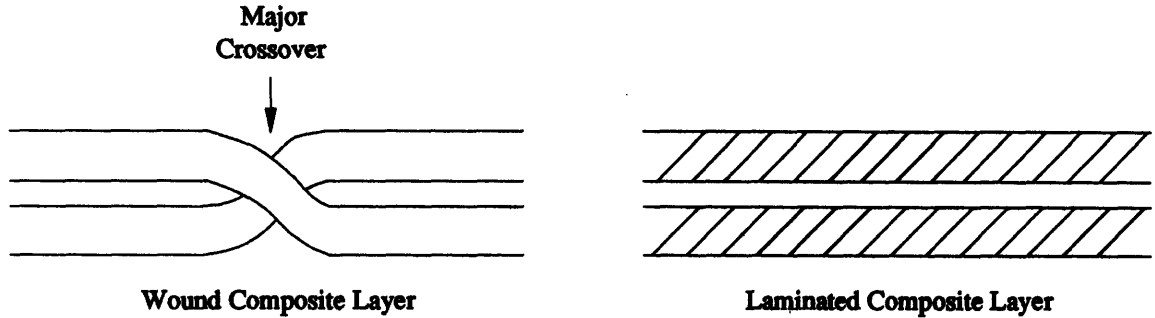
Figure 3-9: Layers in a Wound and a Laminated Composite

, where

- m_1 = integer part of $\mathcal{M}$, and

- $m_2/\mathcal{N}$ = fractional part of $\mathcal{M}$.

By definition, $m_2/\mathcal{N} < 1$. The value of m_1 is unimportant: it is the extra rotation mentioned above, and can be calculated from the machine speeds, part length, and desired turn-around. The values of m_2 and $\mathcal{N}$, however, will be needed, because they lead directly to the repeat.

First, define $\mathcal{N}$ as the number of circuits necessary to completely cover the mandrel, *i.e.* one layer. (Note that one single layer of filament-wound composite corresponds to two layers of laminated composite, as shown in Figure 3-9.) $\mathcal{N}$, like the machine speeds, is independent of the repeat, so we can calculate it immediately.

The bandwidth and wind angle were defined earlier. From these two values, two more widths can be defined: the axial bandwidth b_a, and the circumferential bandwidth b_c (Figure 3-10). They are:

$$b_a = \frac{B}{\sin\theta} \tag{3.10}$$

$$b_c = \frac{B}{\cos\theta} \tag{3.11}$$

Now, Figure 3-11a shows two neighboring tow paths after the first circuit (tow paths in the other direction are not shown for clarity). The distance L between them must be filled by additional bands to complete the layer (Figure 3-11b). Each circuit will put one more band
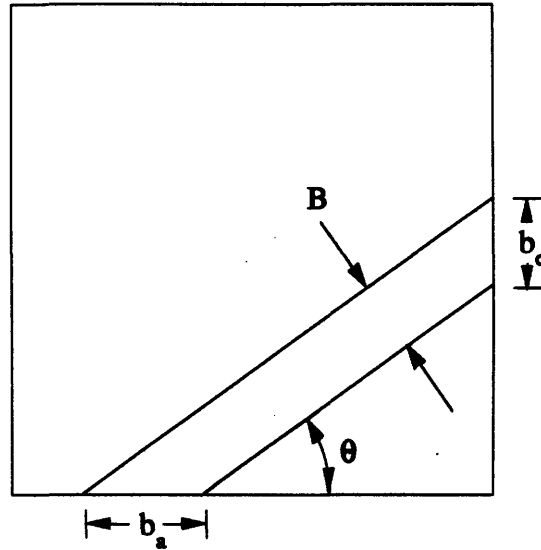
Figure 3-10: Axial and Circumferential Bandwidths

into the gap. Thus,

$$\mathcal{N} = 1 + \frac{L}{b_a} \tag{3.12}$$

where the '1' accounts for the circuit already laid down. The distance L also equals the distance travelled by the eye in exactly one mandrel revolution. From equation 3.1,

$$L = V_h t + b_a \tag{3.13}$$

(The last term is included because L is measured from the inside edges of the two bands, Figure 3-11a.) The time it takes for one mandrel revolution is:

$$n_{revs} = \omega t \frac{1}{2\pi} = 1 \Rightarrow t = \frac{2\pi}{\omega} \tag{3.14}$$

Substituting this value for t and the earlier values for V_h and b_a (equations 3.6 and 3.10) into equation 3.13 gives

$$
\begin{aligned}
L &= (V_f \cos\theta)\frac{2\pi}{\omega} - \frac{B}{\sin\theta} \\
&= (2\pi V_f \cos\theta)\frac{D}{2V_f \sin\theta} - \frac{B}{\sin\theta}
\end{aligned}
$$
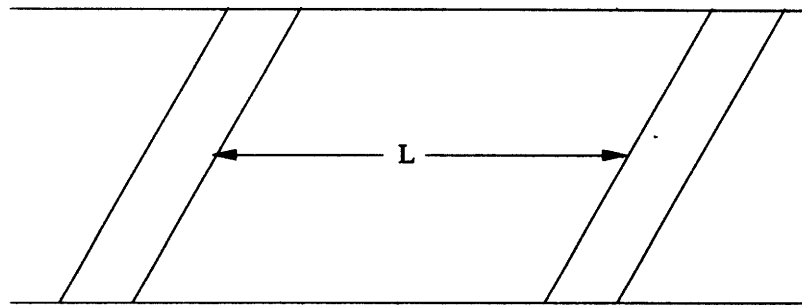
(a) Neighboring tows after first circuit
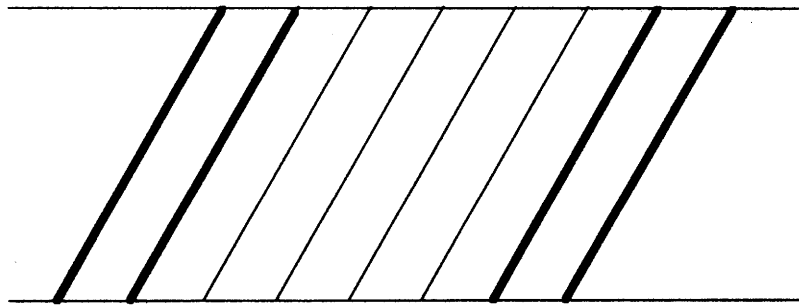
(b) A circuit is complete when "L" has been filled

Figure 3-11: Determination of Number of Circuits Per Layer, $\mathcal{N}$
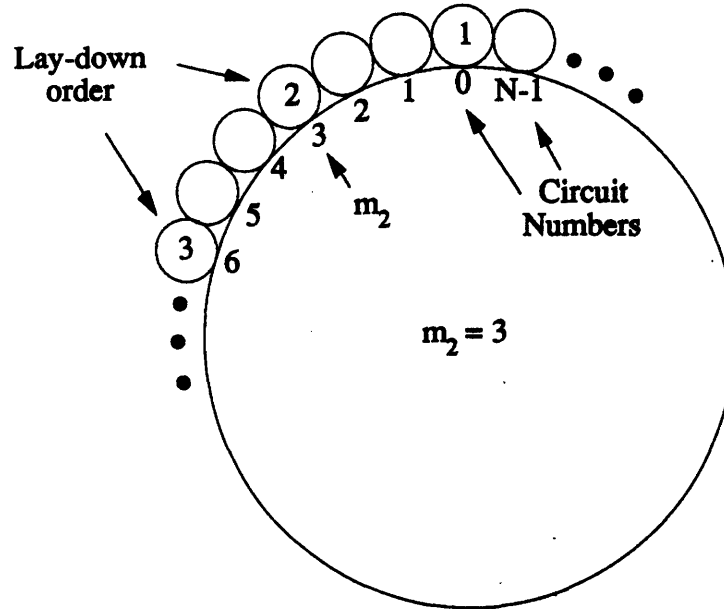
Figure 3-12: Meaning of "Skip" Value, m_2

$$L = \pi \mathcal{D} \cot \theta - \frac{\mathcal{B}}{\sin \theta} \qquad (3.15)$$

Finally, substituting this last equation back into equation 3.12 gives us $\mathcal{N}$:

$$\mathcal{N} = 1 + \left(\pi \mathcal{D} \cot \theta - \frac{\mathcal{B}}{\sin \theta} \right) \frac{\sin \theta}{\mathcal{B}} \qquad (3.16)$$

or, more simply,

$$\mathcal{N} = \frac{\pi \mathcal{D} \cos \theta}{\mathcal{B}} \qquad (3.17)$$

With equation 3.17, the only unknown that remains in equation 3.9 is m_2. Entec [12] calls this value K and defines it as "the number of circuit positions covered from start of first circuit to start of second circuit." Figure 3-12 shows what this means.

When the second circuit begins laying down, the new tow path lies an integral number of b_c's away from the first tow path. The number of these b_c's is defined as m_2. m_2 may be called a "skip" value: it indicates the number of bands (or circuits) in the circumferential direction "skipped" from one circuit to the next. These "skipped" circuits will eventually be filled in, but not necessarily in order.
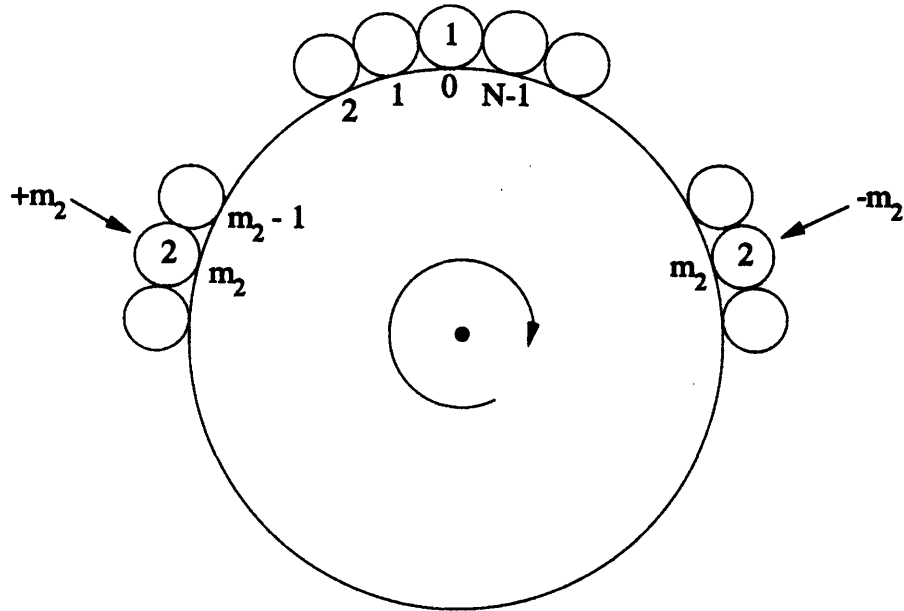
Figure 3-13: Positive and Negative m_2's

Furthermore, m_2 can be either positive or negative. A positive value means the next circuit is laid down "after" the current circuit; a negative value means it is laid down "before" (Figure 3-13). We can write for m_2 that:

$$1 \leq |m_2| < \mathcal{N} \tag{3.18}$$

(m_2 could be equal to 0 or $\mathcal{N}$, but then each tow would lie directly on top of the previous one.)

At last, we get to the repeat. Entec [12] defines the repeat as "the circuit number that will lay next to the first circuit." In other words, the repeat answers the question "How many circuits from now will the tow be laid next to the tow from the current circuit?" It is much easier to see the repeat than to describe it. On a finished part, the repeat will equal the number of diamonds around the circumference, as in Figure 3-6.

Figures 3-14 and 3-15 show mandrels with $\mathcal{N} = 9$ and $\mathcal{N} = 10$, respectively. Also shown are the order the tows are laid down for different values of repeat, $\mathcal{R}$, and m_2. Note that a given m_2—or even an $|m_2|$—does not give a unique $\mathcal{R}$. In fact, for a given $\mathcal{R}$, the ratio $m_2/\mathcal{N}$ can take on one of many values, as shown in Table 3.1.

The general rule is:

Rule 3.1 *If $\mathcal{R} = n$, then $\frac{m_2}{\mathcal{N}} = \frac{1}{n}, \frac{2}{n}, \ldots, \frac{n-1}{n}$ where $n < \mathcal{N}$.*

$\mathcal{R}$	$m_2/\mathcal{N}$
1	1
3	$\frac{1}{3}, \frac{2}{3}$
5	$\frac{1}{5}, \frac{2}{5}, \frac{3}{5}, \frac{4}{5}$
$\vdots$	$\vdots$
n	$\frac{1}{n}, \frac{2}{n}, \ldots, \frac{n-1}{n}$

Table 3.1: Relation Between $\mathcal{R}$ and $m_2/\mathcal{N}$

R	Order	m_2
1	1,2,3,...	2
	2,3,4,...	3
	6,7,8,...	7
3	1,4,7,2,5,8,...	4
	3,6,9,4,7,...	6
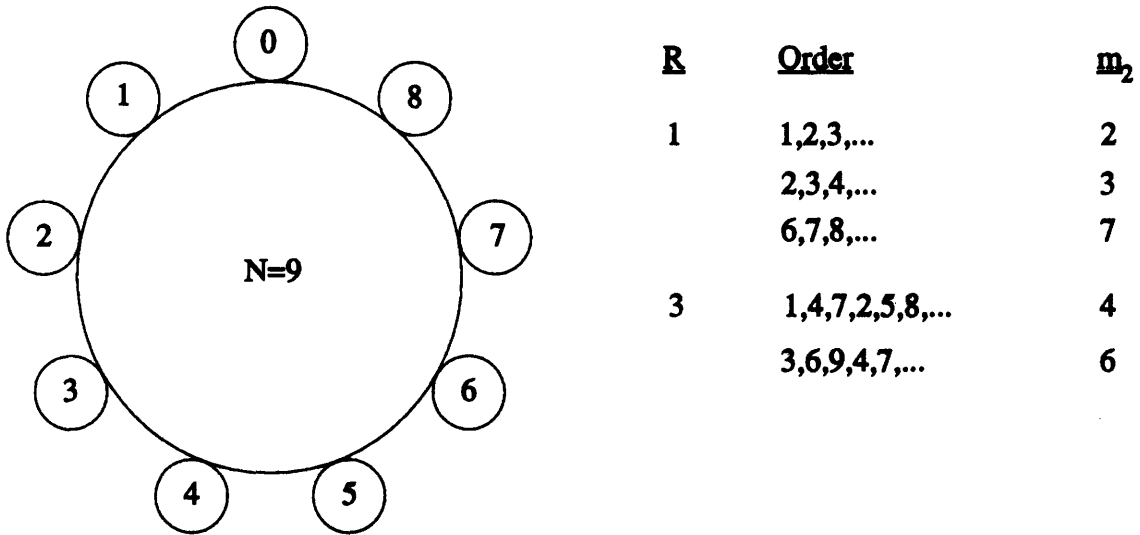
Figure 3-14: Possible Circuit Orders for $\mathcal{N} = 9$

(This rule assumes that for a repeat of 1, $m_2 = \mathcal{N}$, not 1.)

We could simply define $\mathcal{R}$ as the denominator of $m_2/\mathcal{N}$, after the fraction has been put into its simplest form. This isn't a very elegant definition, though. Look again at Figures 3-14 and 3-15. It should be apparent that

$$\mathcal{R} = \frac{\mathcal{N}}{\text{distance between circuits}} \qquad (3.19)$$

where the distance between circuits is given in circuit numbers. Thus, in Figure 3-15 with a repeat of 5, the circuit numbers in the order they are laid down are $\{0,2,4,6,8,0,\ldots\}$, and the

R	Order	m_2
2	2,4,6,...	4
	5,7,9,1,...	7
5	1,6,2,7,...	6
	4,9,5,0,...	9
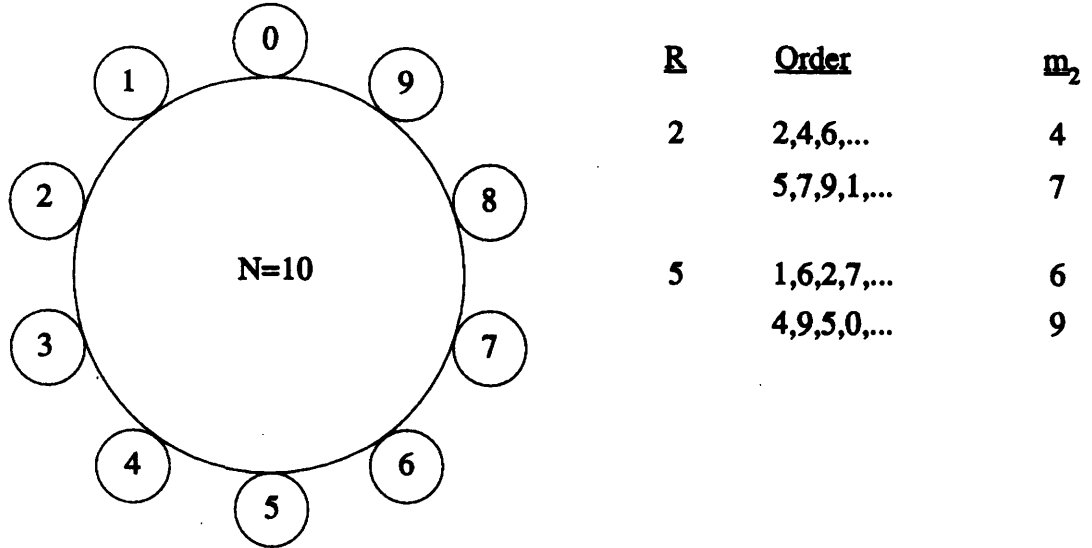
Figure 3-15: Possible Circuit Orders for $\mathcal{N} = 10$

distance between them is 2.

This implies that the set of all m_2's for a given repeat are equivalent. The problem is to figure out which set a given m_2 belongs to. For example, with $\mathcal{N} = 10$, the value of $m_2 = 4$ belongs to the $\mathcal{R} = 5$ set. But with $\mathcal{N} = 8$, the same $m_2 = 4$ belongs to the $\mathcal{R} = 2$ set. A comparison of several different sets and $\mathcal{N}$ values yields the final form of the repeat equation:

$$\mathcal{R} = \frac{\text{lcm}(m_2, \mathcal{N})}{m_2} \tag{3.20}$$

where $\text{lcm}(m_2, \mathcal{N})$ stands for the least common multiple of m_2 and $\mathcal{N}$.

3.3   Pattern Definition

The winding path has now been completely defined. Before going on to the strength and elasticity analysis, two more variables will be needed. These two variables depend on the earlier work in this chapter, but do not themselves affect the winding path.

Refer back to Figure 3-6, which shows the triangular pattern on the composite. Again, the number of "X's" (or diamonds) around the circumference equals the repeat. The distance between the minor crossovers equals $(\mathcal{N} - 1)\mathcal{B}$, and the axial distance between them equals L
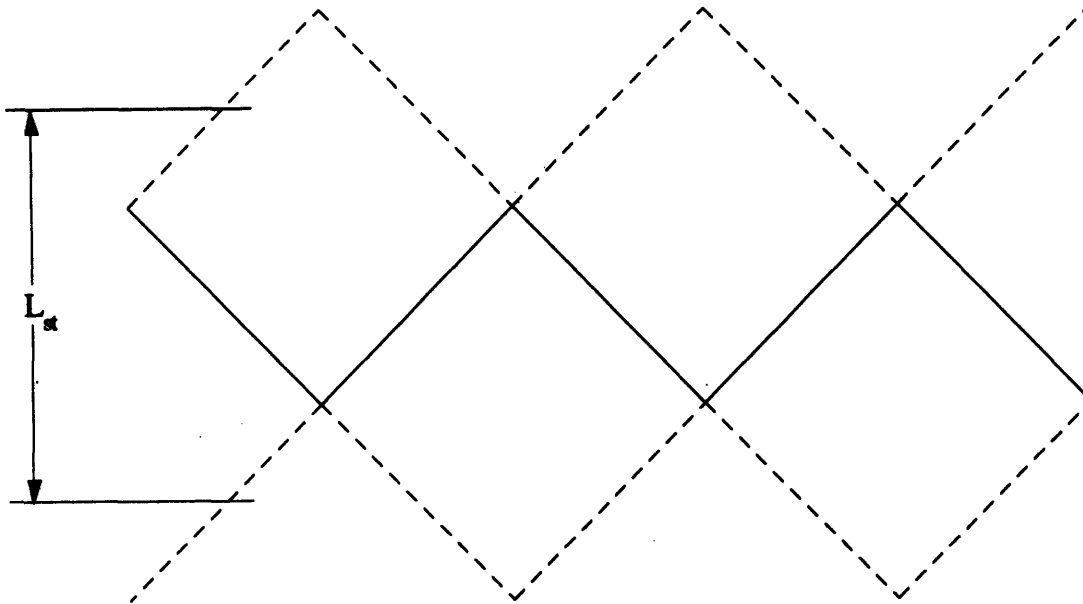
Figure 3-16: Major Crossover

(equation 3.15). But what is the distance between the major crossovers?

We first need to better define where the major crossovers end and the laminar region begins. Figure 3-16 shows a closeup of the region near a major crossover. The major crossover, unlike the minor crossover, is not a smooth line. Rather, it forms a double-sawtooth boundary between two laminar regions. Note that the surface pattern doesn't show the full extent of the major crossover—the dotted lines in Figure 3-16 indicate regions where the sawtooth pattern continues below the surface of the composite.

As shown in [44], the effect of interweaving extends to the midline of the region indicated by dotted lines. Therefore, this line will be considered the boundary of the major crossover. Figure 3-17 shows an even closer view of the one of the "teeth." The height of the major crossover is

$$\mathcal{L}_{st} = 2B \cos \theta \qquad (3.21)$$

For the distance between the major crossovers, take the distance between the top and bottom edges of two closest sawtooth regions plus $\mathcal{L}_{st}$ (Figure 3-18). Figure 3-19 shows a single triangle. Obviously, we also need the length of the base of this triangle. Since it represents one measure of the circumferential distance between minor crossovers, call it $\mathcal{L}_{min}$. Along any
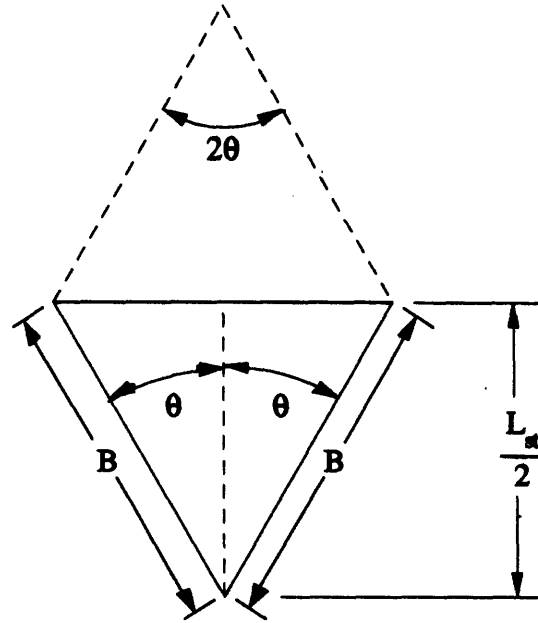
Figure 3-17: Closeup of Major Crossover "Tooth"

major crossover, the number of triangles equals the repeat. Therefore, the base of each triangle contains $\left(\frac{1}{\mathcal{R}}\right)^{th}$ of the part circumference, or

$$\mathcal{L}_{min} = \frac{\pi \mathcal{D}}{\mathcal{R}}$$ (3.22)
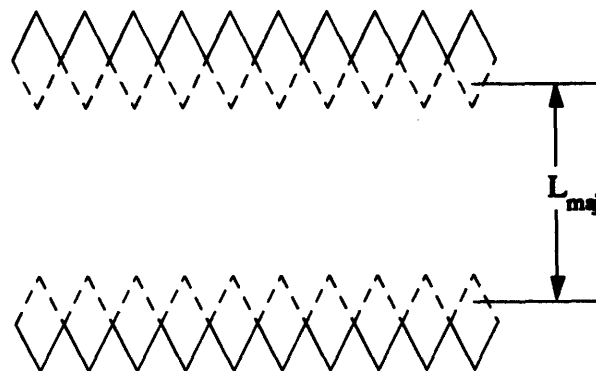
Figure 3-18: Distance Between Major Crossovers, $\mathcal{L}_{maj}$
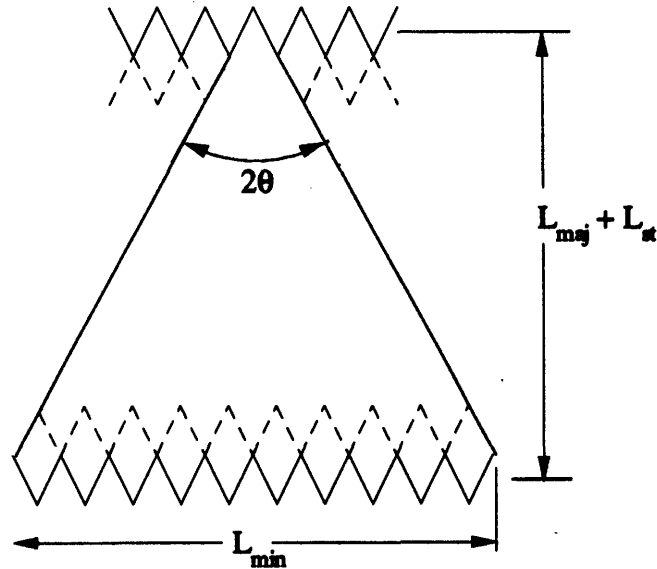
Figure 3-19: Single Triangle

The distance between two major crossovers is then easily found to be

$$\mathcal{L}_{maj} = \frac{\mathcal{L}_{min}}{2} \cot \theta - \mathcal{L}_{st} \tag{3.23}$$

or, substituting equation 3.22 for $\mathcal{L}_{min}$ and equation 3.21 for $\mathcal{L}_{st}$,

$$\mathcal{L}_{maj} = \frac{\pi D}{2\mathcal{R}} \cot \theta - 2B \cos \theta \tag{3.24}$$

$\mathcal{L}_{maj}$ cannot take on any value. If $\mathcal{L}_{maj} = 0$, then neighboring major crossovers will meet. This sets a maximum value for the repeat:

$$\mathcal{R}_{max} = \frac{\pi D}{4B} \csc \theta \tag{3.25}$$

Since this equation is unlikely to produce an integer value, $\mathcal{R}_{max}$ should be taken as the integer portion of equation 3.25.
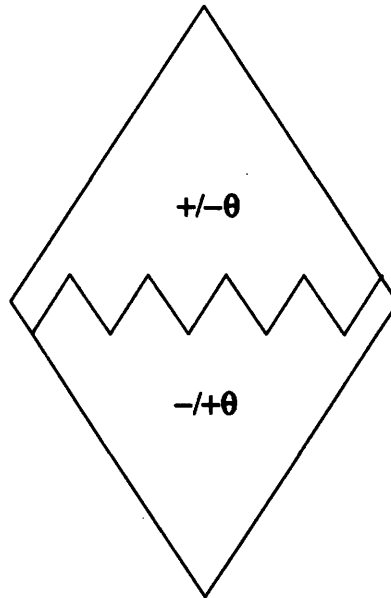
Figure 3-20: Diamond Repeating Unit

3.4 Repeating Unit and Degree of Interweaving

We can now describe the tow path and the triangular pattern which appears on the surface of the wound composite using a just a few variables. One further idea will help with the analysis—a simple repeating unit. Basically, this is just a portion of the triangular pattern which contains all of the information about the entire pattern, and which can be used to reproduce the complete pattern simply by making duplicates of the unit and placing them next to each other on a cylinder.

Two repeating units can be identified. The first is a diamond separated into two triangles, one triangle of layup $[\pm\theta]$, the other of layup $[\mp\theta]$ (Figure 3-20). The diamond is divided in two by a major crossover, and its four sides are minor crossovers. The surface pattern is formed by placing the diamonds so they share each of their sides with a neighbor (Figure 3-21).

The second repeating unit is a rectangle, which actually contains one of the diamond repeating units. Portions of neighboring diamonds are included to make the unit rectangular (Figure 3-22). Although the layup within the rectangle is more complicated than the diamond, and the rectangle is not bounded by any crossovers, it is easier to form a complete pattern: Simply fill a grid with the rectangular repeating unit, as shown in Figure 3-23.
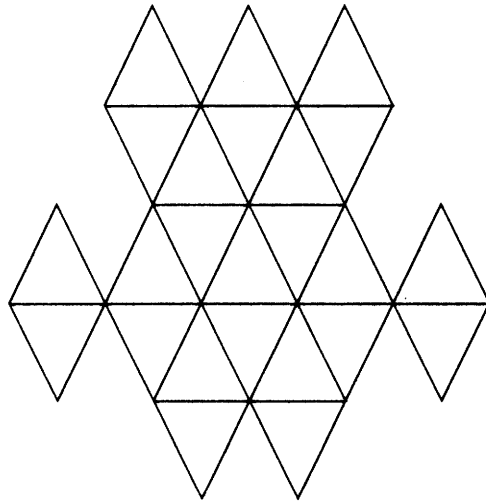
Figure 3-21: Replication of Repeating Diamonds
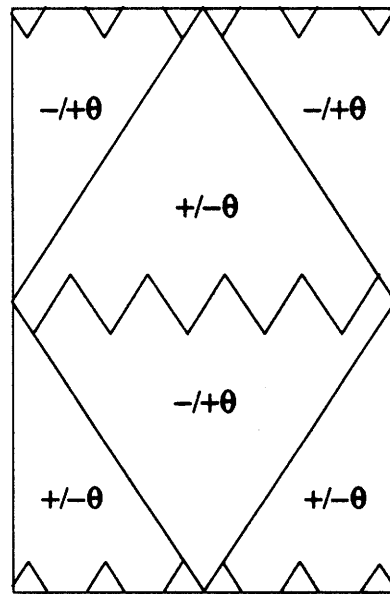
Figure 3-22: Rectangular Repeating Unit
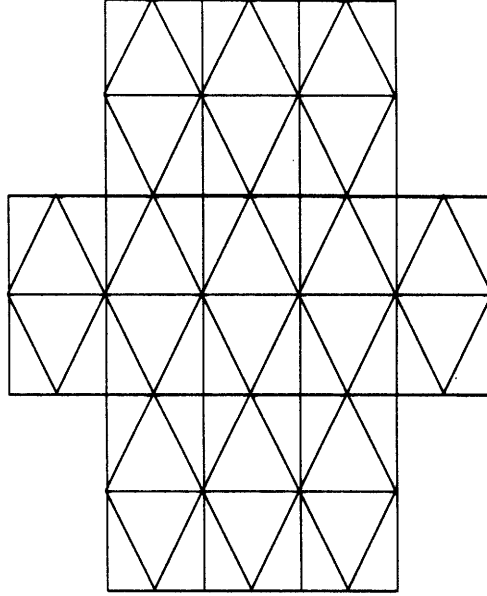
Figure 3-23: Replication of Repeating Rectangles

This latter repeating unit leads to a simple definition of *degree of interweaving*. The phrase "degree of interweaving" has been loosely used in the literature; often it is synonymous with repeat. In this work, a new and precise definition is introduced. Degree of interweaving $\mathcal{I}$ shall be defined as the area fraction of the repeating unit affected by interweaving. Each repeating unit contains one full major crossover and two halves of a major crossover, along the top and the bottom of the repeating unit (Figure 3-22).

The width of the repeating unit is $\mathcal{L}_{min}$, and the height of a full major crossover is $\mathcal{L}_{st}$. Thus, the area taken up by the major crossovers—or regions of interweaving—in a repeating unit is

$$
\begin{aligned}
A_{\mathcal{I}} &= 2\mathcal{L}_{st}\mathcal{L}_{min} \\
&= \frac{4\pi\mathcal{B}\mathcal{D}\cos\theta}{\mathcal{R}}
\end{aligned}
\tag{3.26}
$$

The height of the repeating unit is $2(\mathcal{L}_{maj} + \mathcal{L}_{st})$, so the area of the repeating unit is

$$
\begin{aligned}
A_{ru} &= 2(\mathcal{L}_{maj} + \mathcal{L}_{st})\mathcal{L}_{min} \\
&= \left(\frac{\pi\mathcal{D}}{\mathcal{R}}\right)^2 \cot\theta
\end{aligned}
\tag{3.27}
$$

The degree of interweaving can thus be written as

$$
\begin{aligned}
\mathcal{I} &= \frac{A_{\mathcal{I}}}{A_{ru}} \\
&= \frac{4\mathcal{B}\mathcal{R}\sin\theta}{\pi\mathcal{D}}
\end{aligned}
\tag{3.28}
$$

or as

$$
\mathcal{I} = \frac{\mathcal{R}}{\mathcal{R}_{max}}
\tag{3.29}
$$

Chapter 4

Theoretical Background

The theoretical models developed in this work to predict the behavior of wound composites are based on the theories designed for laminated composites. These latter theories have been presented in numerous other sources: see, for example [40], or any other basic composites text. Only the important results are presented herein.

Most texts use engineering notation. Tensor notation, however, is a more natural choice for shell analysis, so it will be used throughout this work. Normal expansion rules should be followed unless otherwise noted, with Greek indices taking on the values $1, 2$ and Roman indices the values $1, 2, 3$.

4.1   Coordinate Systems and Laminate Notation

Two coordinate systems will be used to describe a laminate: ply coordinates x^α, and laminate coordinates y^α. Figure 4-1 shows these coordinate systems. The ply coordinates are sometimes called L (for longitudinal) and T (for transverse), and are aligned with the fibers. The y^1 and y^2 axes of the laminate system are chosen to align with the laminate principle axes; y^3, sometimes called z, is taken as a thickness coordinate with $y^3 = 0$ at the laminate midplane.

A laminate consists of several plies stacked together, with their fibers oriented in different directions. We need a shorthand method for describing the stacking sequence and orientation of the plies in a laminate. Define $\theta^{[i]}$ as the angle the x^1 axis of the ith ply makes with the y^1
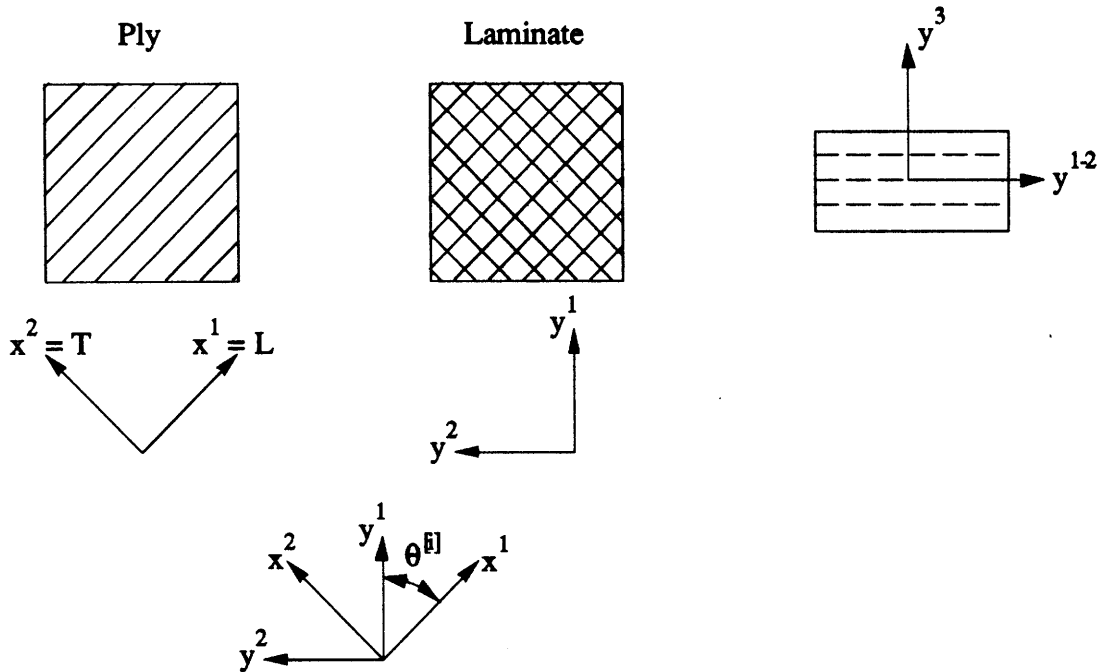
Figure 4-1: Ply and Laminate Coordinate Systems

axis of the laminate (Figure 4-1). A laminate can then be described as

$$\left[\theta_{m_1}^{[1]} / \theta_{m_2}^{[2]} / \cdots / \theta_{m_i}^{[i]}\right]_{nS/T} \tag{4.1}$$

The order of the $\theta^{[i]}$ represent the stacking sequence, with ply one being at the top of the laminate ($y^3 = \max$) and ply k being at the bottom of the laminate ($y^3 = \min$). k represents the total number of plies in the laminate.

The other symbols are defined as follows:

• m_i = number of plies at angle $\theta^{[i]}$ at that position in the laminate;

• $[\cdots]$ = sublaminate;

• n = number of times the sublaminate is repeated;

• S = symmetric laminate; *i.e.* the stack of n sublaminates is reflected about its midplane; and

• T = total laminate.

Code	Expansion
$[0_2^\circ/90_2^\circ]$	$0/0/90/90$
$[\pm 45^\circ]_{2T}$	$45/-45/45/-45$
$[0^\circ/\pm 60^\circ]_S$	$0/60/-60/-60/60/0$

Table 4.1: Examples of Laminate Code

Note that either S or T may be used, but not both. If either m_i or n are not present, they are assumed equal to one. Table 4.1 shows several examples of how this notation is used.

4.2   Micromechanics

Micromechanics is the prediction of composite properties based on the properties of the constituents. Micromechanical models have a reputation for being inaccurate, but with reliable material data they can actually be quite good predictors of composite behavior.

The micromechanical model used herein is a modified rule of mixtures [5]. Fiber properties are denoted by the subscript f, matrix properties by the subscript m. The ply engineering constants are found from

$$
\begin{aligned}
E_{11} &= k_f E_{f11} + k_m E_m \\[2mm]
E_{22} &= \frac{E_m}{1 - \sqrt{k_f}(1 - E_m/E_{f22})} = E_{33} \\[2mm]
\nu_{12} &= k_f \nu_{f12} + k_m \nu_m = \nu_{13} \\[2mm]
\nu_{23} &= \frac{E_{22}}{2G_{23}} - 1 \\[2mm]
G_{12} &= \frac{G_m}{1 - \sqrt{k_f}(1 - G_m/G_{f12})} = G_{13} \\[2mm]
G_{23} &= \frac{G_m}{1 - \sqrt{k_f}(1 - G_m/G_{f23})}
\end{aligned}
\tag{4.2}
$$

where k_f and k_m are the volume fractions of the fiber and matrix respectively, and $k_f + k_m = 1$.

For most of the later analyses two-dimensional models are used, and the constants E_{33}, ν_{23}, G_{13}, and G_{23} are not required. But for the fiber undulation method derived in section 4.4.2, these constants will be needed.

4.3 Lamination Theory

Lamination theory describes the elastic properties of a composite laminate—a stack of laminae or plies. Although wound composites are not true laminates, this theory is still useful in describing them.

4.3.1 Lamina Properties

Lamination theory begins be describing the ply stiffnesses in the ply coordinate system. The stiffnesses of the individual plies are then transformed into the laminate coordinate system. Finally, the transformed stiffnesses of each ply are summed over the laminate and normalized to the laminate thickness. The laminate elastic properties are the result of this process. This section describes the first two steps.

Hooke's Law for a two-dimensional orthotropic problem (a composite ply) in the principal coordinate system is written as

$$\sigma_{\alpha\beta} = E^*_{\alpha\beta\sigma\gamma}\epsilon_{\sigma\gamma} \tag{4.3}$$

or

$$\left\{ \begin{array}{c} \sigma_{11} \\ \sigma_{22} \\ \sigma_{12} \end{array} \right\} = \left[\begin{array}{ccc} E^*_{1111} & E^*_{1122} & 0 \\ E^*_{1122} & E^*_{2222} & 0 \\ 0 & 0 & E^*_{1212} \end{array} \right] \left\{ \begin{array}{c} \epsilon_{11} \\ \epsilon_{22} \\ \epsilon_{12} \end{array} \right\} \tag{4.4}$$

where $\sigma_{\alpha\beta}$ are the stresses and $\epsilon_{\sigma\gamma}$ are the strains. Note that $E^*_{\alpha\beta\sigma\gamma}$ is, of course, symmetric.

The nonzero components of $E^*_{\alpha\beta\sigma\gamma}$ are given by

$$\begin{aligned} E^*_{1111} &= \frac{E_L}{1 - \nu_{LT}\nu_{TL}} \\ E^*_{2222} &= \frac{E_T}{1 - \nu_{LT}\nu_{TL}} \\ E^*_{1122} &= \frac{E_T\nu_{LT}}{1 - \nu_{LT}\nu_{TL}} \\ E^*_{1212} &= G_{LT} \end{aligned} \tag{4.5}$$

Equations 4.5 are in terms of the ply engineering constants.

- $E_L = E_{11}$ = Young's modulus in longitudinal direction,

- $E_T = E_{22}$ = Young's modulus in transverse direction,

- $\nu_{LT} = \nu_{12}$ = major Poisson's ratio,

- $\nu_{TL} = \nu_{21}$ = minor Poisson's ratio = $\nu_{LT} E_T/E_L$, and

- $G_{LT} = G_{12}$ = shear modulus.

These constants can be found using the micromechanics equations of Section 4.2.

Equations 4.4 and 4.5 apply to the ply coordinate system; they must be transformed to the laminate coordinate system to determine laminate properties. $E^*_{\alpha\beta\sigma\gamma}$ could be transformed using the tensor transformation rule for transforming from one orthogonal system to another, i.e.

$$\tilde{E}^{[\theta]}_{\alpha\beta\sigma\gamma} = l_{\tilde{\alpha}\delta} l_{\tilde{\beta}\theta} l_{\tilde{\sigma}\mu} l_{\tilde{\gamma}\rho} E^*_{\delta\theta\mu\rho} \tag{4.6}$$

In this particular expression of the general rule, the corresponding axes of the original and transformed systems are assumed to lie at an angle θ to each other. The expression $l_{\tilde{\alpha}\beta}$ refers to the cosine of the angle between the α axis of the transformed system and the β axis of the original system.

This rule can obviously be quite complicated to use in practice. Thus, most authors adopt a set of invariants to use in performing the transformations. I will use the invariants chosen by Tsai and Hahn [40]:

$$U_1 = \frac{1}{8}[3E^*_{1111} + 3E^*_{2222} + 2E^*_{1122} + 4E^*_{1212}]$$

$$U_2 = \frac{1}{2}[E^*_{1111} - E^*_{2222}]$$

$$U_3 = \frac{1}{8}[E^*_{1111} + E^*_{2222} - 2E^*_{1122} - 4E^*_{1212}]$$

$$U_4 = \frac{1}{8}[E^*_{1111} + E^*_{2222} + 6E^*_{1122} - 4E^*_{1212}]$$

$$U_5 = \frac{1}{8}[E^*_{1111} + E^*_{2222} - 2E^*_{1122} + 4E^*_{1212}] \tag{4.7}$$

The transformed stiffnesses in terms of the invariants are

$$E^{[\theta]}_{1111} = U_1 + U_2 \cos 2\theta + U_3 \cos 4\theta$$

$$E^{[\theta]}_{2222} = U_1 - U_2 \cos 2\theta + U_3 \cos 4\theta$$

$$E^{[\theta]}_{1122} = U_4 - U_3 \cos 4\theta$$

$$E^{[\theta]}_{1212} = U_5 - U_3 \cos 4\theta$$

$$E^{[\theta]}_{1112} = \frac{1}{2}U_2 \sin 2\theta + U_3 \sin 4\theta$$

$$E^{[\theta]}_{2212} = \frac{1}{2}U_2 \sin 2\theta - U_3 \sin 4\theta \tag{4.8}$$

Note that the laminate coordinates do not necessarily coincide with the principal axes of the plies, so $E^{[\theta]}_{1112}$ and $E^{[\theta]}_{2212}$ can be nonzero (and are nonzero for $\theta \neq 0°, 90°$).

4.3.2 Laminate Properties

The individual ply properties must now be combined to describe the laminate. The method used to derive the plate equations will be followed here: although the governing equations differ from shell theory, certain constants do not change when making the transition from plates to shells. At this point, we only need to define these constants and see how they describe the laminate. Later, they can be applied to the curved geometry of a shell.

We begin by making two assumptions about the laminate under an arbitrary loading:

1. In-plane stresses are constant in any lamina; bending stresses vary linearly through any lamina.

2. Strains are constant through the entire laminate.

Thus, the stress and strain state through a laminate may look like that shown in Figure 4-2. We will further assume that all plies have the same thickness, t_{ply}. This assumption is not necessary to the theory, but it is true for all of the laminates studied herein. It also helps simplify the math.

Now, the stress-displacement equations for a plate can be written as [4]

$$\left\{ \begin{array}{c} \sigma_{11} \\ \sigma_{22} \\ \sigma_{12} \end{array} \right\} = \left[\begin{array}{ccc} \bar{E}_{1111} & \bar{E}_{1122} & \bar{E}_{1112} \\ \bar{E}_{1122} & \bar{E}_{2222} & \bar{E}_{2212} \\ \bar{E}_{1112} & \bar{E}_{2212} & \bar{E}_{1212} \end{array} \right] \left\{ \begin{array}{c} u^0_{1,1} - y^3 u_{3,11} \\ u^0_{2,2} - y^3 u_{3,22} \\ u^0_{1,2} + u^0_{2,1} - 2y^3 u_{3,12} \end{array} \right\} \tag{4.9}$$

where all values are given in laminate coordinates and
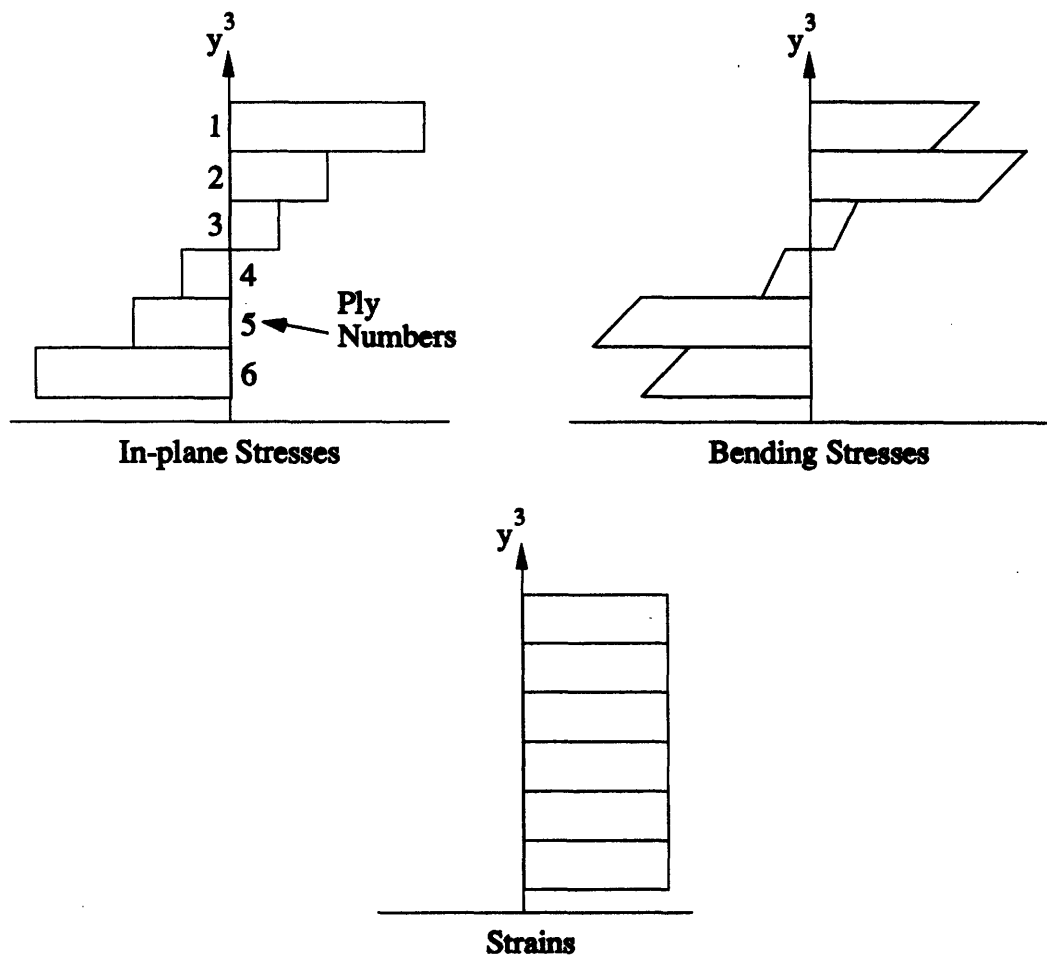
Figure 4-2: Stress and Strain States Within a Laminate

- $\bar{E}_{\alpha\beta\sigma\gamma}$ = laminate stiffness property, yet to be defined;

- u_a = displacements in the y^a direction;

- "0" as a superscript refers to midplane displacements; and

- ",α" as a subscript refers to differentiation with respect to y^α.

Because of the two assumptions made earlier, equation 4.9 can be written as

$$\left\{ \begin{array}{c} \sigma_{11}^{[i,L]} \\ \sigma_{22}^{[i,L]} \\ \sigma_{12}^{[i,L]} \end{array} \right\} = \left[\begin{array}{ccc} E_{1111}^{[\theta]} & E_{1122}^{[\theta]} & E_{1112}^{[\theta]} \\ E_{1122}^{[\theta]} & E_{2222}^{[\theta]} & E_{2212}^{[\theta]} \\ E_{1112}^{[\theta]} & E_{2212}^{[\theta]} & E_{1212}^{[\theta]} \end{array} \right] \left\{ \begin{array}{c} u_{1,1}^0 - y^3 u_{3,11} \\ u_{2,2}^0 - y^3 u_{3,22} \\ u_{1,2}^0 + u_{2,1}^0 - 2y^3 u_{3,12} \end{array} \right\} \tag{4.10}$$

where the superscript $[i, L]$ refers to the stress in the ith ply in laminate coordinates.

It will be easier to work with stress- and moment-resultants rather than simple stresses. Therefore, define the stress-resultants as

$$N_{\alpha\beta} = \int_{-h/2}^{h/2} \sigma_{\alpha\beta}^{[i,L]} dy^3 \tag{4.11}$$

and the moment-resultants as

$$M_{\alpha\beta} = \int_{-h/2}^{h/2} \sigma_{\alpha\beta}^{[i,L]} y^3 dy^3 \tag{4.12}$$

Substituting equations 4.11 and 4.12 into equation 4.9, and considering equation 4.10, we can write

$$\left\{ \begin{array}{c} N_{11} \\ N_{22} \\ N_{12} \end{array} \right\} = \left[\begin{array}{ccc} A_{1111} & A_{1122} & A_{1112} \\ A_{1122} & A_{2222} & A_{2212} \\ A_{1112} & A_{2212} & A_{1212} \end{array} \right] \left\{ \begin{array}{c} u_{1,1}^0 \\ u_{2,2}^0 \\ u_{1,2}^0 + u_{2,1}^0 \end{array} \right\} - \left[\begin{array}{ccc} B_{1111} & B_{1122} & B_{1112} \\ B_{1122} & B_{2222} & B_{2212} \\ B_{1112} & B_{2212} & B_{1212} \end{array} \right] \left\{ \begin{array}{c} u_{3,11} \\ u_{3,22} \\ 2u_{3,12} \end{array} \right\}$$

$$\left\{ \begin{array}{c} M_{11} \\ M_{22} \\ M_{12} \end{array} \right\} = \left[\begin{array}{ccc} B_{1111} & B_{1122} & B_{1112} \\ B_{1122} & B_{2222} & B_{2212} \\ B_{1112} & B_{2212} & B_{1212} \end{array} \right] \left\{ \begin{array}{c} u_{1,1}^0 \\ u_{2,2}^0 \\ u_{1,2}^0 + u_{2,1}^0 \end{array} \right\} - \left[\begin{array}{ccc} D_{1111} & D_{1122} & D_{1112} \\ D_{1122} & D_{2222} & D_{2212} \\ D_{1112} & D_{2212} & D_{1212} \end{array} \right] \left\{ \begin{array}{c} u_{3,11} \\ u_{3,22} \\ 2u_{3,12} \end{array} \right\}$$

$$\tag{4.13}$$

Ply
Number

	y^3		h_0
1			h_1
2			h_2
3			h_3
4			$h_4 \rightarrow y^1\text{-}y^2$
5			h_5
6			h_6
7			h_7
8			h_8
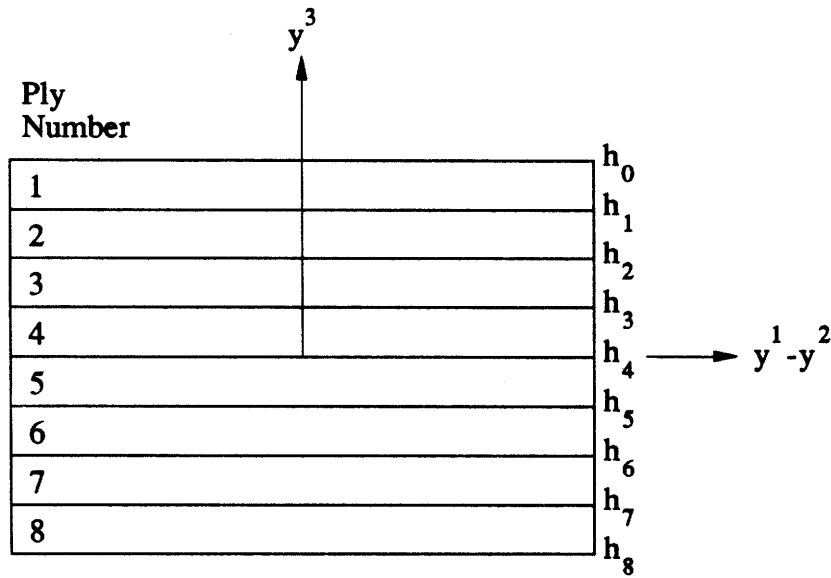
Figure 4-3: Thickness Coordinates

with

$$A_{\alpha\beta\sigma\gamma} = \sum_{i=1}^{k} E_{\alpha\beta\sigma\gamma}^{[-\theta]} (h_{i-1} - h_i)$$

$$B_{\alpha\beta\sigma\gamma} = \frac{1}{2} \sum_{i=1}^{k} E_{\alpha\beta\sigma\gamma}^{[-\theta]} (h_{i-1}^2 - h_i^2)$$

$$D_{\alpha\beta\sigma\gamma} = \frac{1}{3} \sum_{i=1}^{k} E_{\alpha\beta\sigma\gamma}^{[-\theta]} (h_{i-1}^3 - h_i^3) \tag{4.14}$$

where h_i refers to the y^3 coordinate of the lower surface of the ith lamina (Figure 4-3). $\mathbf{E}$ is referenced to $-\theta$ because a positive θ was defined as a clockwise rotation (Figure 4-1).

4.3.3 Special Laminates

In the general case, $\mathbf{A}$, $\mathbf{B}$, and $\mathbf{D}$ will be fully populated. In most applications, however, several of the components will be zero. Let's take a look at these special cases.

Unsymmetric Cross-Ply Laminate Here, all plies are either 0° or 90°, and all laminates are of the form $[0^\circ_m/90^\circ_m]_{nT}$. Special properties of $\mathbf{A}$, $\mathbf{B}$, and $\mathbf{D}$ are:

- $(A, D)_{1111} = (A, D)_{2222}$

- $(A, D)_{1112} = (A, D)_{2212} = 0$

- $B_{1122} = B_{1212} = B_{1112} = B_{2212} = 0$

Antisymmetric Laminate Here, all plies are of the same angle though of different sign, such that $\theta(y^3) = -\theta(-y^3)$. This gives a laminate of the form $[\pm\theta_m]_{nT}$ or $[\mp\theta_m]_{nT}$. Special properties are:

- $(A, D)_{1111} = (A, D)_{2222}$

- $B_{1112} = B_{2212}$

- $(A, D)_{1112} = (A, D)_{2212} = 0$

- $B_{1111} = B_{2222} = B_{1122} = B_{1212} = 0$

The laminar regions of filament-wound composites are antisymmetric.

Symmetric, Balanced Laminate This is the simplest and perhaps most often used laminate. The term balanced means that for every angled ply, *i.e.* plies whose angles are not 0° or 90°, the laminate must have another ply of the same angle but of opposite sign. The laminate is of the form $[0^\circ_{m_1}/90^\circ_{m_2}/ \pm \theta^1_{m_3}/ \pm \theta^2_{m_4}/\cdots]_{nS}$. The 0° and 90° plies do not both have to appear, or neither may appear. If both appear, the θ plies may be absent (a symmetric, cross-ply laminate). Special properties are:

- $A_{1112} = A_{2212} = 0$

- $\mathbf{B} = \mathbf{0}$

Wound composites should not be modeled with unmodified lamination theory, but most papers do exactly that (Chapter 2). The two most common choices are an antisymmetric

laminate, either $[\pm\theta]_{nT}$ or $[\mp\theta]_{nT}$; and a specially orthotropic laminate, with the same stiffness properties as a symmetric, balanced laminate, but consisting of a single ply with fibers in both the $+\theta$ and the $-\theta$ directions.

4.4 Woven Composites and Area Averaging of Properties

4.4.1 Mosaic Model

As a first attempt at analyzing wound composites, let's try an approach which has worked well for woven composites. Recall from Figures 2-1 and 2-2 that the geometry of woven and wound composites are somewhat similar. Both contain regions of interweaving, even though the patterns may be different.

The simplest model of a woven or wound composite is the mosaic model—the fiber angle within a ply is assumed to change abruptly between one laminar region and another. For the wound composite, these regions are bounded by the major and minor crossovers. The sawtooth pattern of the major crossover will be ignored: assume it has straight lines as boundaries.

The mosaic model sums the **A**, **B**, and **D** matrices for each laminar region, and averages them by the fraction of the area they occupy in the repeating unit. That is [20],

$$(\bar{A}_{\alpha\beta\sigma\gamma}, \bar{B}_{\alpha\beta\sigma\gamma}, \bar{D}_{\alpha\beta\sigma\gamma}) = \frac{1}{l_1 l_2} \int_0^{l_2} \int_0^{l_1} [A_{\alpha\beta\sigma\gamma}(z^1, z^2), B_{\alpha\beta\sigma\gamma}(z^1, z^2), D_{\alpha\beta\sigma\gamma}(z^1, z^2)] dz^1 dz^2$$

$$(4.15)$$

where the l_α are the lengths of the repeating unit in the z^α directions (Figure 4-4). Note that the unaveraged **A**, **B**, and **D** are functions of the two repeating unit coordinates.

The wound composite consists of three layup regions: 1) $\pm\theta$; 2) $\mp\theta$; and 3) interweaving. The first two are obviously antisymmetric. Assume the latter matches the specially orthotropic condition mentioned above.

The values for **A** and **D** do not depend on the ply sequence. Thus, **A** and **D** are identical for all three regions. That leaves **B**. In the specially orthotropic case, *i.e.* in the interwoven region, **B** = **0**.

The laminar regions are antisymmetric, and a property of antisymmetric laminates is that
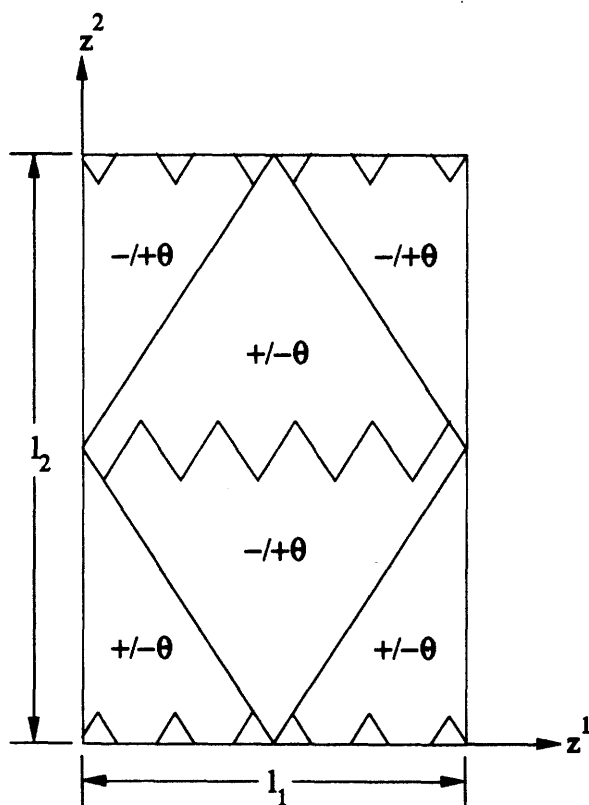
Figure 4-4: Repeating Unit Coordinates

reversing the ply sequence reverses the sign of **B**. Therefore,

$$\mathbf{B}(\pm\theta) = -\mathbf{B}(\mp\theta) \tag{4.16}$$

Because the $\pm\theta$ and $\mp\theta$ regions of the repeating unit occupy the same area, the area average of **B** is **0**. This means that simple area averaging gives a result identical to the specially orthotropic case.

However, the buckling model presented in Section 4.6.2 depends only on the magnitude of **B**, not its sign. Therefore, we should be justified in using the absolute value of **B**. $\mathcal{I}$ equals the area fraction of the repeating unit covered by interweaving. In this fraction of the area, **B** = **0**. In the rest of the area, **B** is simply $|\mathbf{B}|$. Thus, the effective properties of the wound composite by this method would be

$$(\bar{\mathbf{A}}, \bar{\mathbf{D}}) = (\mathbf{A}, \mathbf{D}) \tag{4.17}$$

$$\bar{\mathbf{B}} = (1 - \mathcal{I})|\mathbf{B}| \tag{4.18}$$

4.4.2 Fiber Undulation Method

This method was also originally developed for use with woven composites. The method is similar to the simple area averaging examined above, but the fiber geometry in the region of interweaving is allowed to be more complex. The work in this section is based on [17].

Once again, area averages of **A**, **B**, and **D** are taken. This time, however, the detail of the weaving, or "fiber undulation," in the regions of the major and minor crossovers is accounted for. We accomplish this by assuming a function which describes the undulation of the fibers through the weaving.

This model is shown pictorially in Figure 4-5 (based on the figure in [21]). For the region $a_0 \leq x \leq a_2$, assume an undulation shape such as

$$h(x^1) = \left[1 + \sin\left\{\left(x - \frac{a}{2}\right)\frac{\pi}{a}\right\}\right]\frac{h_t}{4} \tag{4.19}$$

In practice, this function should be based on an actual cross-section of the composite. This information was not available for the cylinders tested in this project; the function above is the
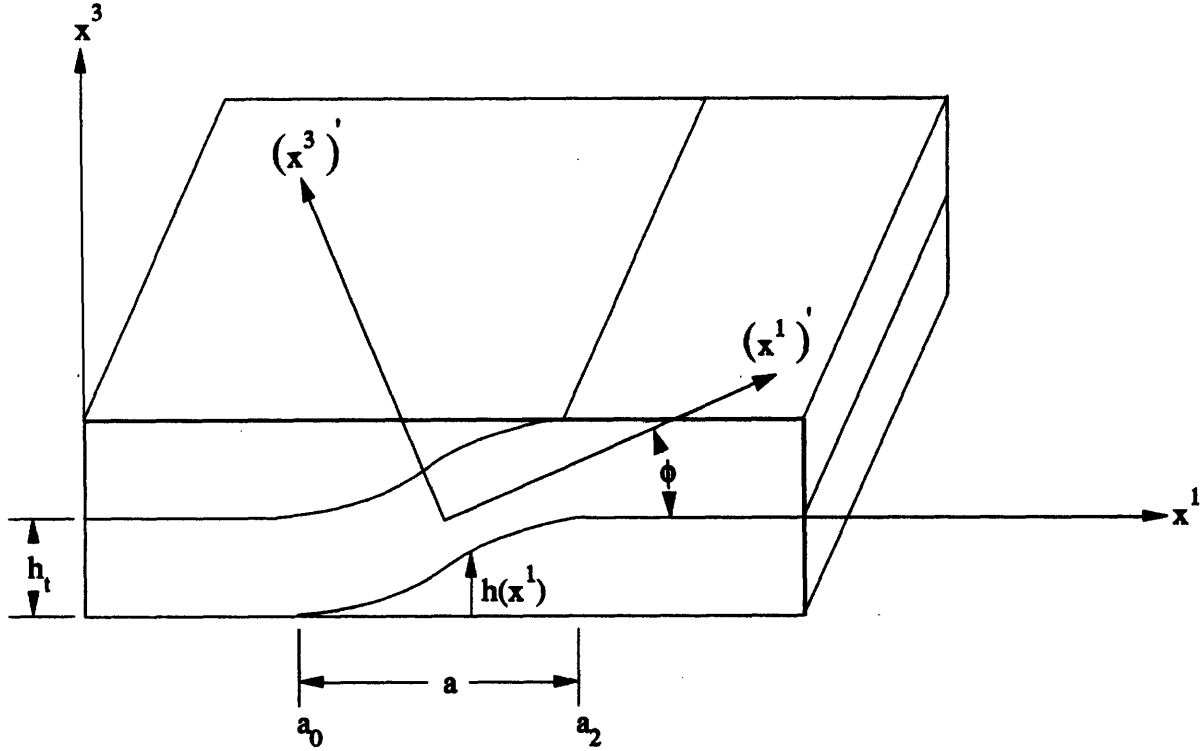
Figure 4-5: Fiber Undulation Model

same one which appears in [17].

Within the undulation region, the fibers make an angle ϕ with the x^1-x^2 plane, where

$$\phi = \tan^{-1}\left(\frac{dh(x^1)}{dx^1}\right) \tag{4.20}$$

Assume ϕ is small, so $\tan^{-1}(\phi) \approx \phi$. Then

$$\phi = \frac{h_t\pi}{4a}\sin\left(\frac{\pi x}{a}\right) \tag{4.21}$$

For $a/h_t = 1.5$ the error in the approximate ϕ is under 10%; for $a/h_t = 2.0$ the error is under 2-3%.

Two methods are now available to find the effective $\mathbf{A}$, $\mathbf{B}$, and $\mathbf{D}$ matrices. Both methods find elastic constants in the local plane of the undulation (the $(x^1)'$-$(x^2)'$ plane) and transform these constants to the laminate plane. The first method, used by Ishikawa and Chou in [21]

and [17], takes the engineering constants in the undulated plane and transforms them into the laminate plane.

The local engineering constants are determined using the micromechanics equations and are assumed equal to the engineering constants of a flat laminate. The transformation equations are then [25]

$$E_{11} = \left[\frac{\cos^4 \phi}{E'_{11}} + \left(\frac{1}{G''_{13}} - \frac{2\nu'_{31}}{E'_{11}} \right) \cos^2 \phi \sin^2 \phi + \frac{\sin^4 \phi}{E'_{33}} \right]$$

$$\nu_{21} = \nu'_{31} \cos^2 \phi + \nu'_{23} \sin^2 \phi$$

$$G_{12} = G'_{12} \cos^2 \phi + G'_{23} \sin^2 \phi$$

$$E_{22} = E'_{22} = E'_{33} \qquad (4.22)$$

The primed constants are those in the undulated plane[1]. These new ply engineering constants are substituted into equations 4.5, a new $\mathbf{E^*}$ matrix is found, and from this the effective $\mathbf{A}$ $\mathbf{B}$, and $\mathbf{D}$ matrices are found.

The second method, also suggested by Ishikawa and Chou in [21], is to directly transform the matrix of elastic constants, thereby bypassing the calculation of the engineering constants. In [21], the transformation is applied to $\mathbf{E^*}$. But $\mathbf{E^*}$ is the plane-strain form of the three-dimensional $\mathbf{E}$ matrix—an out-of-plane transformation is being applied to a plane-strain elasticity matrix[2].

The more accurate method is to calculate the full $\mathbf{E}$ with principal axes in the local undulation plane, transform this matrix to the laminate plane, then apply the plane-strain approximations to get $\mathbf{E^*}$. However, $\mathbf{E}$ is a function of the coefficients of Chentsov and the coefficients of mutual influence of the first and second kind—constants which are usually not known [25]. Therefore, the first method, using only the four basic engineering constants, is the only practical method.

In either case, the effective $\mathbf{A}$, $\mathbf{B}$ and $\mathbf{D}$ are equivalent to the original $\mathbf{A}$, $\mathbf{B}$ and $\mathbf{D}$, except that each *component* (not matrix) is multiplied by a constant. These matrices are then multi-

---

[1]Note that Lekhnitskii's transformation relations ([25], p. 41) are for a rotation about the x^3 axis, whereas the undulation calls for a rotation about the x^2 axis. However, the single ply is specially orthotropic, and the 2 and 3 axes are equivalent.

[2]Perhaps that is why this method appears in [21] but not in the later article [17].

plied by the factor $(1 - \mathcal{I})$ as in equation 4.18 to account for the amount of interweaving. The effect is the same as in the mosaic model, but the modifications to the elastic matrices are more complicated.

4.5 Shell Theory

We now move away from the flat geometry of plates and into the curved geometry of shells. As in Section 4.3, only a brief review of the theory will be presented, and only that part dealing with cylindrical shells will be covered.

4.5.1 Governing Equations

Consider a circular cylinder of radius r. The curvilinear coordinate system which defines its reference or mid-plane surface is (Figure 4-6)

$$
\begin{aligned}
y^1 &= r \sin \xi^2 \\
y^2 &= r \cos \xi^2 \\
y^3 &= \xi^1
\end{aligned}
\tag{4.23}
$$

Next look at the strain-displacement, stress-strain, and equilibrium equations. In all cases, the Donnell approximations [10] are used. The strain-displacement equations are

$$
\begin{aligned}
\epsilon_{11}^0 &= u_{1,1}^0 \\
\epsilon_{22}^0 &= \frac{1}{r} u_{2,2}^0 + \frac{1}{r} u_3^0 \\
\epsilon_{12}^0 &= u_{2,1}^0 + \frac{1}{r} u_{1,2}^0
\end{aligned}
\tag{4.24}
$$

for the strains, and

$$
\begin{aligned}
\kappa_{11} &= u_{3,11}^0 \\
\kappa_{22} &= \frac{1}{r^2} u_{3,22}^0 \\
\kappa_{12} &= \frac{1}{r} u_{3,12}^0
\end{aligned}
\tag{4.25}
$$
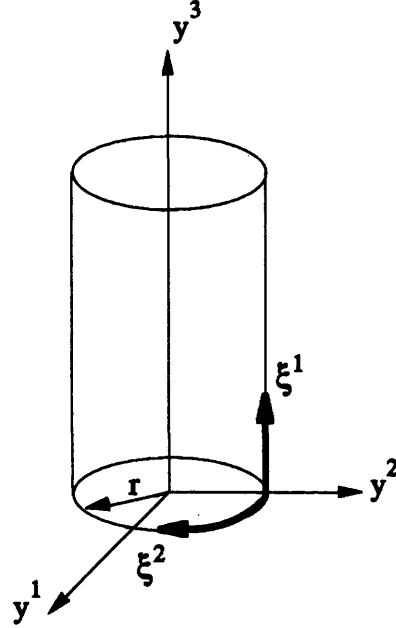
Figure 4-6: Cylindrical Shell Coordinates

for the curvatures and twists. Note that the last of equations 4.24 is in terms of engineering strain, not tensor strain. This may be inconsistent with the notation, but engineering strain seems to be used in most other works.

Now come the six stress-strain relations:

$$
\left\{ \begin{array}{c} N_{11} \\ N_{22} \\ N_{12} \end{array} \right\} = [A] \left\{ \begin{array}{c} u^0_{1,1} \\ \frac{u^0_{2,2}+u^0_3}{r} \\ u^0_{2,1} + \frac{u^0_{1,2}}{r} \end{array} \right\} - [B] \left\{ \begin{array}{c} u_{3,11} \\ \frac{u_{3,22}}{r^2} \\ \frac{2u_{3,12}}{r} \end{array} \right\}
$$

$$
\left\{ \begin{array}{c} M_{11} \\ M_{22} \\ M_{12} \end{array} \right\} = [B] \left\{ \begin{array}{c} u^0_{1,1} \\ \frac{u^0_{2,2}+u^0_3}{r} \\ u^0_{2,1} + \frac{u^0_{1,2}}{r} \end{array} \right\} - [D] \left\{ \begin{array}{c} u_{3,11} \\ \frac{u_{3,22}}{r^2} \\ \frac{2u_{3,12}}{r} \end{array} \right\}
$$

(4.26)

or, more succinctly

$$
\{N\} = [A]\{\epsilon^0\} - [B]\{\kappa\}
$$

$$
\{M\} = [B]\{\epsilon^0\} - [D]\{\kappa\}
$$

(4.27)

Finally, the five equilibrium equations, along with the compatibility equation, are

$$N_{11,1} + \frac{1}{r}N_{12,2} = 0$$

$$N_{12,1} + \frac{1}{r}N_{22,2} = 0$$

$$N_{13,1} + \frac{1}{r}N_{23,2} - \frac{1}{r}N_{22} + q_3 = 0$$

$$M_{11,1} + \frac{1}{r}N_{12,2} - N_{13} = 0$$

$$M_{12,1} + \frac{1}{r}N_{22,2} - N_{23} = 0$$

$$-\frac{1}{r}u_{3,11}^0 + \epsilon_{22,11}^0 + \frac{1}{r^2}\epsilon_{11,22}^0 - \frac{1}{r}\epsilon_{12,12}^0 = 0 \qquad (4.28)$$

q_3 is a pressure loading, normal to the ξ^1-ξ^2 plane. N_{13} and N_{23} are transverse shear terms, and can be eliminated by differentiating the fourth and fifth equations and substituting into the third equation. The result is

$$M_{11,11} + \frac{2}{r}M_{12,12} + \frac{1}{r^2}M_{22,22} - \frac{N_{22}}{r} + q_3 = 0 \qquad (4.29)$$

To get to the governing equations, partially invert equations 4.27 as in [9]:

$$\{\epsilon^0\} = [a]\{N\} - [b]\{\kappa\}$$

$$\{M\} = [b]^T\{N\} - [d]\{\kappa\} \qquad (4.30)$$

where

$$[a] = [A]^{-1}$$

$$[b] = [A^{-1}B] = [aB]$$

$$[d] = [BA^{-1}B - D] = [b^TB - D] \qquad (4.31)$$

Equations 4.30 have six dependent variables, $\{N\}$ and $\{\kappa\}$. However, $\{\kappa\}$ contains only one dependent variable, u_3^0. $\{N\}$ can be reduced to a single dependent variable by introducing the

Airy stress function U such that

$$N_{11} = \frac{1}{r^2}U_{,22}$$

$$N_{22} = U_{,11}$$

$$N_{12} = -\frac{1}{r}U_{,12} \tag{4.32}$$

The strains and moment resultants are now found by substituting equations 4.25 and 4.32 into equations 4.30.The results are

$$\left\{\begin{array}{c} \epsilon^0_{11} \\ \epsilon^0_{22} \\ \epsilon^0_{12} \end{array}\right\} = [a]\left\{\begin{array}{c} \frac{U_{,22}}{r^2} \\ U_{,11} \\ -\frac{U_{,12}}{r} \end{array}\right\} + [b]\left\{\begin{array}{c} u^0_{3,11} \\ \frac{u^0_{3,22}}{r^2} \\ \frac{2u^0_{3,12}}{r} \end{array}\right\} \tag{4.33}$$

and

$$\left\{\begin{array}{c} M_{11} \\ M_{22} \\ M_{12} \end{array}\right\} = [b]^T\left\{\begin{array}{c} \frac{U_{,22}}{r^2} \\ U_{,11} \\ -\frac{U_{,12}}{r} \end{array}\right\} + [d]\left\{\begin{array}{c} u^0_{3,11} \\ \frac{u^0_{3,22}}{r^2} \\ \frac{2u^0_{3,12}}{r} \end{array}\right\} \tag{4.34}$$

The two governing equations are now found be substituting into the equilibrium/compatibility equations. First substitute equation 4.33 into the last of equations 4.28, the compatibility equation, to get

$$a_{2222}U_{,1111} - \frac{2a_{2212}}{r}U_{,1112} + \frac{2a_{1122} + a_{1212}}{r^2}U_{,1122}$$

$$-\frac{2a_{1112}}{r^3}U_{,1222} + \frac{a_{1111}}{r^4}U_{,2222} + b_{1122}u^0_{3,1111}$$

$$+\frac{2b_{2212} - b_{1211}}{r}u^0_{3,1112} + \frac{b_{1111} + b_{2222} - 2b_{3333}}{r^2}u^0_{3,1122}$$

$$+\frac{2b_{1112} - b_{1222}}{r^3}u^0_{3,1222} + \frac{b_{1122}}{r^4}u^0_{3,2222} - \frac{1}{r}u^0_{3,11} = 0 \tag{4.35}$$

for the first of the governing equations. Next, equation 4.34 is substituted into equation 4.29 to get

$$b_{2211}U_{,1111} + \frac{2b_{2212} - b_{1211}}{r}U_{,1112} + \frac{b_{1111} + b_{2222} - 2b_{3333}}{r^2}U_{,1122}$$

$$+\frac{2b_{1112} - b_{1222}}{r^3}U_{,1222} + \frac{b_{1122}}{r^4}U_{,2222} + d_{1111}u^0_{3,1111} + \frac{4d_{1112}}{r}u^0_{3,1112}$$

$$+\frac{2(d_{1122} + 2d_{1212})}{r^2}u^0_{3,1122} + \frac{4d_{2212}}{r^3}u^0_{3,1222} + \frac{d_{2222}}{r^4}u^0_{3,2222}$$

$$-\frac{1}{r}U_{,11} = -q_3 \tag{4.36}$$

for the second of the governing equations.

4.5.2 Special Cases

As was shown in Section 4.3.3, certain laminates eliminate some of the components of **A**, **B**, and **D**. These same laminates also lead to simplifications in the governing equations. We are interested in two cases: the antisymmetric laminate; and the balanced, symmetric laminate.

In the former case, the governing equations reduce to

$$a_{2222}U_{,1111} + \frac{2a_{1122} + a_{1212}}{r^2}U_{,1122} + \frac{a_{1111}}{r^4}U_{,2222}$$

$$+\frac{2b_{2212} - b_{1211}}{r}u^0_{3,1112} + \frac{2b_{1112} - b_{1222}}{r^3}u^0_{3,1222} - \frac{1}{r}u^0_{3,11} = 0 \tag{4.37}$$

and

$$\frac{2b_{2212} - b_{1211}}{r}U_{,1112} + \frac{2b_{1112} - b_{1222}}{r^3}U_{,1222} + d_{1111}u^0_{3,1111}$$

$$+\frac{2(d_{1122} + 2d_{1212})}{r^2}u^0_{3,1122} + \frac{d_{2222}}{r^4}u^0_{3,2222} - \frac{1}{r}U_{,11} = -q_3 \tag{4.38}$$

In the latter case, the governing equations reduce to

$$a_{2222}U_{,1111} + \frac{2a_{1122} + a_{1212}}{r^2}U_{,1122} + \frac{a_{1111}}{r^4}U_{,2222} - \frac{1}{r}u^0_{3,11} = 0 \tag{4.39}$$

and

$$D_{1111}u^0_{3,1111} + \frac{2(D_{1122} + 2D_{1212})}{r^2}u^0_{3,1122} + \frac{D_{2222}}{r^4}u^0_{3,2222} - \frac{1}{r}U_{,11} = q_3 \tag{4.40}$$

4.5.3 Stresses and Strains

The final step is to determine the stresses and strains in the laminate. From [4], the reference surface strains are

$$
\left\{ \begin{array}{c} \epsilon_{11}^0 \\ \epsilon_{22}^0 \\ \epsilon_{12}^0 \end{array} \right\} = \left[\begin{array}{ccc} a_{1111} & a_{1122} & a_{1112} \\ a_{1122} & a_{2222} & a_{2212} \\ a_{1112} & a_{2212} & a_{1212} \end{array} \right] \left\{ \begin{array}{c} \frac{U_{,22}}{r^2} \\ U_{,11} \\ -\frac{U_{,12}}{r} \end{array} \right\}
$$
$$
+ \left[\begin{array}{ccc} b_{1111} - y^3 & b_{1122} & b_{1112} \\ b_{2211} & b_{2222} - y^3 & b_{2212} \\ b_{1211} & b_{1222} & b_{1212} - y^3 \end{array} \right] \left\{ \begin{array}{c} u_{3,11}^0 \\ \frac{u_{3,22}^0}{r^2} \\ \frac{2u_{3,12}^0}{r} \end{array} \right\} \qquad (4.41)
$$

and the stresses in a lamina are

$$
\left\{ \begin{array}{c} \sigma_{11}^{(i)} \\ \sigma_{22}^{(i)} \\ \sigma_{12}^{(i)} \end{array} \right\} = [e^{(i)}] \left\{ \begin{array}{c} \frac{U_{,22}}{r^2} \\ U_{,11} \\ -\frac{U_{,12}}{r} \end{array} \right\} + \left[[f^{(i)}] - y^3 [E^{[\theta]}] \right] \left\{ \begin{array}{c} u_{3,11}^0 \\ \frac{u_{3,22}^0}{r^2} \\ \frac{2u_{3,12}^0}{r} \end{array} \right\} \qquad (4.42)
$$

where

$$
[e^{(i)}] = [E^{[\theta]}][a^{(i)}] \qquad (4.43)
$$

and

$$
[f^{(i)}] = [E^{[\theta]}][b^{(i)}] \qquad (4.44)
$$

4.5.4 Solution of the Governing Equations

The governing equations (4.35 and 4.36) are obviously too complex to solve analytically. A numerical solution must therefore be obtained. The actual solution was considered outside the scope of this thesis, but a brief discussion is included as an aid to further work.

Two possibilities exist for numerical solutions: finite elements, which don't require the governing equations; and finite differences. Finite element solutions are discussed in Appendix C. Finite difference solutions will be covered here.

The properties of the wound composite are a function of position on the cylinder, and depends on the location with respect to the diamond pattern. This variation is easily allowed

for with either element or difference techniques. In the latter, the grid points are spaced such that they "catch" all of the variations in material properties. In this way, the solution accurately reflects the behavior of the material: areas where material properties change rapidly (near the crossovers) are treated differently than areas where the properties are constant. Compare this to the mosaic and fiber undulation models, where the changes are "smeared out" into effective properties.

Another advantage of the discrete solution is that material failure modes can be investigated. A list of common failure models was given in Chapter 1. These models require a knowledge of the stress state at any point on the composite, something not available with the area-averaging techniques.

Finally, the discrete models would also allow modelling of localized imperfections. For example, the void content may be higher near the crossovers than elsewhere on the wound composite, and a high void content would adversely affect the strength of the composite. Including these imperfections would probably improve the accuracy of the model.

Assembly of differencing grids can be automated, much like meshes can be generated for finite element solutions. The major difficulty lies in choosing an appropriate differencing scheme. Calcote [4] presents difference equations for the partial derivatives encountered in the composite plate equations. These same difference equations can be applied to the shell equations without modification. A more complete set of difference equations can be found in [8].

4.6 Stability

When subjected to a loading, a shell can fail in one of three ways: 1) material failure; 2) Euler or column buckling; and 3) shell buckling. The latter two modes will be examined here.

4.6.1 Euler Buckling

The Euler buckling equation for an isotropic column is

$$P_{cr} = \frac{c\pi^2 EI}{\ell^2} \tag{4.45}$$

where c is a constant which depends on the boundary conditions. For a composite column, the Euler equation becomes [11]

$$P_{cr} = \frac{\pi^2 A_{1111} I}{4 k t_{ply} \ell^2}$$ (4.46)

where ℓ is the length of the column and I the moment of inertia of the cross-section.

4.6.2 Shell Buckling

For composite cylinders, shell buckling usually begins with a local instability. Thus, variations in material properties—such as the weavings of wound composites—can be very important. The model selected will have to be adaptable to the variable geometry of wound shells.

We are also looking for a model which gives the proper curve shape for the buckling loads over a range of laminates. All models incorporate an empirical factor to account for the large discrepancies between theory and practice. Therefore, the magnitudes of the predicted buckling loads are not as important as the relative size of the loads from one cylinder to the next.

One of the simplest models is

$$N_{11_{cr}} = \gamma \frac{2}{r} \sqrt{\left(A_{2222} - \frac{A_{1122}^2}{A_{1111}}\right) D_{1111}}$$ (4.47)

where γ is an empirical factor with a recommended value of 0.2 [11]. One immediate problem with this equation is that the buckling load is independent of **B**. Thus, the following laminates all have identical buckling loads: $[\pm\theta]_S$, $[\mp\theta]_S$, $[\pm\theta]_{2T}$, and $[\mp\theta]_{2T}$.

Another model, slightly more complex but with the same problems as the one above is given by Vinson and Sierakowski [42], and is a slightly modified version of the model in [27]. The main difference between these two models is the shape of the failure curves for different layups: Figure 4-7 shows the buckling loads for a $[\pm\theta]_S$ cylinder made from AS4/3501-6.

Two important points about these curves are:

1. Both are symmetric about $\theta = 45°$: the first is exactly symmetric, the second is approximately symmetric.

2. Both models are roughly equivalent in the range $20° \leq \theta \leq 70°$.

These curves have been normalized to have the same value at $\theta = 45°$—about 22,000 psi,
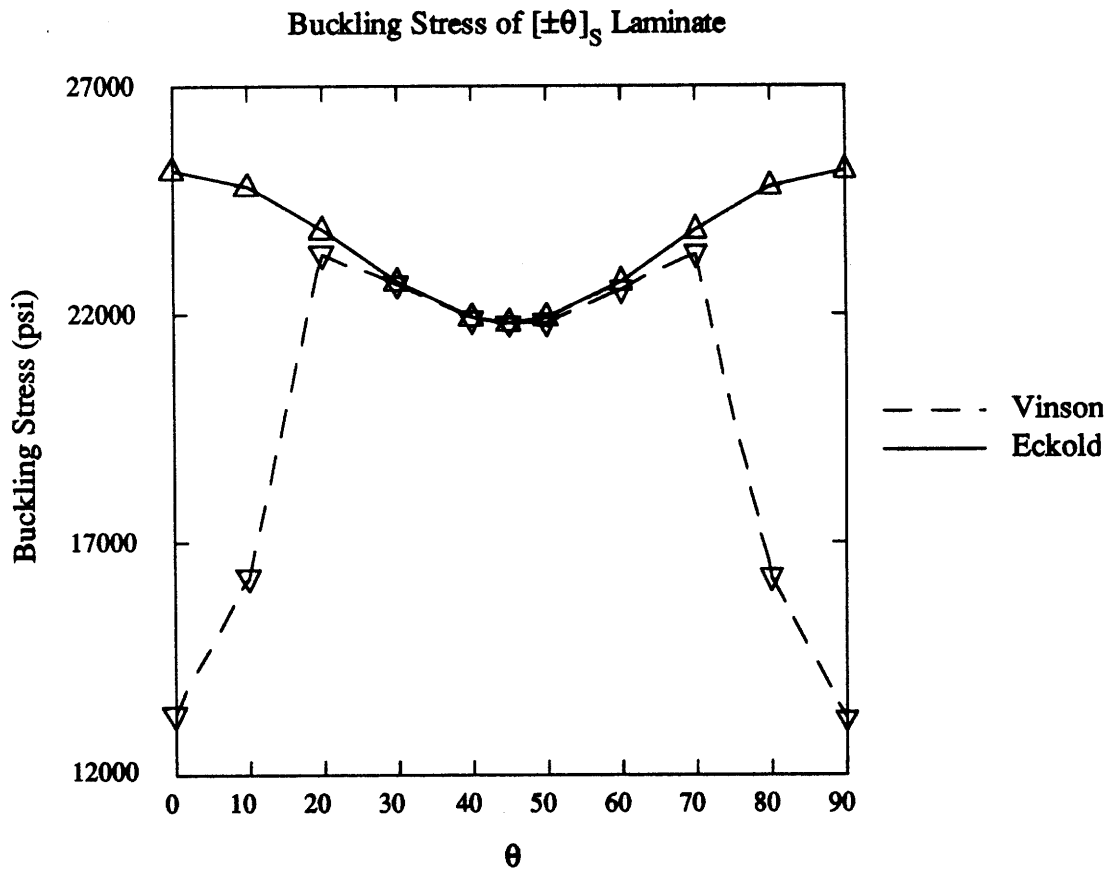
Figure 4-7: Simple Buckling Models

the average value of the experimental failure load of the 45° cylinders. The normalization is accomplished simply by adjusting the empirical factors.

Now let's consider models which allow variations in **B**. There are several choices here, none of them very simple. The two most common seem to be one based on Flügge's equations, presented by Cheng and Ho [6]; and one based on the energy method, presented by Khot [23]. The latter was chosen for this work, because it requires much less computer time than the former.

Khot finds the potential energy of an anisotropic shell subjected to an applied axial end load. Taking the variation of the energy and equating it to zero yields the natural boundary conditions, the equilibrium conditions, and the compatibility condition. An assumed radial displacement is then substituted into the potential energy equation. Finally, the buckling load is obtained by minimizing the total potential energy with respect to the displacement functions.

The classical buckling load is given by the equation

$$\sigma_{cl} = R_1[R_2/\omega + R_3\omega + R_4] + R_5/\omega \tag{4.48}$$

where the R_i are given are functions of the **A**, **B**, and **D** matrices, as shown in Appendix A. This buckling load has been nondimensionalized—the buckling load $\bar{\sigma}_{cl}$ in lb/in is found from

$$\sigma_{cl} = (\bar{\sigma}_{cl}r/2)(a_{1111}/d_{2222})^{1/2} \tag{4.49}$$

where r is the radius of the midplane of the cylinder.

This expression gives buckling loads based on the ratio of axial buckle waves to circumferential buckle waves; the critical buckling load is found by minimizing 4.48 with respect to the constants a (given in Appendix A) and ω:

$$\omega = \left[\frac{R_1R_2 + R_5}{R_1R_3}\right]^{1/2} \tag{4.50}$$

The result of the minimization is

$$R_{11}/\omega + \omega R_{12} + R_{13} = 0 \tag{4.51}$$

Solving equations 4.50 and 4.51 gives the value of a which minimizes equation 4.48, and hence gives the buckling load.

Equations 4.50 and 4.51 can be easily solved using Newton's method. The problem was set up using TK Solver Plus[3] on a Macintosh SE. Solution of the nonlinear equations took under a minute with a reasonable initial guess for a. Results of the calculations are shown in Section 5.3.3.

One important property of this model is that, although it is not independent of **B**, it is independent of the *sign* of **B**. Thus, it gives:

$$\sigma_{cl}(\mathbf{B}) = \sigma_{cl}(-\mathbf{B}) \tag{4.52}$$

This helps justify the use of $|\mathbf{B}|$ in Section 4.4.1 (mosaic model).

---

[3]Trademark of Universal Technical Systems, Inc.

Chapter 5

Results

5.1   Experimental Approach

To test the theories of the previous sections, I examined 45 tubes with 15 different combinations of wind angle and repeat, as shown in Table 5.1. Each tube was given a code number of the form TmR$n.p$, where m was the wind angle, n was the repeat, and p was a number 1 through 3 to give each tube a unique code.

Fifteen tubes of at least 30 in. length were wound on aluminum mandrels, and three 8 in. tubes were cut from each longer tube. Details of the mandrel preparation and the input files for the winding patterns are presented in Appendices B and D. All of the tubes were made from Hercules AS4/3501-6, 12K tow-preg. Table 5.2 shows the material properties of this composite for a 65% fiber volume fraction. These properties were calculated using the micromechanics equations of section 4.2 and the constituent properties shown in table 5.3.

Code	Wind Angle	Repeat	Code	Wind Angle	Repeat	Code	Wind Angle	Repeat
T30R1.1-3	30	1	T45R1.1-3	45	1	T60R1.1-3	59	1
T30R3.1-3	30	3	T45R3.1-3	45	3	T60R3.1-3	61	3
T30R5.1-3	30	5	T45R5.1-3	45	5	T60R5.1-3	61	5
T30R7.1-3	30	7	T45R7.1-3	46	7	T60R7.1-3	61	7
T30R9.1-3	30	9	T45R9.1-3	45	9	T60R9.1-3	61	9

Table 5.1: List of Tubes

Property	Value
E_L (Msi)	22.317
E_T (Msi)	1.397
ν_{LT}	0.249
ν_{TL}	0.01559
G_{LT} (Msi)	0.962

Table 5.2: Properties of AS4/3501-6, 65% V_f

Fiber Properties		Matrix Properties	
E_L (Msi)	34	E (Msi)	0.62
E_T (Msi)	2	ν	0.34
ν_{LT}	0.2	G (Msi)	0.231
G_{LT} (Msi)	4		

Table 5.3: Constituent Properties

The tests consisted of simple axial compression to failure, and were performed on an MTS 880. Simple compression grips were used, with a pivoting platen as the top grip (Figure 5-1). Aluminum endcaps were bonded to the tubes to prevent brooming of the cylinder ends and to give a more even loading. Appendix B contains design information for the endcaps.

Special care was taken to insure that the ends of the tubes were as close to parallel, and as square to the cylinder walls, as possible, to prevent any bending moments from being introduced. Before testing, each tube was placed on a granite table and the height around the edge of the endcap measured (Figure 5-2). The differences between the high and the low measurements were noted, and are listed in Table 5.4. In most cases, the difference is less than 0.010 in.

Load and stroke were recorded for all tests. Two axial extensometers were also used in the first test, of tube T60R3.1. This tube had the greatest difference in measured height around the endcap—21.0×10^{-3} in. The extensometers were placed at the mid-length of the tube, below the high and low measurement points. The slopes of the extensometer readings were nearly identical, so a bending moment was not being introduced. Since the height differences of the other tubes were not as severe as this one, the extensometers were not used for the remaining
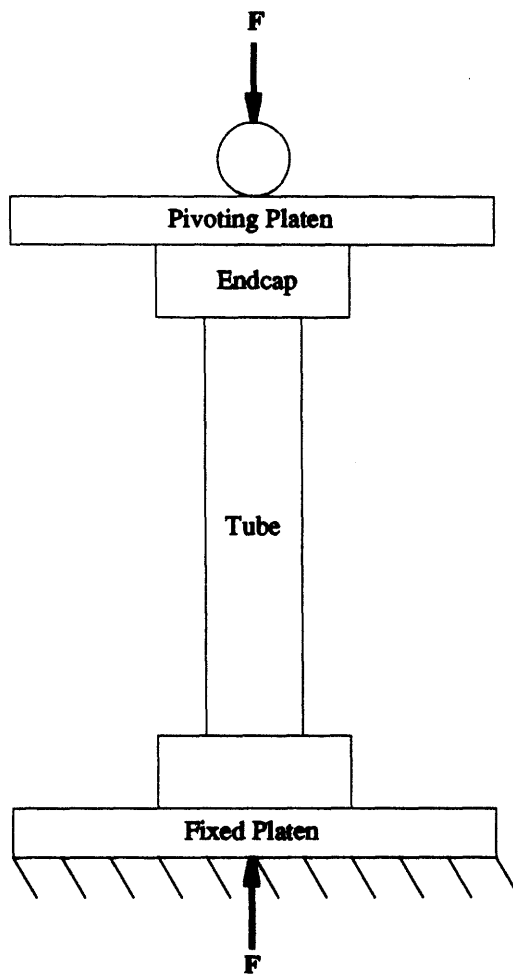
Figure 5-1: Test Fixture Schematic
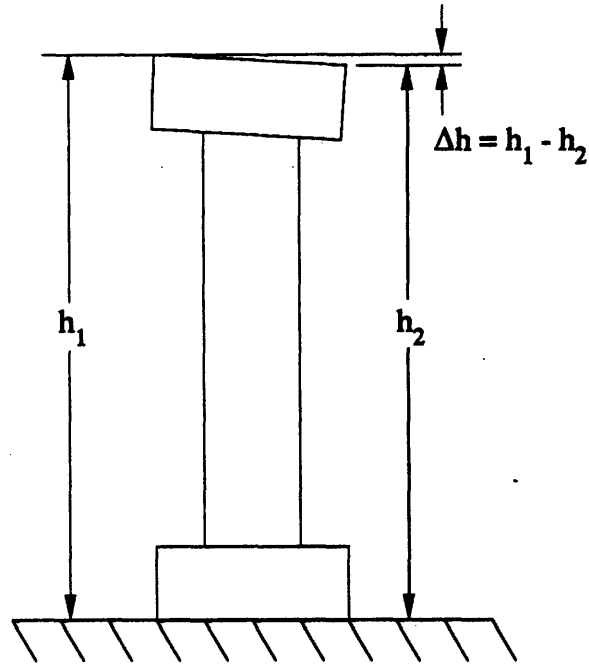
Figure 5-2: Measuring Heights of Tubes with Endcaps

Tube	Δh^a	Tube	Δh	Tube	Δh
T30R1.1	5.5	T30R1.2	2.0	T30R1.3	3.0
T30R3.1	14.0	T30R3.2	2.5	T30R3.3	4.5
T30R5.1	4.0	T30R5.2	2.5	T30R5.3	8.0
T30R7.1	2.5	T30R7.2	4.5	T30R7.3	4.0
T30R9.1	8.0	T30R9.2	6.5	T30R9.3	4.5
T45R1.1	6.5	T45R1.2	4.0	T45R1.3	6.0
T45R3.1	8.0	T45R3.2	16.0	T45R3.3	22.0
T45R5.1	6.0	T45R5.2	4.5	T45R5.3	11.0
T45R7.1	6.5	T45R7.2	6.0	T45R7.3	9.5
T45R9.1	10.0	T45R9.2	4.0	T45R9.3	5.5
T60R1.1	3.5	T60R1.2	5.0	T60R1.3	3.5
T60R3.1	21.0	T60R3.2	2.0	T60R3.3	9.0
T60R5.1	9.0	T60R5.2	4.5	T60R5.3	3.0
T60R7.1	4.5	T60R7.2	5.0	T60R7.3	8.0
T60R9.1	5.5	T60R9.2	8.5	T60R9.3	3.5

$^a\Delta h$ in 0.001 in.

Table 5.4: Height Differences Around Endcaps

tests[1].

5.2 Physical Characterization

One major problem with using a prepreg tow is determining the bandwidth. Dry tows have a
fairly constant bandwidth, and tend to spread out as they are laid down on the mandrel, which
helps to minimize the variations. Prepreg tows, however, have varying bandwidths, and the
tow does not spread out as it is laid down.

For the material used here, the typical bandwidth was about 0.16 in, but varied from 0.14 in.
to 0.19 in. This creates a difficulty in determining the winding pattern and related parameters,
especially degree of interweaving. A few sample tubes were wound, and a bandwidth of 0.16 in.
seemed to give the best pattern (least amount of gaps and overlaps). Therefore, a bandwidth
of 0.16 in was used to generate all of the winding paths. However, the pattern-generation
software (FiberGrafiX from Entec) makes adjustments in the bandwidth to more closely match
a "theoretical" value generated by the program. This accounts for the variations in bandwidth
seen in Table D.1. The values of $\mathcal{L}_{st}$, $\mathcal{L}_{min}$, $\mathcal{L}_{maj}$, $\mathcal{R}_{max}$, and $\mathcal{I}$ shown in Table 5.5 were
calculated using the bandwidths and wind angles from Tables 5.1 and D.1. For comparison,
the FiberGrafiX values of $\mathcal{N}$ and m_2 are also listed in Table D.1.

Figure 5-3 shows a plot of $\mathcal{I}$ versus $\mathcal{R}$ for the three wind angles. $\mathcal{I}$ increases towards 1.0 as
$\mathcal{R}$ increases. Note that the ratio of the $\mathcal{I}$'s for different wind angles is constant with respect to
repeat, *i.e.*

$$\frac{\mathcal{I}(\theta_1, \mathcal{R}_1)}{\mathcal{I}(\theta_2, \mathcal{R}_1)} = \frac{\mathcal{I}(\theta_1, \mathcal{R}_2)}{\mathcal{I}(\theta_2, \mathcal{R}_2)} \approx \frac{\sin\theta_1}{\sin\theta_2} \tag{5.1}$$

In addition to bandwidth, the thickness of the cylinders was also difficult to characterize.
Even though the tubes were wrapped with release film and shrink tape during cure, they still
show large variations in thickness. In general, the tubes are thickest along the major crossovers
and thinnest in the laminar regions.

Ten measurements were made on each cylinder: four direct thickness measurements; two
inner diameter measurements; and four outer diameter measurements. Figure 5-4 shows where

---

[1]The extensometers were accidentally destroyed by one of the technicians during an unrelated test. Otherwise,
more strain data may have been taken.

Degree of Interweaving vs. Repeat
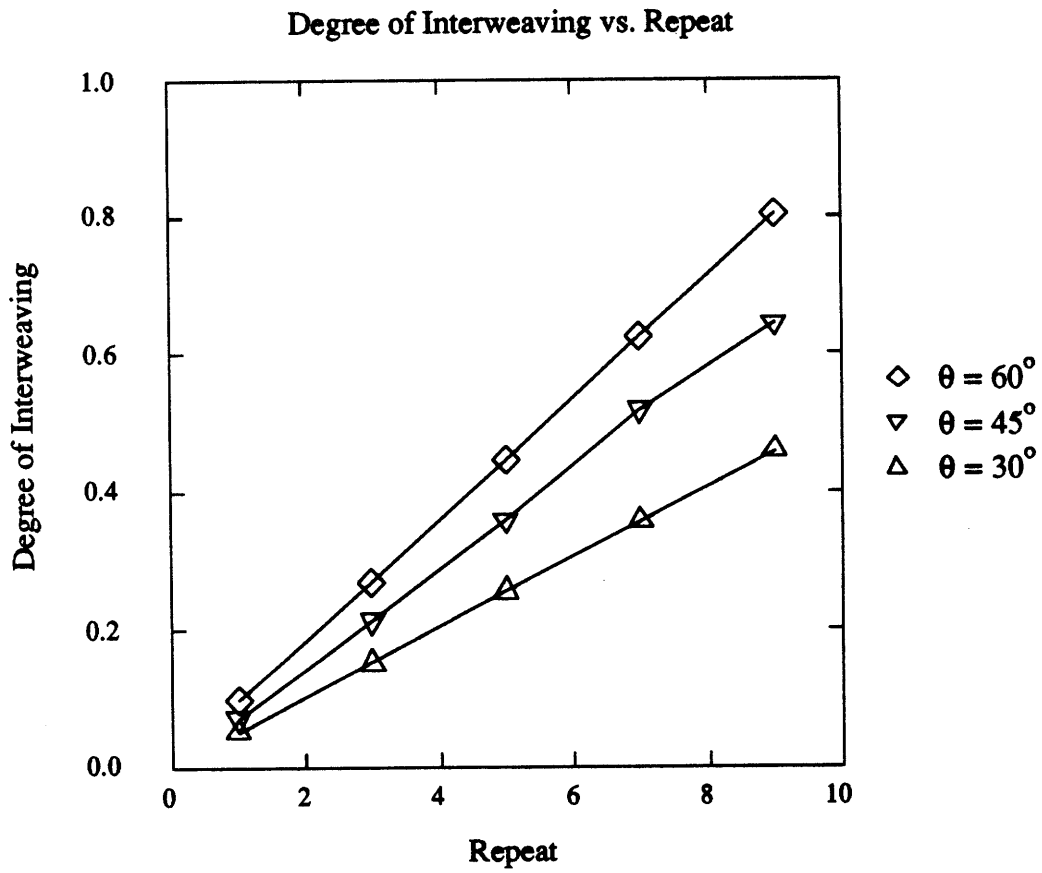
Figure 5-3: $\mathcal{I}$ as a Function of $\mathcal{R}$

Tube	$\mathcal{L}_{st}(in)$	$\mathcal{L}_{min}(in)$	$\mathcal{L}_{maj}(in)$	$\mathcal{R}_{max}$	$\mathcal{I}$
T30R1	0.2772	6.2832	5.1642	19.6299	0.0509
T30R3	0.2772	2.0944	1.5366	19.6299	0.1528
T30R5	0.2772	1.2566	0.8111	19.6299	0.2547
T30R7	0.2772	0.8976	0.5001	19.6299	0.3566
T30R9	0.2772	0.6981	0.3274	19.6299	0.4585
T45R1	0.2244	6.2832	2.9172	14.0000	0.0714
T45R3	0.2244	2.0944	0.8228	14.0000	0.2143
T45R5	0.2244	1.2566	0.4039	14.0000	0.3571
T45R7	0.2246	0.8976	0.2088	13.5083	0.5182
T45R9	0.2244	0.6981	0.1247	14.0000	0.6429
T60R1	0.1852	6.2832	1.7025	10.1931	0.0981
T60R3	0.1555	2.0944	0.4250	11.2022	0.2678
T60R5	0.1555	1.2566	0.1928	11.2022	0.4463
T60R7	0.1555	0.8976	0.0933	11.2022	0.6249
T60R9	0.1555	0.6981	0.0380	11.2022	0.8034

Table 5.5: Physical Parameters of Wound Cylinders

these measurements were made. The direct thickness measurements are the least accurate—they give a maximum rather than average or typical thickness, as shown in Figure 5-5. The outer diameter measurements are somewhat more accurate. By varying the height at which the O.D. measurements are made, they can be taken in both thick and thin regions to give a range of values. Finally, the inner diameter measurements are very accurate. Because the mandrels were not flexible, the inside surfaces of the tubes were very smooth.

For later calculations, the thickness used is

$$t_{cyl} = \frac{\text{ODAVG} - \text{IDAVG}}{2} \qquad (5.2)$$

where ODAVG and IDAVG are the average outer diameter and inner diameter measurements for a cylinder. This method, rather than the direct thickness method, was chosen because it uses the most accurate and typical measurements available. Table 5.6 shows the variations of these measurements with wind angle and repeat. The average thickness for all of the cylinders was 0.29 in. Ply thicknesses were assumed to be equal, i.e. $t_{ply} = t_{cyl}/4$.

The remaining important physical parameters are resin and void content. Funding was
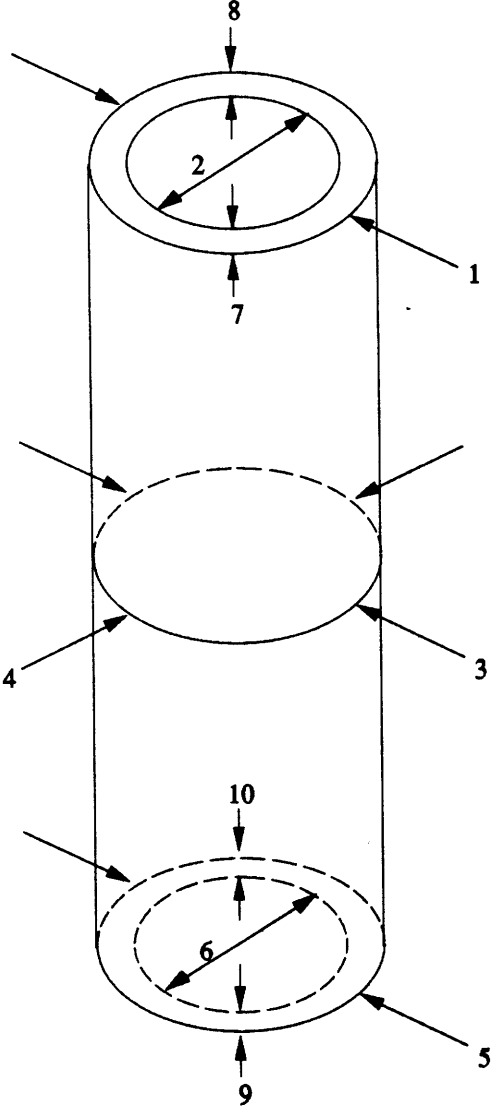
Figure 5-4: Measurement Locations
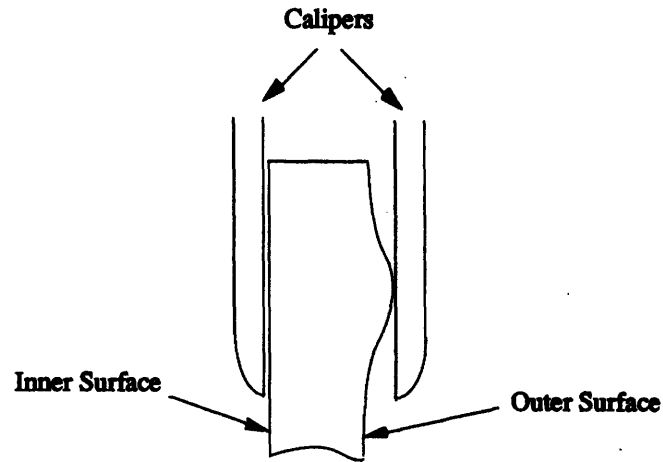
Figure 5-5: Inaccuracy in Thickness Measurements

Tube	t (in)	Tube	t (in)	Tube	t (in)	t_{avg} (in)
T30R1.1	.029	T30R1.2	.028	T30R1.3	.028	.028
T30R3.1	.026	T30R3.2	.028	T30R3.3	.027	.027
T30R5.1	.027	T30R5.2	.025	T30R5.3	.028	.027
T30R7.1	.028	T30R7.2	.028	T30R7.3	.029	.028
T30R9.1	.028	T30R9.2	.028	T30R9.3	.028	.028
T45R1.1	.030	T45R1.2	.029	T45R1.3	.032	.030
T45R3.1	.031	T45R3.2	.031	T45R3.3	.029	.030
T45R5.1	.029	T45R5.2	.030	T45R5.3	.030	.030
T45R7.1	.033	T45R7.2	.029	T45R7.3	.031	.030
T45R9.1	.031	T45R9.2	.030	T45R9.3	.030	.030
T60R1.1	.026	T60R1.2	.027	T60R1.3	.025	.026
T60R3.1	.028	T60R3.2	.029	T60R3.3	.029	.029
T60R5.1	.029	T60R5.2	.028	T60R5.3	.027	.028
T60R7.1	.030	T60R7.2	.029	T60R7.3	.030	.030
T60R9.1	.028	T60R9.2	.030	T60R9.3	.030	.029

Table 5.6: Thickness Measurements

not available to make these measurements, so any variations in these parameters cannot be considered. The tow-preg was shipped with a 35% resin content.

5.3 Test Results

5.3.1 Qualitative Results

Two types of failure curves were seen, as illustrated by Figures 5-6 and 5-7. The 30° and 60° cylinders were both linear to failure, as in the first figure. The failure mode in these cylinders was best characterized as a localized shell buckling. In some cases, a clear dimple could be seen while the tube was still loaded after failure. Cracks propagated out from this dimple, generally following the major and minor crossovers. These cracks extended through the entire thickness of the composite.

On the 60° tubes, the cracks did not propagate up or down the cylinder very much—they mostly stayed near the latitude of the dimple. A typical crack would start at the dimple, run around the tube, and end near its starting point. On the 30° tubes, however, the cracks followed the minor crossovers along the entire length of the tube, being stopped only by the endcaps. These cracks were not very jagged.

The 45° tubes were nonlinear to failure, and failed from a delamination of the outer ply. The outer-ply fibers were visibly bowed out from the surface of the composite, and cracks often formed under or near these delaminations. Like the 30° and 60° cylinders, the cracks extended through the entire thickness of the composite.

Finally, the 30° and 60° tubes were fairly quiet until the moment of failure, when a large crack was heard. This indicates that the material was not failing locally prior to the ultimate failure. But the 45° tubes were much noisier prior to ultimate failure, even at fairly low load levels.

Pictures of some of the failed specimens were taken, but they don't show much. Two of the better pictures appear in Figures 5-8 and 5-9. The former shows a 45° specimen: the bowing of the outer ply fibers is apparent. It is difficult to see the pattern markings, but the bulge on the left (the horizontal part) follows a major crossover. At the point where the minor crossovers meet (the "X"), the crack moves upward, roughly following the minor crossover.

Ultimate Load
and
Failure Point

Load

Stroke
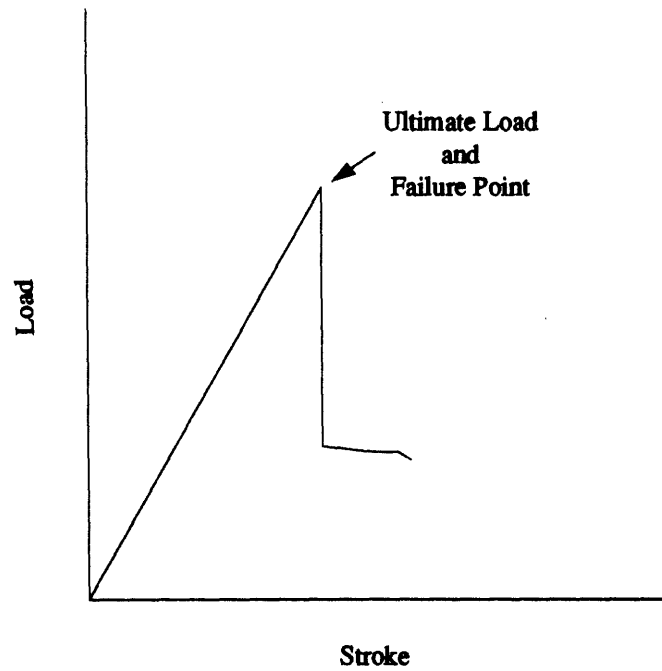
Figure 5-6: Linear Failure Curve

Ultimate Load

Failure Point

Load

Stroke
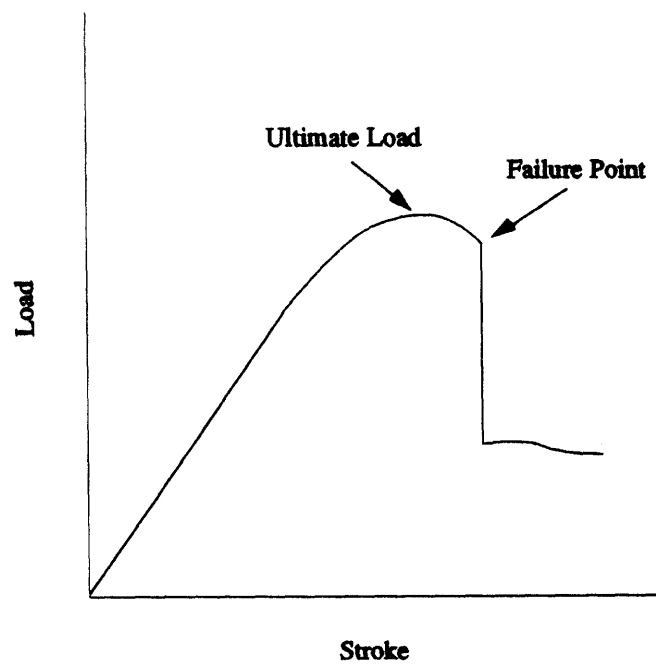
Figure 5-7: Nonlinear Failure Curve

The latter picture shows a typical 60° specimen. The crack is much cleaner than the crack of the 45° specimen—this was generally true of the 60° and 30° cylinders. Again, the crack seems to follow both the major and minor crossovers, making its turn at an "X" point. A dimple cannot be seen in this picture.

Some other typical failures are sketched[2] in Figures 5-10 through 5-14. In these sketches, it is easier to see how the cracks follow the winding patterns. Figure 5-10 shows a failure typical of the 60° specimens: a dimple forms near a major crossover, and a crack propagates around the cylinder, staying at roughly the same axial coordinate. In several cases, deformation along the cracks was large enough to be visible.

The next three figures show failures common to the 45° specimens (for some reason, these gave the most variety). Figure 5-11 shows one type of crack and the shredding that accompanied it. The crack initiates on a major crossover, then follows two minor crossovers upwards. The fibers along the minor crossovers have sheared, as shown in the inset (see also Figure 5-8). Figure 5-12 is similar, but the crack is spiral and follows a single minor crossover. In some cases, the crack begins or ends along a major crossover.

Figure 5-13 shows the last type of failure seen in 45° specimens. The outer ply has bulged out along a single major crossover. This is similar to the bulging on the left of Figure 5-8, but extends all the way around the cylinder. This looks like it may be a shell buckling, but is more likely an outer ply buckling.

Finally, Figure 5-14 shows the typical failure for 30° specimens. The cracks followed the minor crossovers, often along the entire length of the tube. Most of the cracks were very clean, as in Figure 5-9, but in a few cases shredding was seen near the "X" at the meeting of major and minor crossovers.

In general, the crossovers, or weavings, seem to act as barriers to crack growth. This helps explain why moderate amounts of interweaving increase strength, as will be seen in the next section.

---

[2]Figures are based on sketches made during testing.
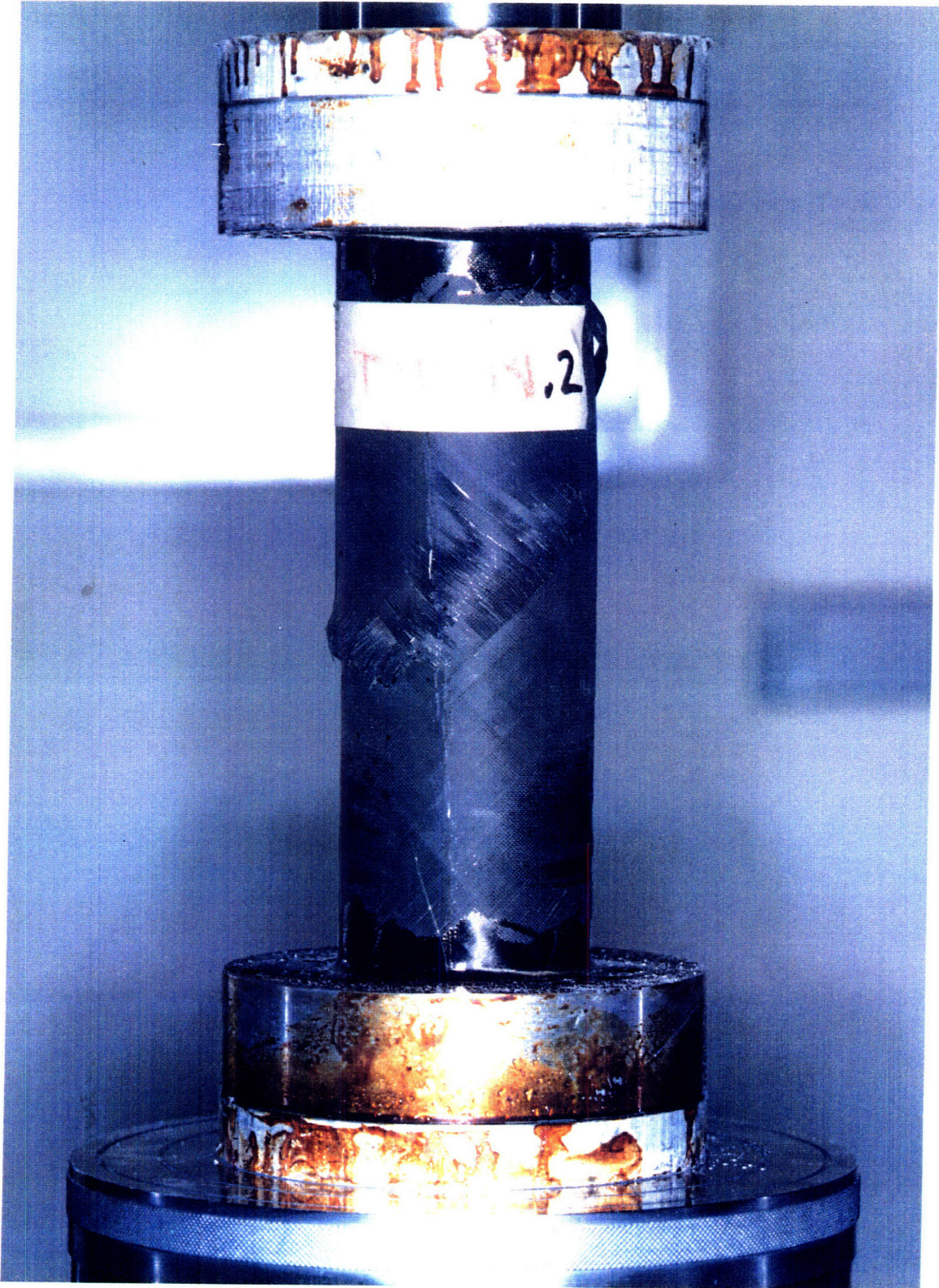
Figure 5-8: Picture of 45° Cylinder After Failure
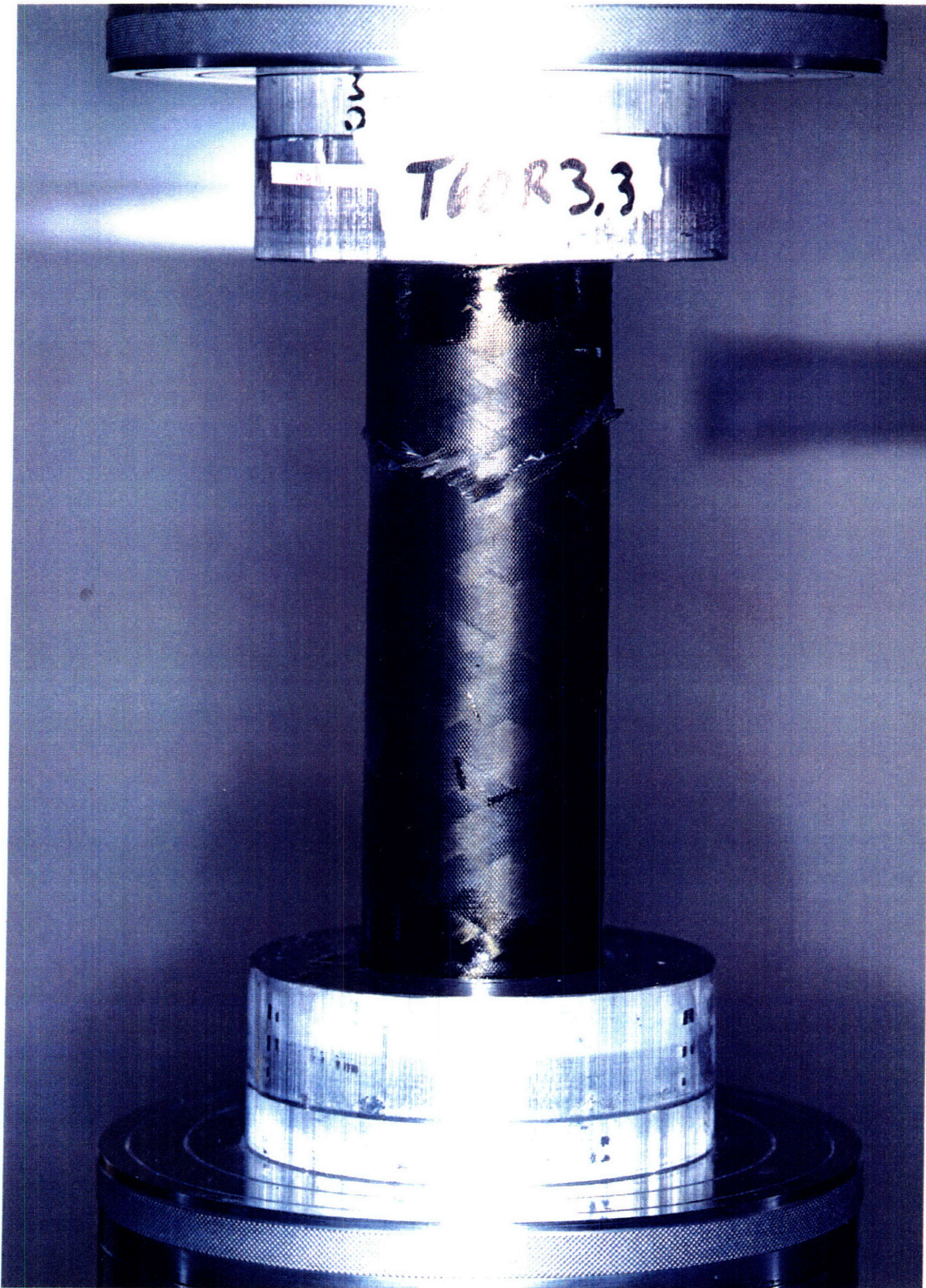
Figure 5-9: Picture of 30° Cylinder After Failure
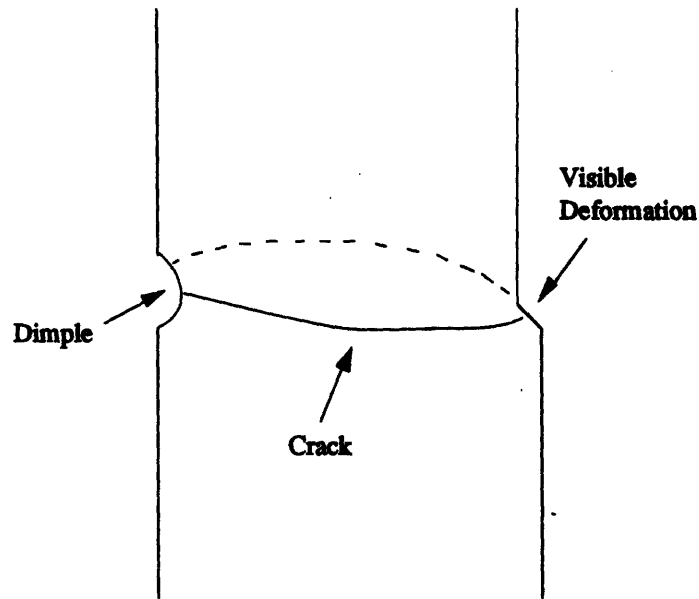
Figure 5-10: Dimple and Crack of 60° Specimen

5.3.2 Quantitative Results

Ultimate loads were taken as the highest load attained prior to ultimate failure (Figures 5-6 and 5-7). For the 30° and 60° specimens, this was the last point before failure. For the 45° specimens, this point occurred slightly before ultimate failure. Since neighboring points were very close to each other in the maximum load region, a curve was not fitted to this region of the 45° load/stroke data.

Ultimate loads were converted to stresses by calculating the typical cross-sectional area of the cylinders

$$A = \pi D t_{cyl} \tag{5.3}$$

where $D = \text{IDAVG} + t_{cyl}$ is the midplane diameter. Figures 5-15 through 5-17 show the ultimate stresses versus the degree of interweaving for each wind angle. Note the large amount of scatter in the 30° and 45° cases; the 60° cases show relatively little scatter.

The 30° and 60° specimens show the most variation in strength with degree of interweaving. This variation can be quite significant: the 60° cylinders show an 80% increase in strength from $\mathcal{I} = 0.0981$ to $\mathcal{I} = 0.4463$. On the other hand, the 45° specimens show little or no variation with interweaving.
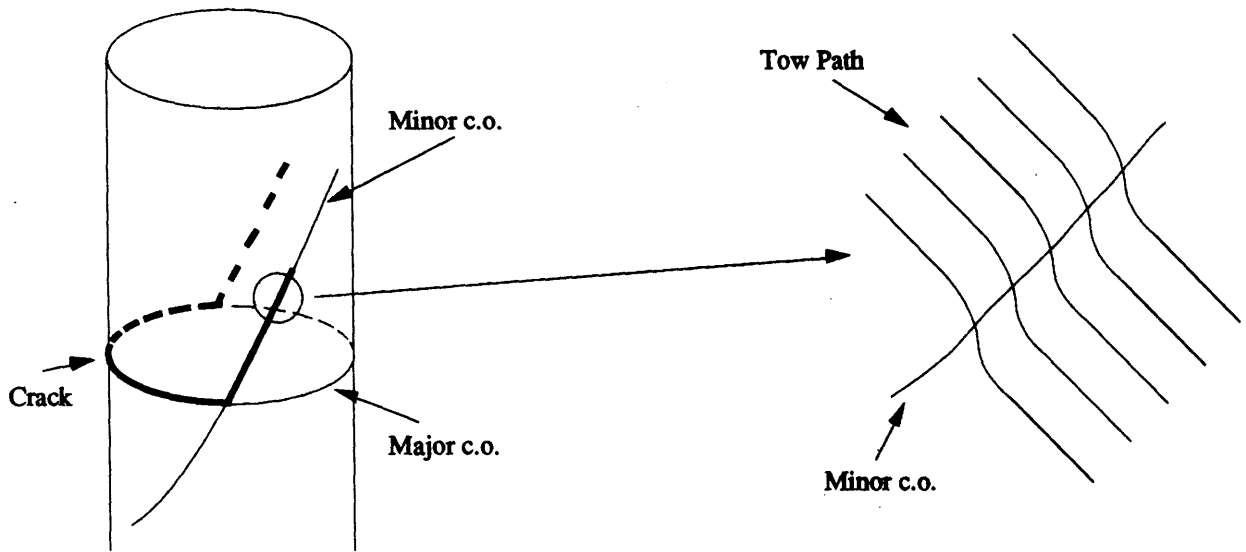
Figure 5-11: Crack of 45° Specimen
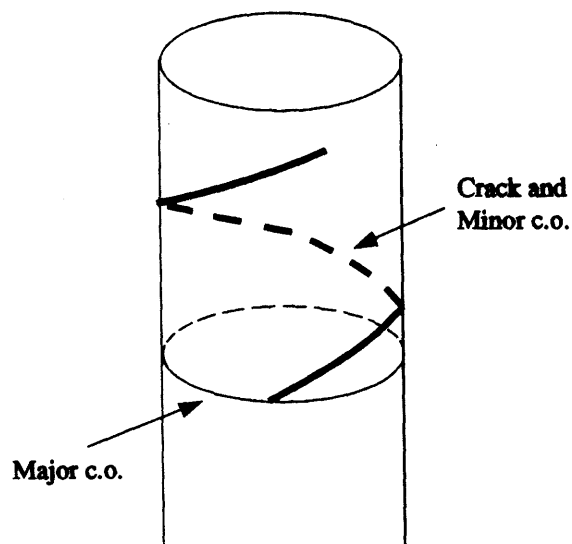
Figure 5-12: Spiral Crack of 45° Specimen
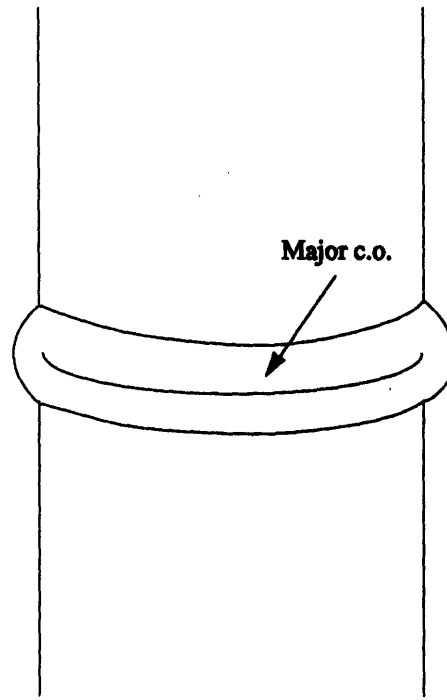
Figure 5-13: Outer Ply Buckling of 45° Specimen

Figure 5-18 shows all three sets of data on the same plot. The curves are not theoretically derived: they are simply weighted fits to the points, so the trends can be more easily seen. There appears to be an optimal degree of interweaving for each wind angle which gives a maximum strength, but this value is not the same for each angle. For the 30° cylinders, it is around $\mathcal{I} = 0.2$; for the 60° cylinders, it is around $\mathcal{I} = 0.45$.

Figure 5-19 is another plot of the ultimate stresses, but this time plotted against repeat. Now the peaks fall closer together—all are in the region $3 \leq \mathcal{R} \leq 5$. This may indicate that the failure load is a function of the winding pattern rather than the amount of weaving. That is, the number of diamonds and their distribution on the cylinder may be more important than the relative amounts of interweaving.

Axial modulus was also measured. Because strain data could not be taken, the strain was approximated as

$$\epsilon = \frac{\Delta \ell}{\ell} \tag{5.4}$$

where ℓ was the initial length of the cylinder (between the endcaps) and $\Delta \ell$ the change in length

Crack and
Minor c.o.

Major c.o.

Major c.o.

Tow Path

Minor c.o.
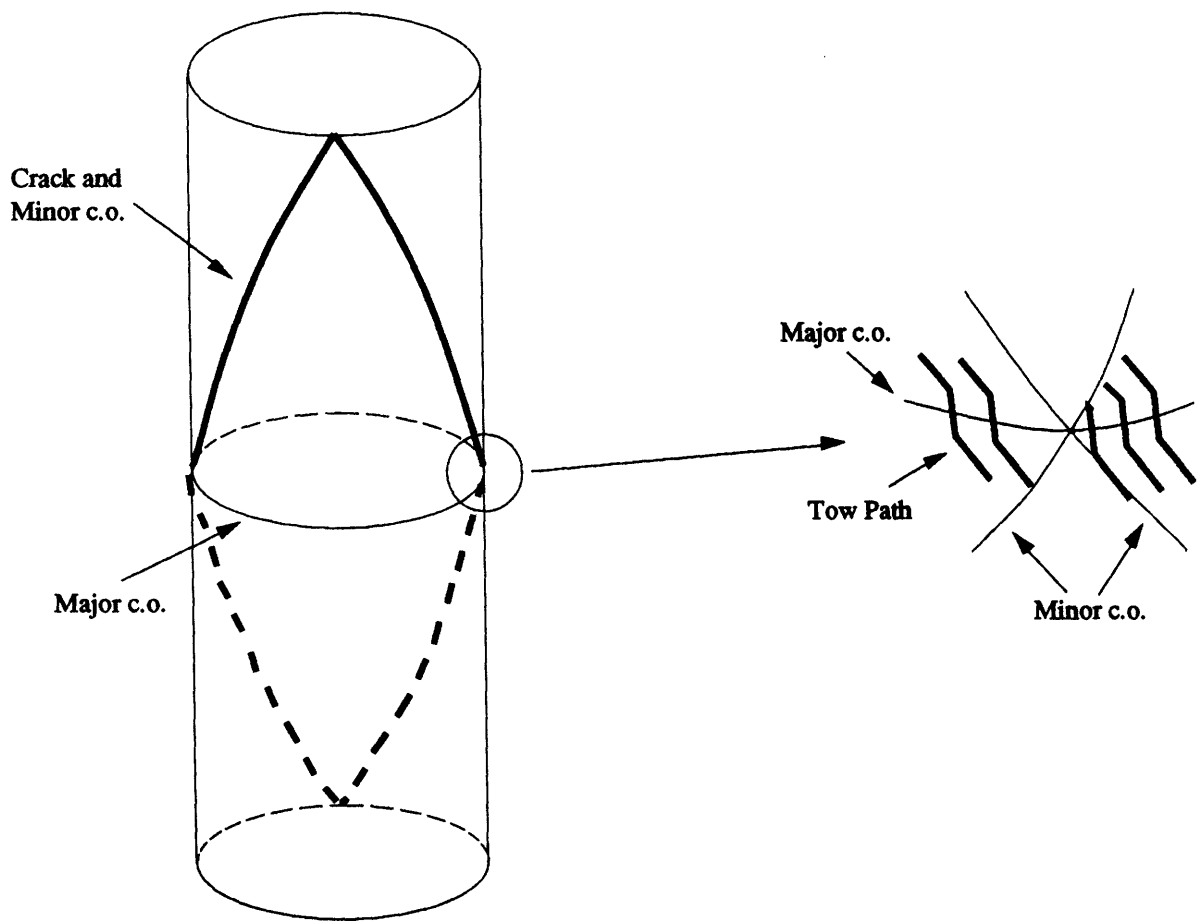
Figure 5-14: Crack of 30° Specimen
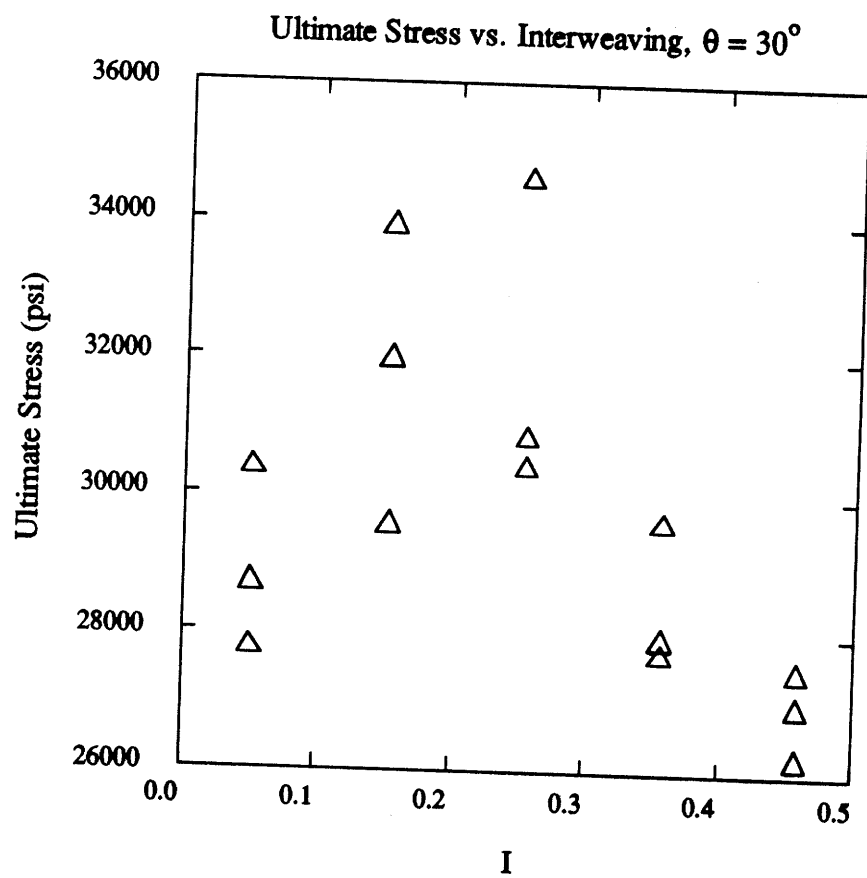
Figure 5-15: Ultimate Stress of the 30° Cylinders
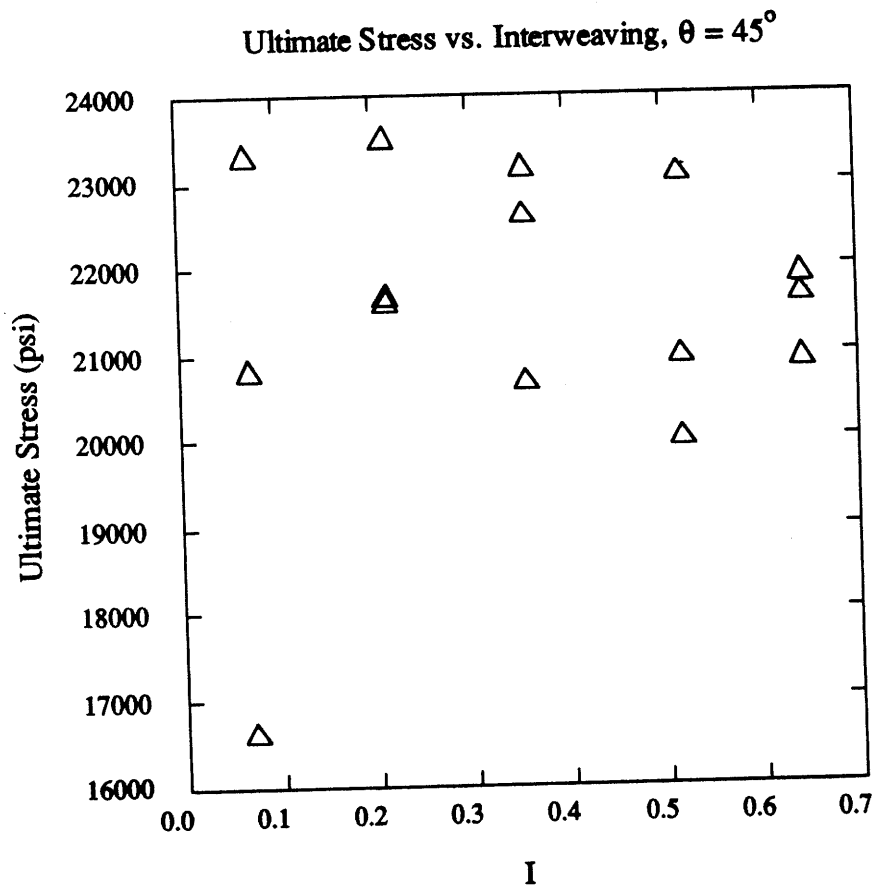
Figure 5-16: Ultimate Stress of the 45° Cylinders

Ultimate Stress vs. Interweaving, $\theta = 60°$
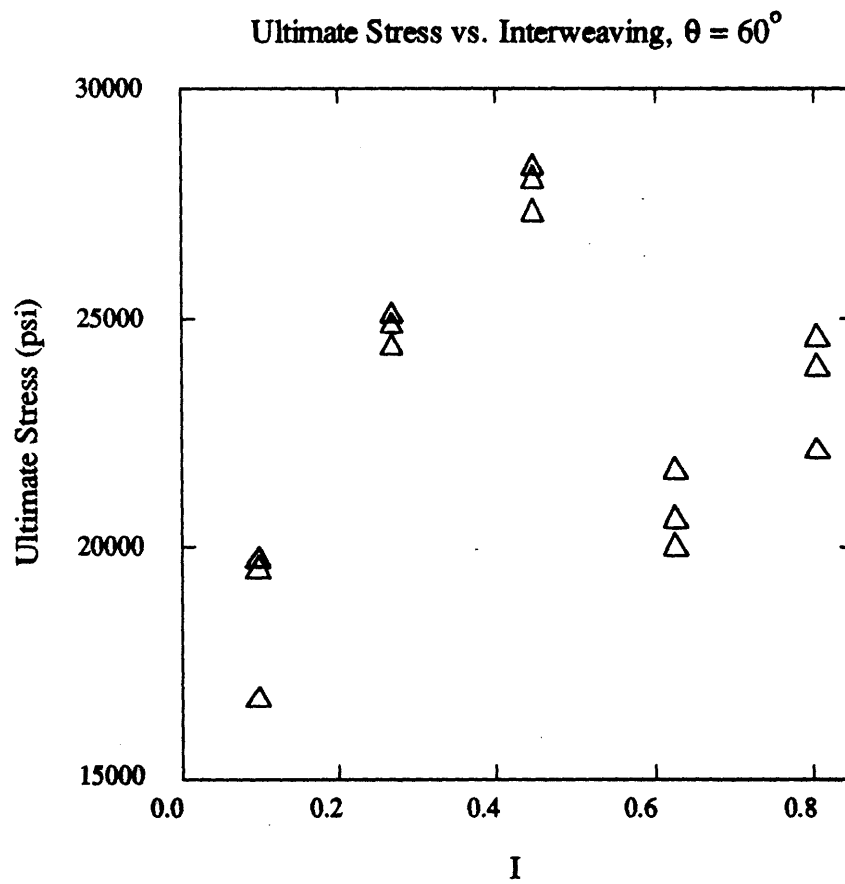
Figure 5-17: Ultimate Stress of the 60° Cylinders
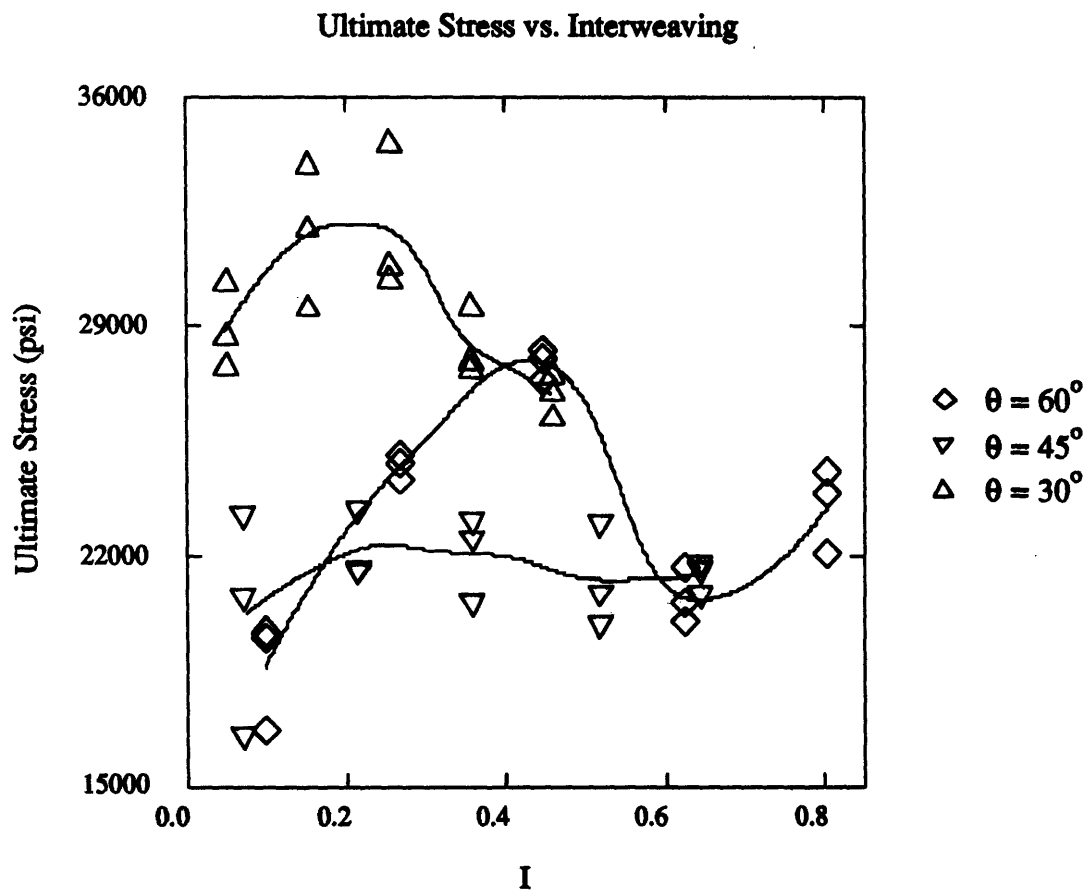
Figure 5-18: Combined Plot of Ultimate Stresses vs. Interweaving

Ultimate Stress vs. Repeat
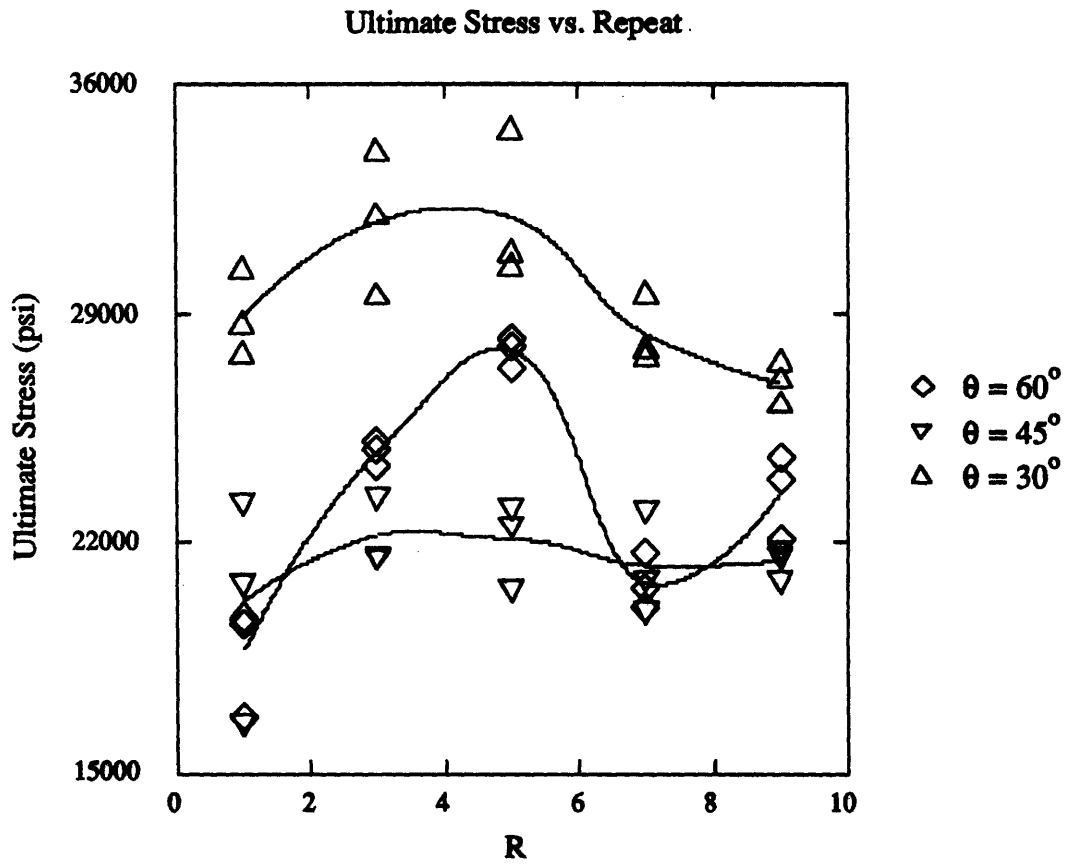
Figure 5-19: Combined Plot of Ultimate Stresses vs. Repeat

Axial Modulus vs. Interweaving
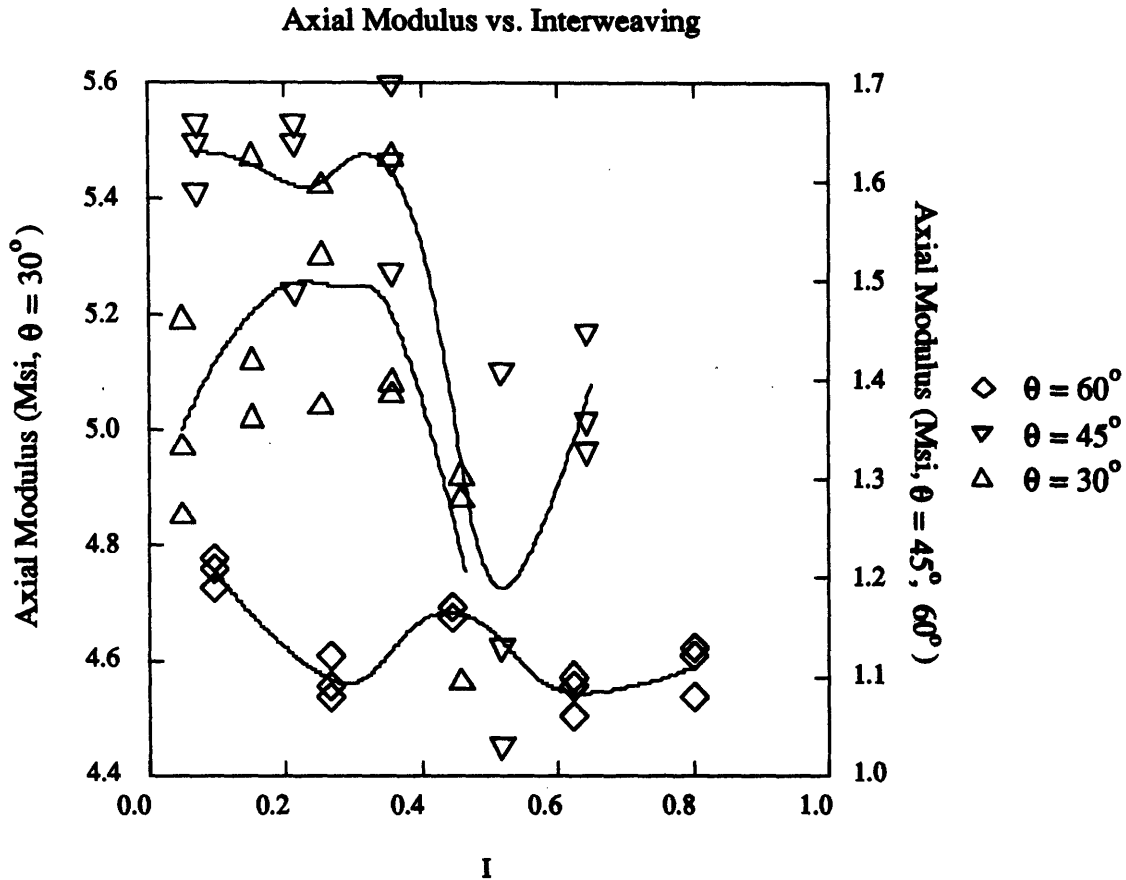
Figure 5-20: Combined Plot of Axial Moduli vs. Interweaving

(taken from the stroke readings). This method of measuring strain is not very accurate, but no attempt was made to model the effect, so this should at least show any general trends.

Figures 5-20 and 5-21 show this modulus data plotted against interweaving and repeat (note the two different scales on each graph). Again there is a lot of scatter, and none of the curves appear very similar. The 45° cylinders show the most variation in modulus; the 30° show very little. This is opposite to the trend seen in the strength data.

5.3.3 Analysis

The previous sections show that interweaving significantly affects the compressive properties of filament-wound cylinders. In terms of failure loads, the magnitude of the effect depends on both the amount of interweaving and the failure mode. Several models to predict these effects

Axial Modulus vs. Repeat
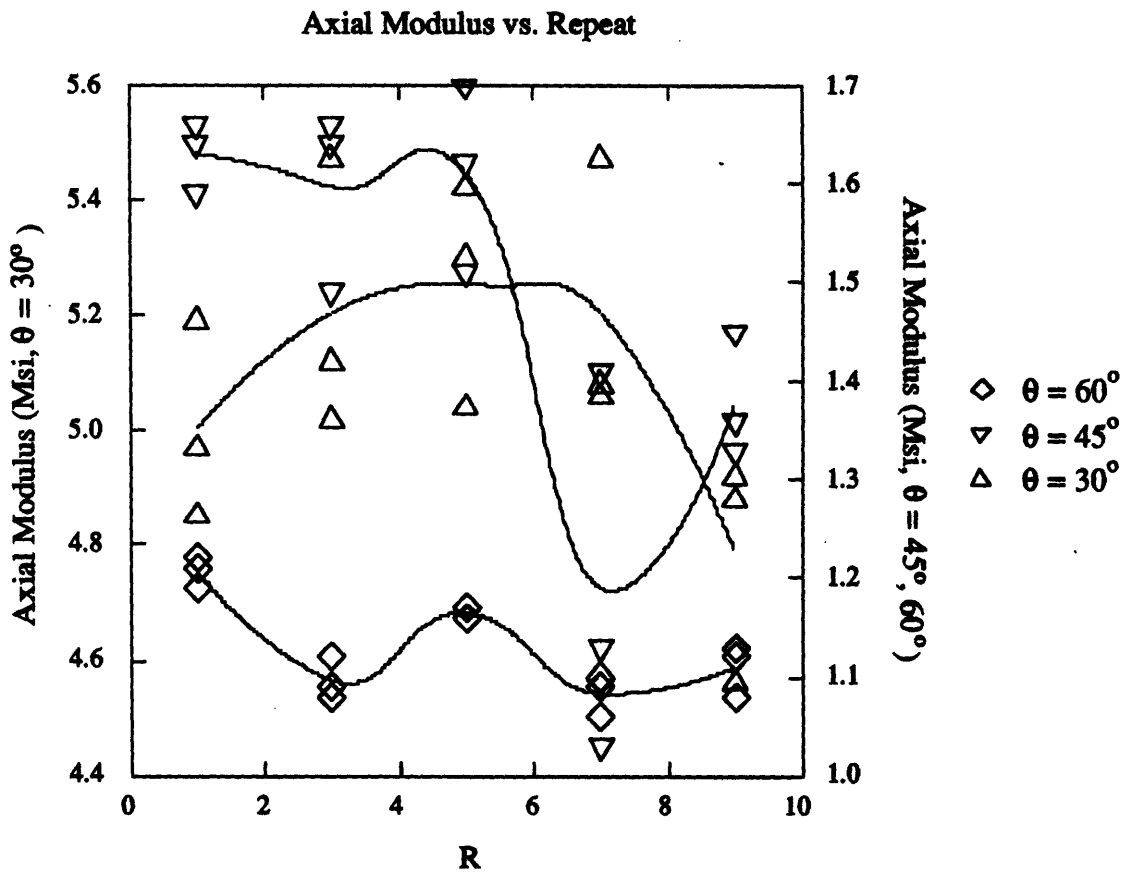
Figure 5-21: Combined Plot of Axial Moduli vs. Repeat

are proposed in Chapter 4. Let us now see how accurate these models are, beginning with the simplest.

One model not mentioned in Chapter 4 is the purely empirical approach, suggested by Tsai [39]:

> The predictions of elastic constants and strength of fabrics, filament-wound and braided structures can be made using classical micro and macro mechanics with *appropriate empirical correction factors*[3]. We propose to replace the woven composite by a multidirectional laminate consisting of the fiber angles. Then the micromechanics formulas for the stiffness and strength are applied to the plies as before.

This model would be useful if a limited number of correction factors could be found to describe all wound composites. But the data in the previous section indicates that this is probably not possible.

The 30° and 60° specimens both showed similar variations in strength with interweaving: the former shows a 20% spread from low to high failure load; the latter an 80% spread (based on the raw data). Both curves are also somewhat bell-shaped. But the former peaks near $\mathcal{I} = 0.2$, the latter near $\mathcal{I} = 0.4$. If the measure of interweaving is repeat, then they both peak at about the same point, $4 < \mathcal{R} < 5$, but the latter then shows an increase in strength around $\mathcal{R} = 8$ which the former doesn't show.

Thus, a single empirical constant cannot describe two cylinders when the only difference between them is wind angle. It becomes even more complicated when the 45° cylinder is considered, which shows almost no variation in strength with interweaving. The trend seems to be towards an empirical constant for each wind angle and degree of interweaving, *i.e.* a series of tests for each specimen.

The next simplest models considered were the Vinson and Eckold buckling equations (Section 4.6.2). Neither of these equations can account for interweaving (they are independent of **B**), but they are extremely sensitive to variations in thickness. Thus, they should at least tell us if thickness alone is the main factor behind the spread in the observed failure loads.

First, Figure 5-22 shows the buckling loads predicted by these models for $[\pm 30°]s$, $[\pm 45°]s$,

---

[3]Emphasis mine.
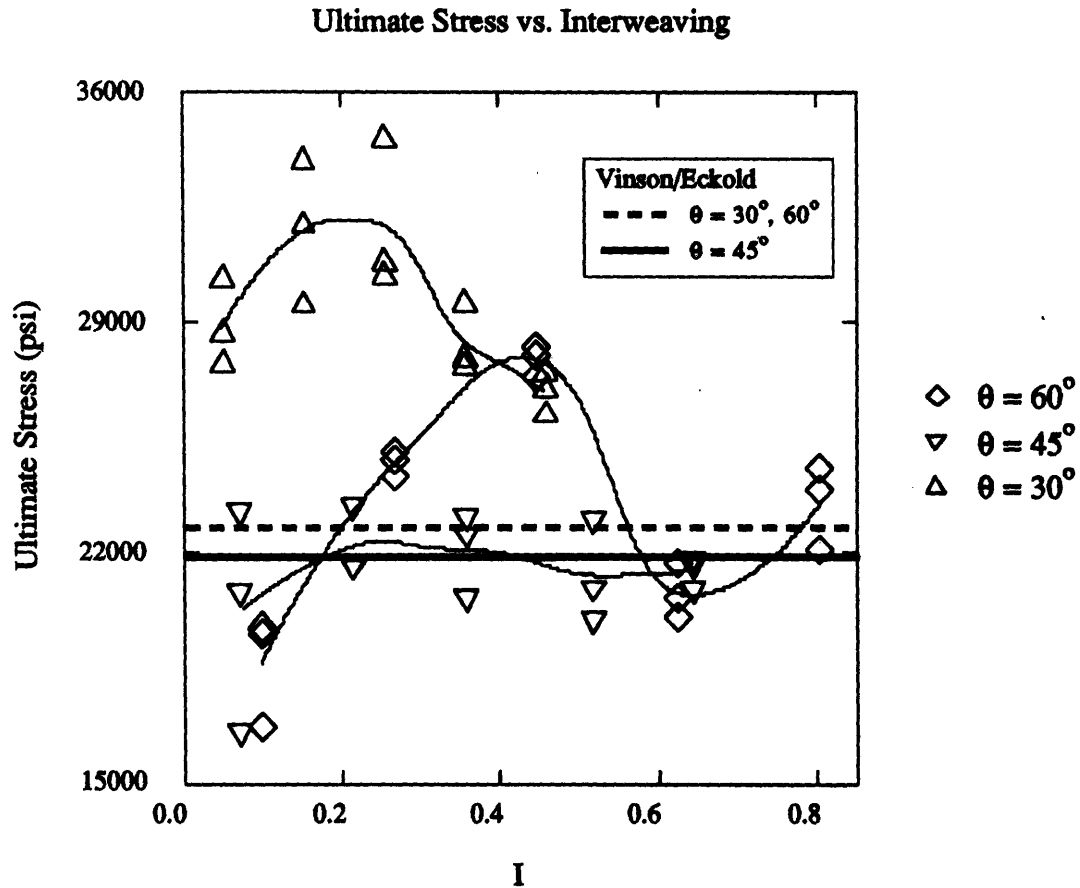
Figure 5-22: Buckling Loads Predicted by Simplest Models, Compared to Experimental Data

and [±60°]$_S$ layups, plotted on the same graph as the experimental data[4]. These calculations use the average thickness for all of the cylinders (0.029 in). As these models stand, they are not even good predictors of a typical or average buckling load for either the 30° or 60° cylinders. We could change the empirical factor so the curves lie near the average of either of the data sets, but then we are back to a purely empirical approach.

Including the variable thicknesses of Table 5.6 produces the results in Figures 5-23 through 5-25. Although some variation in buckling load is now seen as the degree of interweaving changes, those variations are insignificant when compared to the variations in the data. In fact, the predicted values seem to move opposite the experimental values: an increase in the experimental

---

[4]Once again, the models are normalized to the average value of the failure loads of the 45° cylinders. Although these cylinders did not appear to have buckled, they are chosen for the normalization because their failure loads are nearly constant.

Simple Buckling Models with Thickness Variation, θ = 30°
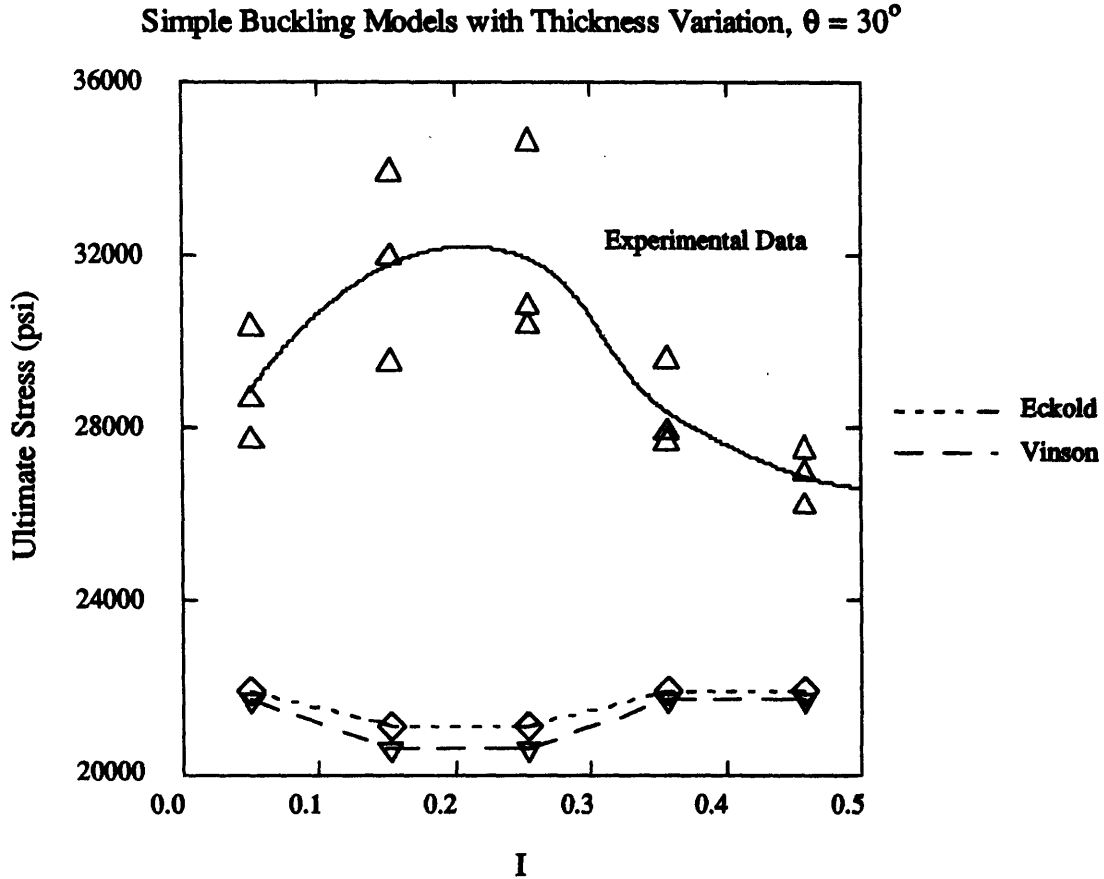
Figure 5-23: Simple Buckling Model with Thickness Variation, Compared to Experimental Data for $\theta = 30°$

value is matched by a decrease in the corresponding *decrease* in the theoretical value, and vice versa.

The last buckling model considered, and the most complicated, is the energy method. It can incorporate both thickness variations and interweaving. The latter factor can be included in one of two ways: by the mosaic models; or by the fiber undulation model. In keeping with the progression from simplest to more complicated, we begin with the mosaic model.

Recall that the mosaic model uses the same A and D matrices obtained for a $[\pm\theta]_2$ laminate, but replaces B with

$$\bar{B} = (1 - \mathcal{I})B$$

The results given by the energy method with this $\bar{B}$, plotted with the experimental data and
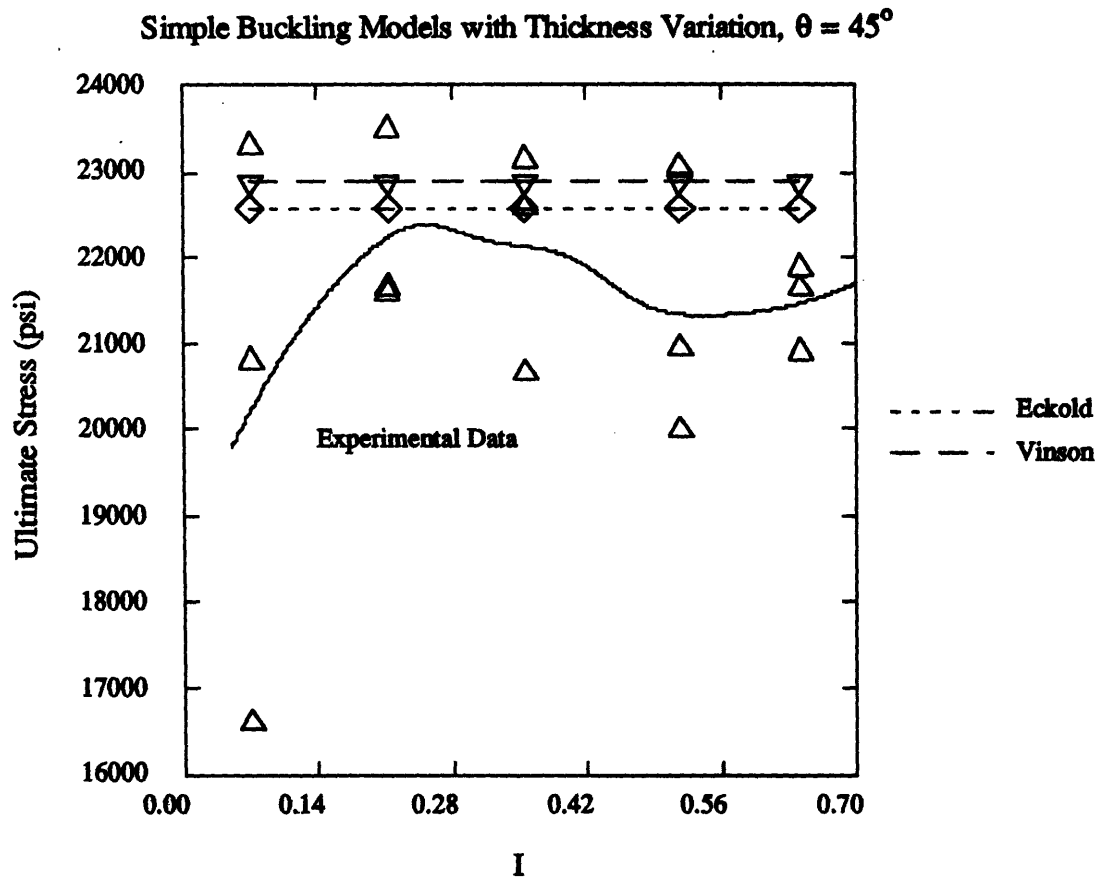
Figure 5-24: Simple Buckling Model with Thickness Variation, Compared to Experimental Data for $\theta = 45°$
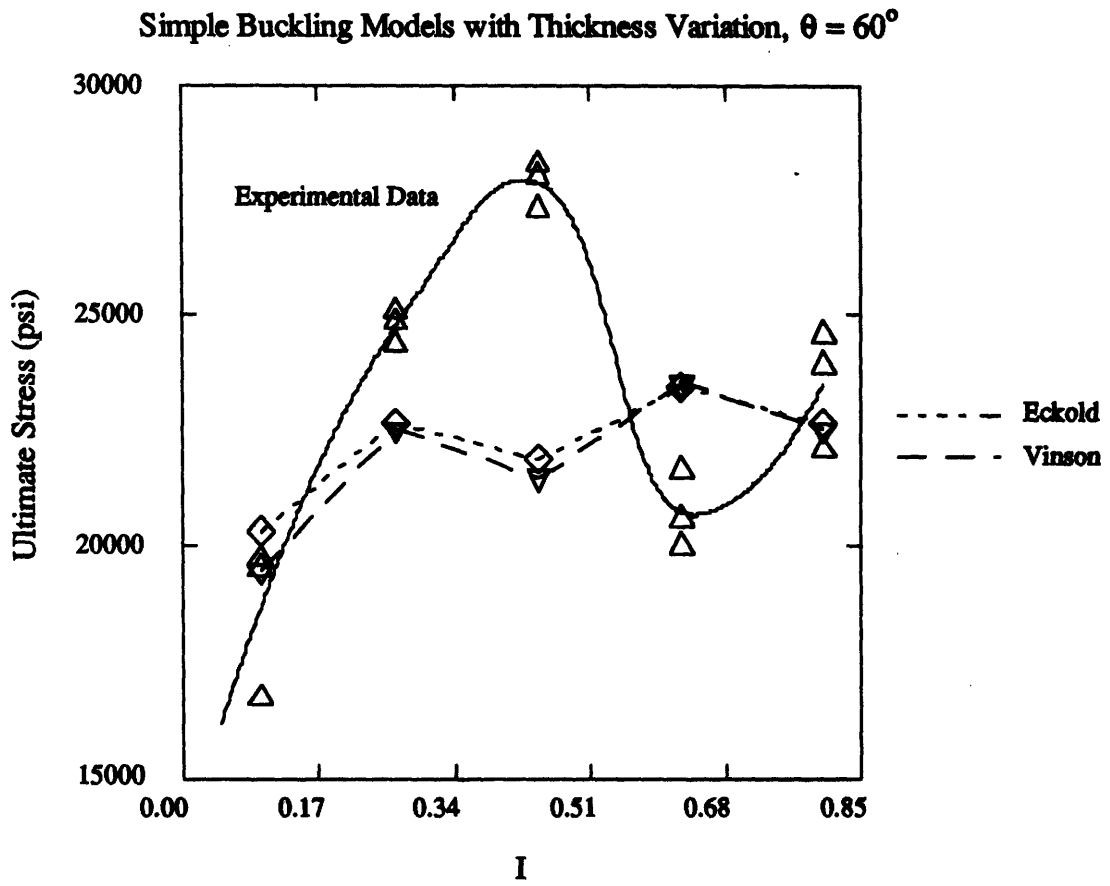
Figure 5-25: Simple Buckling Model with Thickness Variation, Compared to Experimental Data for $\theta = 60°$

Buckling Load by Energy Method, $\theta = 30°$
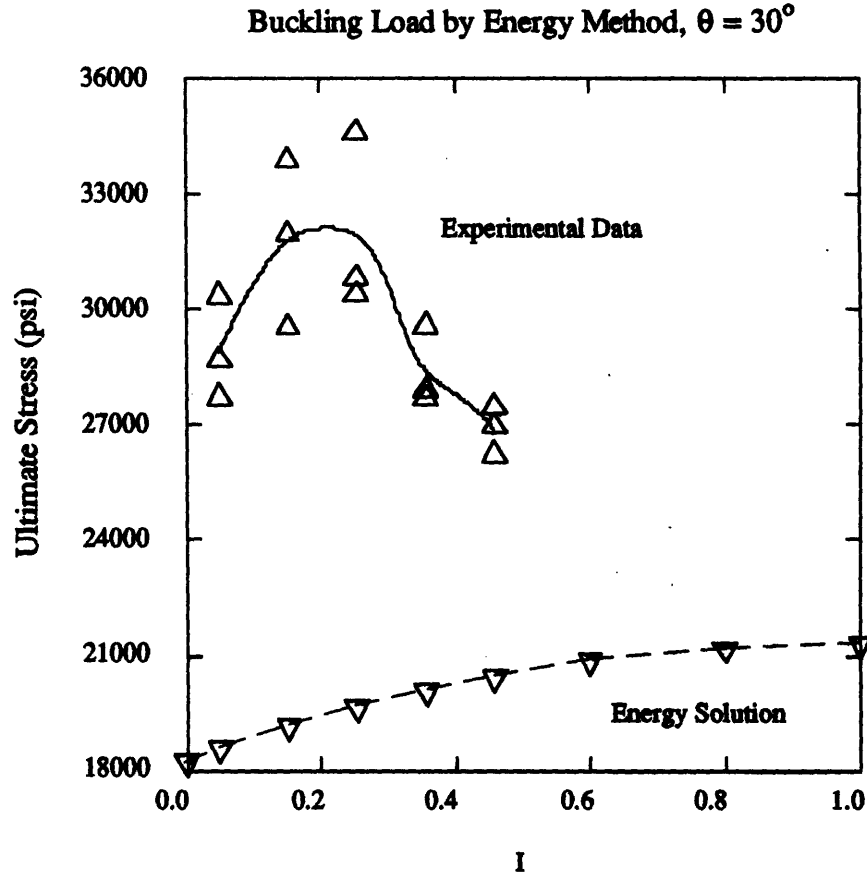
Figure 5-26: Energy Method Compared to Experimental Data, $\theta = 30°$

normalized as in the simple models, are shown in Figures 5-26 through 5-28. Once again, the average thickness of 0.029 in is used. The predicted buckling loads show a smooth increase from a minimum at $\mathcal{I} = 0$ to a maximum at $\mathcal{I} = 1$. This is the same behavior reported by Brito [1] (see page 24, item 3). However, it does not match the observed behavior of the composite cylinders in this study. Even accounting for thickness variations does not help much (Figures 5-29 through 5-31), though this adjustment does not appear as detrimental to the curve shapes as it was for the simpler models.

This time, however, the model might benefit from a different normalization. Remember, the normalization to the average failure load of the 45° cylinders was used only because those failure loads were relatively constant, even though the failure mode was not buckling. Now let us look at the plots of the 30° and 60° data with a new normalization. Let the empirical
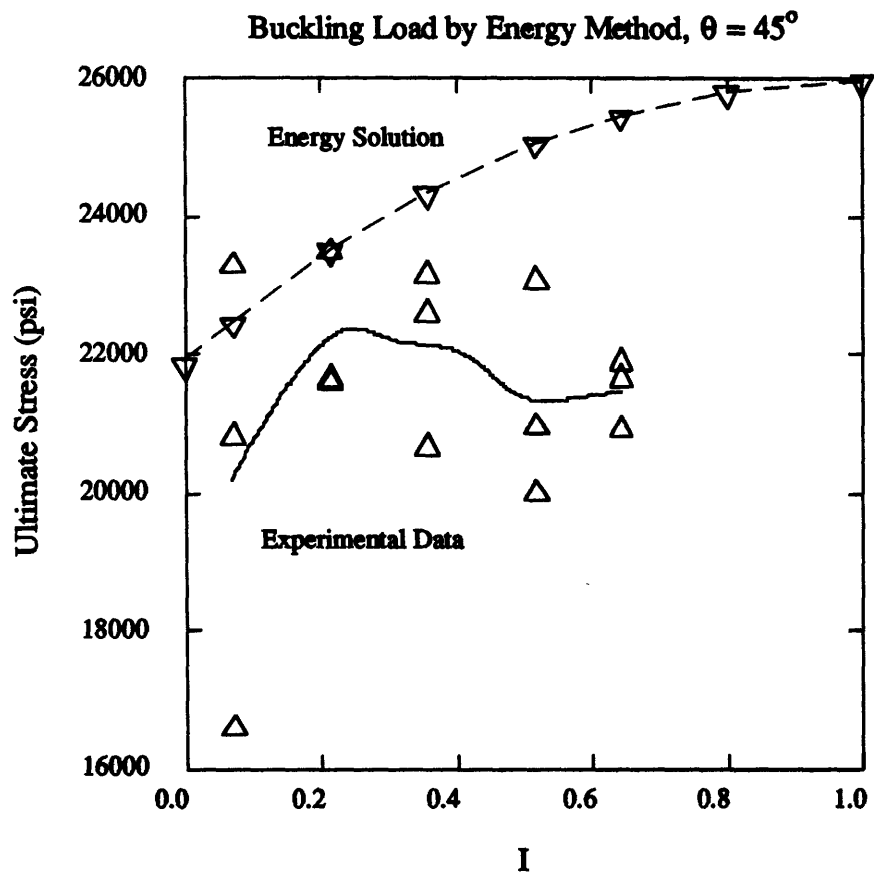
Figure 5-27: Energy Method Compared to Experimental Data, $\theta = 45°$
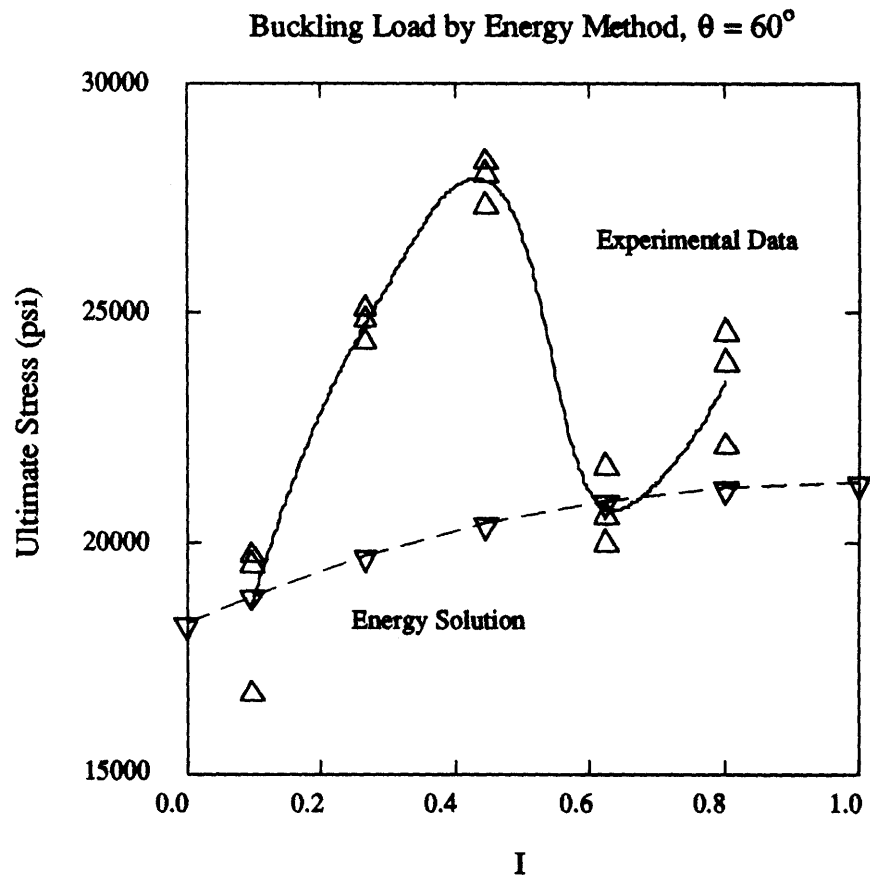
Figure 5-28: Energy Method Compared to Experimental Data, $\theta = 60°$
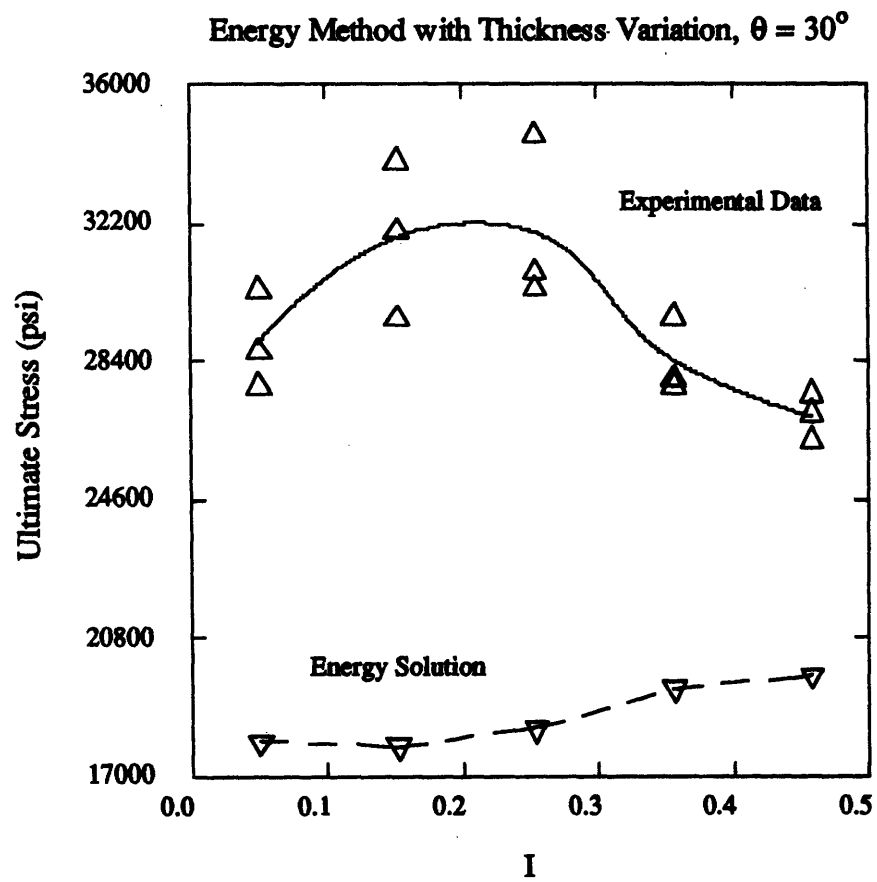
Figure 5-29: Energy Method with Thickness Variation, Compared to Experimental Data for $\theta = 30°$
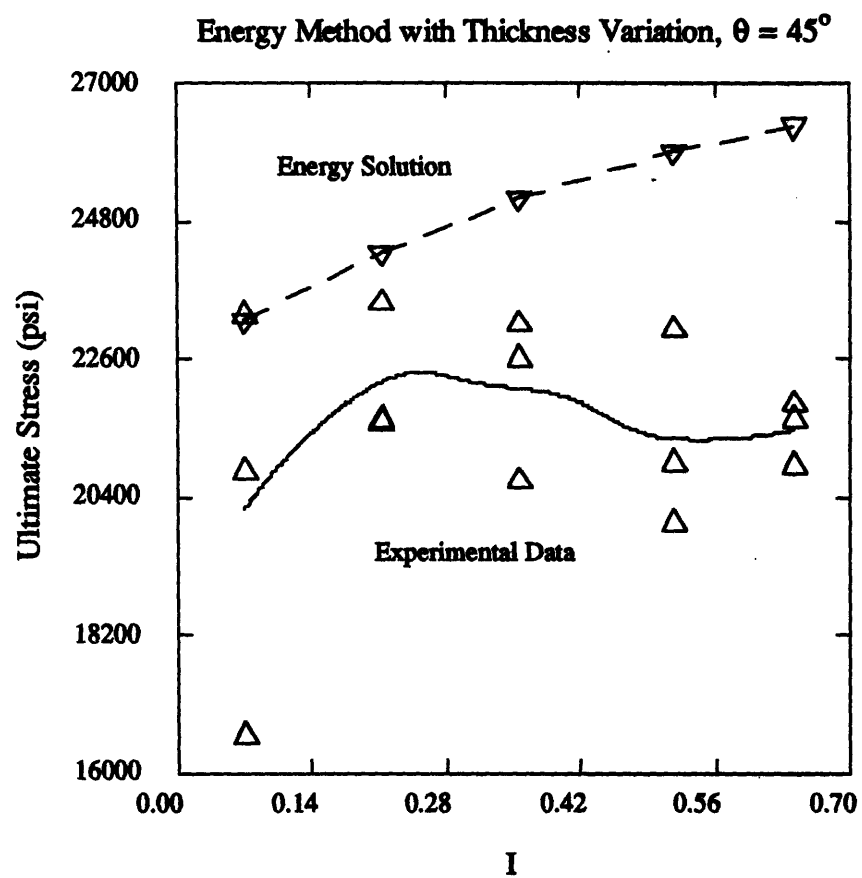
Figure 5-30: Energy Method with Thickness Variation, Compared to Experimental Data for $\theta = 45°$
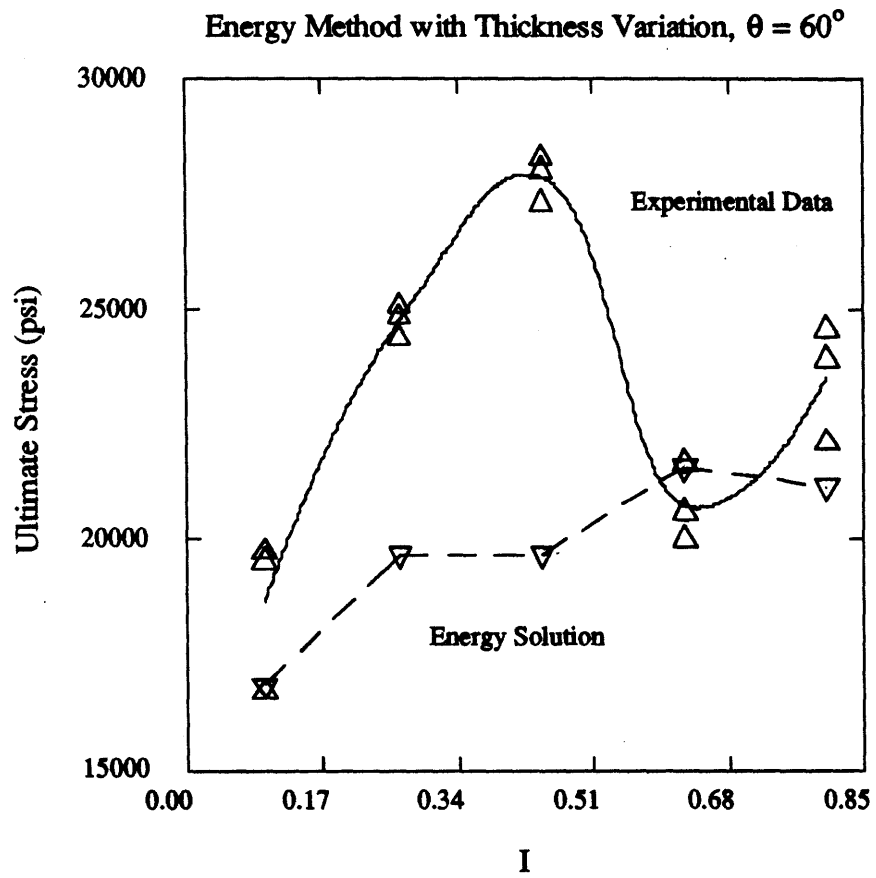
Figure 5-31: Energy Method with Thickness Variation, Compared to Experimental Data for $\theta = 60°$

constant be $\gamma = 0.2$, the value recommended in [11].

Figures 5-32 and 5-33 show this new normalization. The predicted values are now close to both sets of experimental data. A slight decrease in γ would allow both theoretical curves to intersect both sets of experimental data. Note that the energy method puts the 60° values above the 30° values, whereas the experimental data is just the opposite. And for the 60° prediction with thickness variations, the slope between the first two points roughly matches the slope between the first two sets of experimental points.

This new normalization allows us to conclude that the 30° and 60° cylinders did, in fact, fail by shell buckling. The mosaic model does not accurately account for interweaving, but at least the model gives a rough estimate for the failure load. Furthermore, the 45° cylinders fail well below their predicted buckling load[5], indicating some kind of material failure.

The problem still remains of duplicating the bell-shaped curves seen in the experimental data. The buckling load, as predicted by the energy method, is inversely proportional to $|\bar{B}|$. When $\bar{B} = B$ ($\mathcal{I} = 0$), the buckling load takes on its lowest value; when $\bar{B} = 0$ ($\mathcal{I} = 1$), the buckling load takes on its highest value. The theoretical curves rise monotonically from their minimum to their maximum, and no local extremum are predicted.

The variations in the data are also much greater than the total variation achieved by varying B alone. However, the energy method is highly dependent on the values of A and D: if either goes to zero, then the buckling load goes to zero. The fiber undulation model predicts a decrease in the values of the components of A and D. Substituting these new A and D matrices into the energy method will give a correspondingly lower buckling load, which can be of the same magnitude as the observed variations.

However, the final solution is not that simple. The undulation method does not allow an increase in A or D, so all contributions to an increase in the predicted buckling load must come from decreases in B. But the buckling load varies much faster with A and D than it does with B. The result is that altering these three matrices can achieve something like the bell-shaped curves observed in the data, but the variations from maximum to minimum are only on the order of a few percent.

The only way to continue with the current model is to find some justification for allowing

---

[5]Assuming the same γ can be applied to these cylinders.
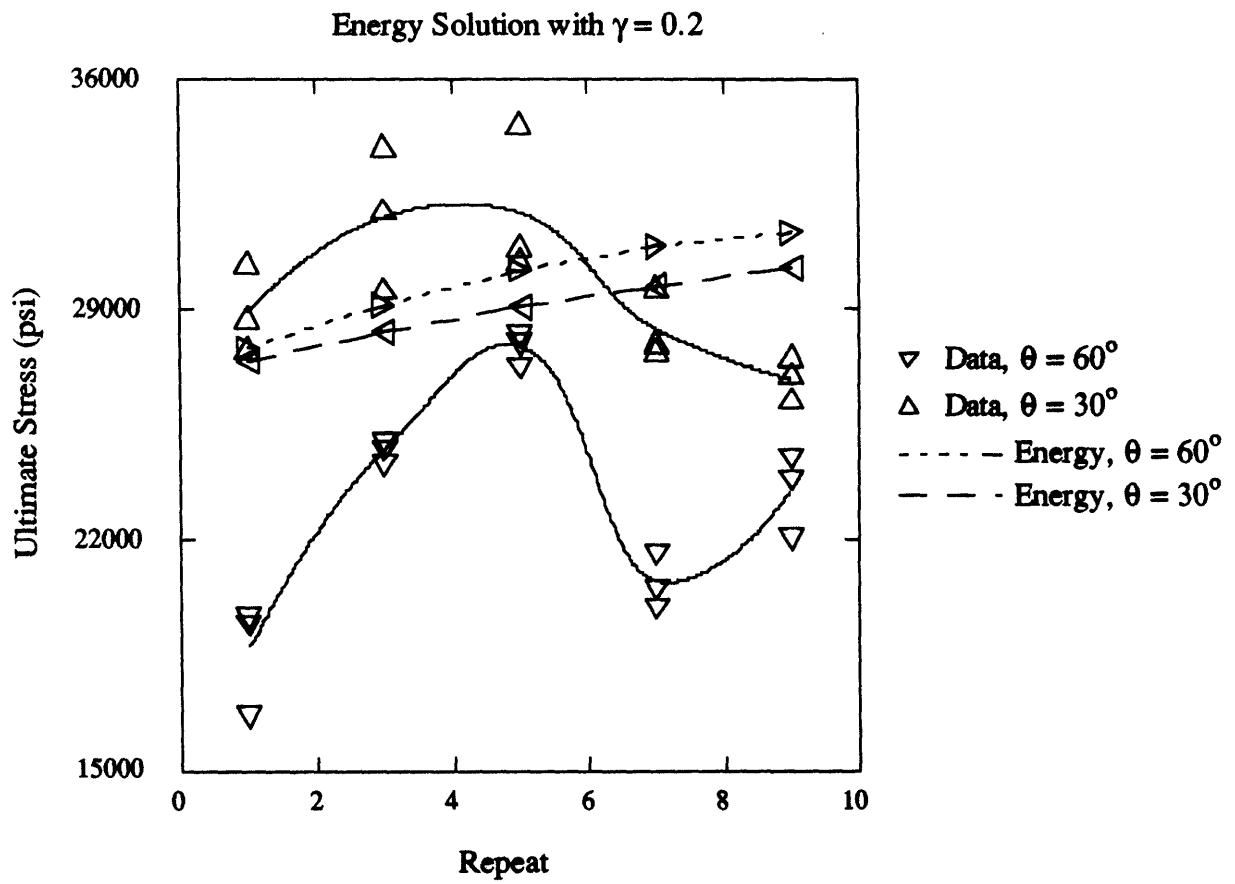
Figure 5-32: Energy Method with $\gamma = 0.2$, for 30° and 60° Cylinders
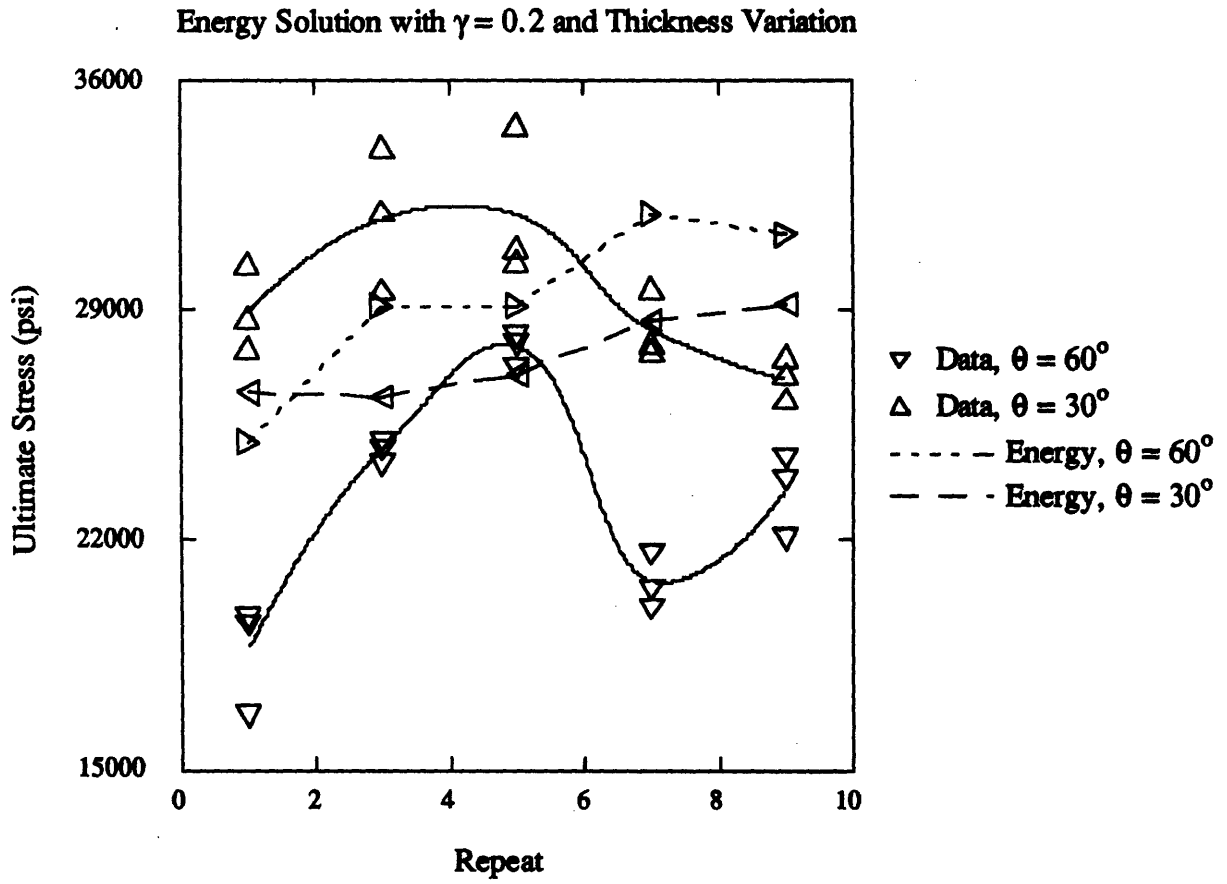
Figure 5-33: Energy Method with $\gamma = 0.2$ and Thickness Variation

increases in **A** and **D**, or to find some other strengthening mechanism which can be incorporated into the mdoel. This analysis will have to wait for a future project.

Since the observed failures all began as localized failures, the ultimate usefulness of these models may be limited. Both the mosaic model and the fiber undulation model use area-averaging of properties as their basis. They "smear out" local material defects and thereby fail to account for any imperfections. An accurate model may have to include these imperfections.

Chapter 6

Conclusions and Recommendations

This thesis began with a list of five specific goals. These goals were stated in the introduction, and are repeated here for convenience:

1. Provide a summary of the literature dealing with the structural analysis of filament-wound composites.

2. Develop a mathematical description of the "degree of interweaving."

3. Show experimentally the effects of interweaving on the compressive strength and modulus of filament-wound cylinders.

4. Determine if a simple model, based on CLPT, can be used to predict these effects.

5. Provide recommendations for developing more complex models in future projects.

The first four goals were accomplished in the earlier chapters; the last will be completed at the end of this chapter. But first, let us summarize the results of this work, and show how they meet the goals listed above.

The first goal was covered in Chapter 2 with a review of the appropriate literature. In accomplishing the third goal, this thesis has added to those earlier works a set of empirical data for axial compressive loads. The current results agree with some of the earlier results:

1. Axial compressive strength increases to a maximum value at moderate values of interweaving, then decreases as the interweaving continues to increase.

2. Interweaving seems to have no effect on the strength of the 45° cylinders. This is related to the observation that the effect of interweaving depends on the failure mode.

3. Interweaving also affects the axial compressive modulus of the cylinders, though the patterns are not as clear as the patterns with strength.

There were also some differences noted in this work:

1. At very high values of interweaving, strength may actually begin to increase again, as observed in the 60° specimens.

2. Some of the variations seen in strength (and perhaps modulus) may be explained by variations in physical parameters, such as thickness.

3. Failure modes under identical loading conditions may vary with different wind angles (though this may have nothing to do with interweaving.).

4. The behavior of the cylinders does not appear to move smoothly from that of an anti-symmetric laminate to that of a homogeneous laminate.

The second goal dealt with the ambiguity in the various definitions of "degree of interweaving." This topic was covered in detail in Chapter 3. Usually interweaving is equated with the term repeat. But the maximum repeat varies with wind angle—for the cylinders wound here, $\mathcal{R}_{max}$ for the 30° cylinders was around 20, whereas $\mathcal{R}_{max}$ for the 60° cylinders was only around 11. The repeat was non-dimensionalized at the end of Chapter 3 by defining the degree of interweaving as

$$\mathcal{I} = \frac{\mathcal{R}}{\mathcal{R}_{max}}$$

Thus, I varied from 0 to 1 for all cylinders.

With this definition of interweaving, some simple failure models were examined, hence accomplishing the fourth goal. Although the simple approaches do not accurately model the observed behavior of the wound composites, they at least give an indication of what factors must be included in more complex models.

The new definition interweaving was incorporated into the mosaic model, an area-averaging modification to lamination theory. The result was an effective bending-stretching coupling

matrix,

$$\bar{\mathbf{B}} = (1 - \mathcal{I})\mathbf{B}$$

The new **B** could then be used in traditional buckling models. The simplest models considered, which are commonly used in practice, are independent of **B** and therefore cannot account for interweaving (at least as it is defined here). A more complex buckling model derived using the energy method was then used. Although it did predict rough failure loads for the 30° and 60° specimens, the interweaving modification could not account for the observed variations in the empirical data.

The fifth and final goal stated above was to provide recommendations for future work. It is appropriate to close with that list:

1. Although more data is needed, the analytical and numerical models should be developed in more detail before further experiments are conducted. Enough data exists to show the general effects that interweaving has on composite behavior, but the mechanisms of those effects are still not understood. We need to know if variations in thickness are more important than, say, void content or bandwidth, so experiments with appropriate controls can be designed.

2. The energy method may still be useful if a mechanism can be found for allowing increases in the **A** and **D** matrices. The crossovers seemed to act as barriers to crack growth, and it may be possible to introduce a factor which accounts for this behavior.

3. Different failure models should be considered. The 45° cylinders failed below their predicted buckling load, indicating a possible material failure (this conclusion is also supported by the lack of variation in failure load with interweaving). Therefore, a tensor or maximum stress/strain failure model may be useful. This would involve solving the governing equations with a finite difference scheme, or developing a finite element model (Appendix C).

4. Variations in physical parameters should be examined in more detail. In particular, the effect of deviations in thickness should be studied. Since all of the ultimate failures began as local failures, these variations in thickness may be very important to understanding

wound composites. Some of the new winding simulation software can output thickness contours of finished parts. This data could be incorporated into a finite element or finite difference solution. Variations in resin and void content should also be examined.

5. The fiber geometry should be modeled more carefully, especially near the crossovers. Most of the failures initiated near the major crossovers, so these regions are of particular importance. The path of the fibers through the woven areas should be documented if possible. These shapes should then be incorporated into the failure models.

6. The peaks in failure load occur at approximately the same repeat values, not interweaving values as expected. This implies that the number and distribution of "diamonds" may be more important than the relative amount of interweaving. An imperfection model, which assumes a distribution shape for imperfections, may be a good choice for future research. Khot's article [23] on the energy solution also includes an imperfection solution. A more complete coverage of the subject is given in [36]; a literature review is given in [37].

Appendix A

Buckling Parameters

The shell buckling equation of Section 4.6.2 (equations 4.48 through 4.51) is given in terms of the functions R_i. These functions depend on the matrices $\mathbf{a}$, $\mathbf{b}$, and $\mathbf{d}$ defined in Section 4.5 (equation 4.31). Because the dependencies are so complex, additional parameters are also defined.

The R_i are

$$R_1 = 1/(H_1^2 - 4aH_2^2)$$

$$R_2 = \frac{1}{2}[H_1 H_3^2/a + H_1 H_4^2 + 4H_2 H_3 H_4]$$

$$R_3 = H_1 a/2$$

$$R_4 = -H_1 H_3 - 2aH_2 H_4$$

$$R_5 = H_5/2a$$

$$R_6 = R_1^2[4H_2^2 + 8aH_2\beta - 2H_1 H_6]$$

$$R_7 = \frac{1}{2}\left[-\frac{1}{a^2}H_1 H_3^2 + 4H_3 H_4\beta + 4H_2 H_3\nu + 4H_2 H_4 H_7 \right.$$
$$\left. +\frac{1}{a}\{H_6 H_3^2 + 2H_1 H_3 H_7\} + H_6 H_4^2 + 2H_1 H_4\nu+\right]$$

$$R_8 = H_1/a + H_6 a/2$$

$$R_9 = -[H_6 H_3 + H_7 H_1 + 2H_2 H_4 + 2\alpha\beta H_4 + 2\alpha\nu H_2]$$

$$R_{10} = -H_5/2a^2 + (1/2a)(2\rho\phi^{1/2} + 2\phi a)$$

$$R_{11} = R_1 R_7 + R_2 R_6 + R_{10}$$

$$R_{12} = R_1 R_8 + R_3 R_6$$

$$R_{13} = R_1 R_9 + R_4 R_6 \qquad \text{(A.1)}$$

The H_i are

$$H_1 = a^2 + a\alpha + 1$$

$$H_2 = \alpha\beta + \gamma$$

$$H_3 = \kappa a^2 + \psi a + \lambda$$

$$H_4 = \nu a + \xi$$

$$H_5 = 1 + 2a\rho\phi^{1/2} + \phi a^2$$

$$H_6 = 2a + \alpha \qquad \text{(A.2)}$$

And the parameters denoted by Greek characters are

$$\alpha = (2a_{1122} + a_{1212})(a_{1111}a_{2222})^{-1/2}$$

$$\beta = a_{2212}a_{1111}^{-1/4}a_{2222}^{-3/4}$$

$$\gamma = a_{1112}a_{2222}^{-1/4}a_{1111}^{-3/4}$$

$$\nu = (2b_{1222} - b_{1112})(a_{2222}d_{2222})^{-1/2} \left(\frac{a_{1111}}{a_{2222}}\right)^{-1/4}$$

$$\xi = (2b_{1211} - b_{2212})(a_{2222}d_{2222})^{-1/2} \left(\frac{a_{2222}}{a_{1111}}\right)^{-1/4}$$

$$\kappa = \frac{b_{1122}}{a_{2222}} \left(\frac{a_{1111}}{d_{2222}}\right)^{1/2}$$

$$\lambda = b_{2211}(a_{1111}d_{2222})^{-1/2}$$

$$\psi = (b_{1111} + b_{2222} - 2b_{1212})(a_{2222}d_{2222})^{-1/2}$$

$$\rho = (d_{1122} + 2d_{1212})(d_{1111}d_{2222})^{-1/2}$$

$$\phi = (a_{1111}d_{1111})/(a_{2222}d_{2222}) \qquad \text{(A.3)}$$

Finally, we get to the buckling parameter a. It is given in citekhot:buck as

$$a = \mu^2 \qquad \text{(A.4)}$$

where

$$\mu = \bar{\mu}(a_{2222}/a_{1111})^{1/4} \tag{A.5}$$

and $\bar{\mu}$ is the wavelength ratio, *i.e.* the number of circumferential waves over the number of axial waves.

Appendix B

Mandrel and Endcap Design

B.1   Mandrel Preparation

Stock aluminum cylinders of about 60 in. length, 2.0 in. outer diameter, and 0.125 in. wall thickness were used for mandrels. Before being used for the first time, the mandrels were sanded with fine sandpaper, washed with alcohol and water, then heated and coated with Carnuba wax.

Before each winding, the mandrels were sprayed with a silicone mold release. Although this is usually enough preparation to allow the composite cylinders to slip off the mandrel once cured, the cylinders would occasionally stick. Therefore, a layer of 3 mil mylar was wrapped around the mandrel, and it in turn was sprayed with mold release.

The composite was wound directly onto the mylar. A hot air gun was used to give the resin some tack and to prevent slipping. After the cylinder was wound, a release film was wrapped over the winding, and then a layer of shrink-tape was wrapped over that (Figure B-1).

The cylinders were then placed in a rotating oven and cured under the following cycle:

1. Ramp up to 210°F over 1 hour.

2. Hold for 1 hour at 210°F.

3. Ramp up to 350°F over 1 hour.

4. Hold for 8 hours[1] at 350°F.

---

[1]Only 2 hours are required for the cure, but a 6 hour post-cure is recommended. It was simply built into the cure cycle.
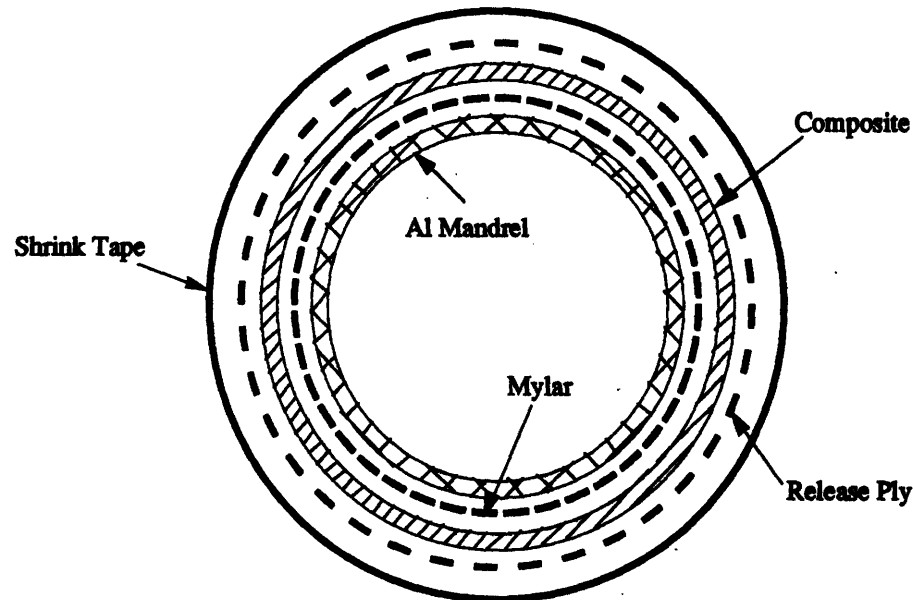
Figure B-1: Cylinder Prepared for Cure

5. Ramp down to room temperature over 4 hours.

The shrink-tape and release film were then removed from the cylinders, and the composite cylinder removed from the mandrel. The mylar would usually slip off with the composite cylinder, but was easily removed from the tube because of the coating of mold release.

Finally, the cylinders were sent to the shop to be ground into 8 in. lengths. The smaller tubes were cut from the center of the large cylinders, avoiding the turn-around regions.

B.2 Endcap Design

Endcaps were made to support the ends of the compression specimens. This prevented end failures and helped assure a more uniform load distribution. The endcaps consist of three parts, as shown in Figures B-2, B-3, and B-4. Figure B-5 shows an endcap assembled on a cylinder.

The plugs fit snugly inside the composite cylinder. The holes in the plugs and rings prevent pressure from building up in the specimen during compression. The inner surface of the ring is slightly angled to give a small inward loading, and thus more firmly grip the cylinder.

A highly viscous, low temperature cure resin was used to bond the endcaps to the test

specimens. Mold release was sprayed on all parts before bonding. After tests were completed, the endcaps were cut off the cylinders and baked at about 500°F to burn off the resin. The endcap parts were then buffed clean using an abrasive pad—3M grill cleaners seemed to work the best.
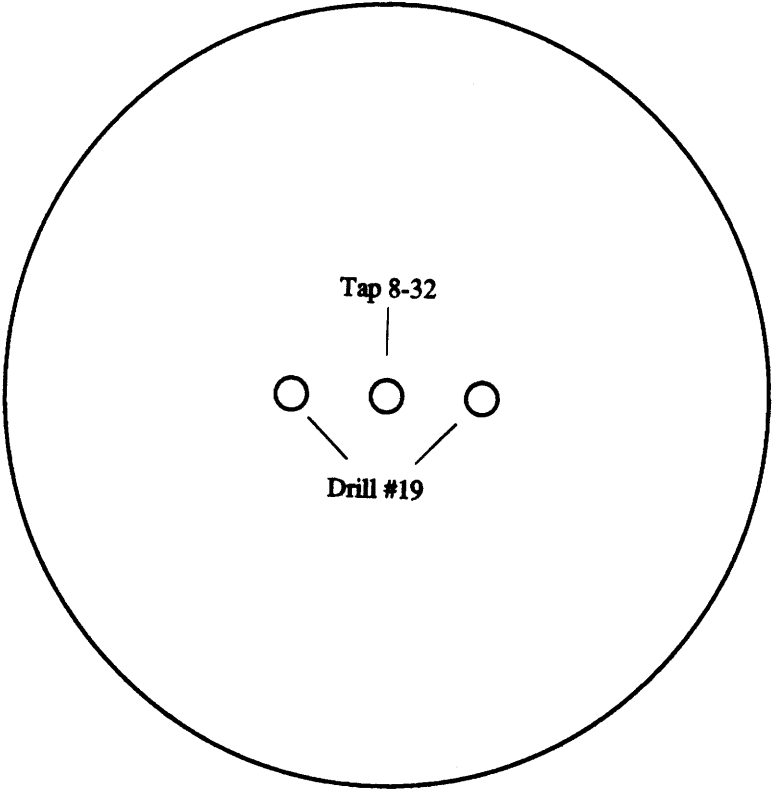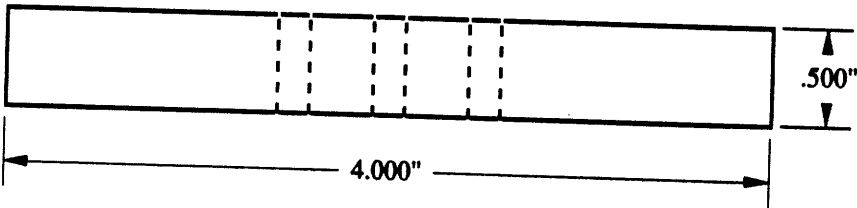
Figure B-2: Endcap Plate

1.000"

2.000"

Drill #19
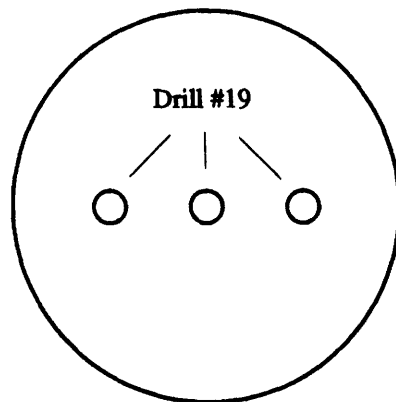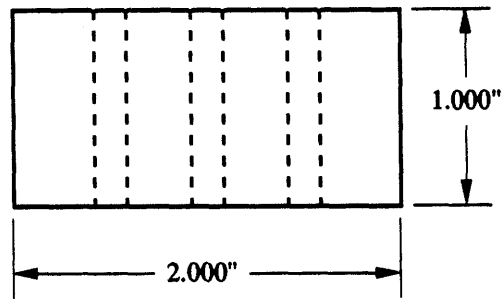
Tolerance = +/-0.1"
Do not need to finish
   rounded face.
Flat faces parallel to
   0.001".

Figure B-3: Endcap Plug
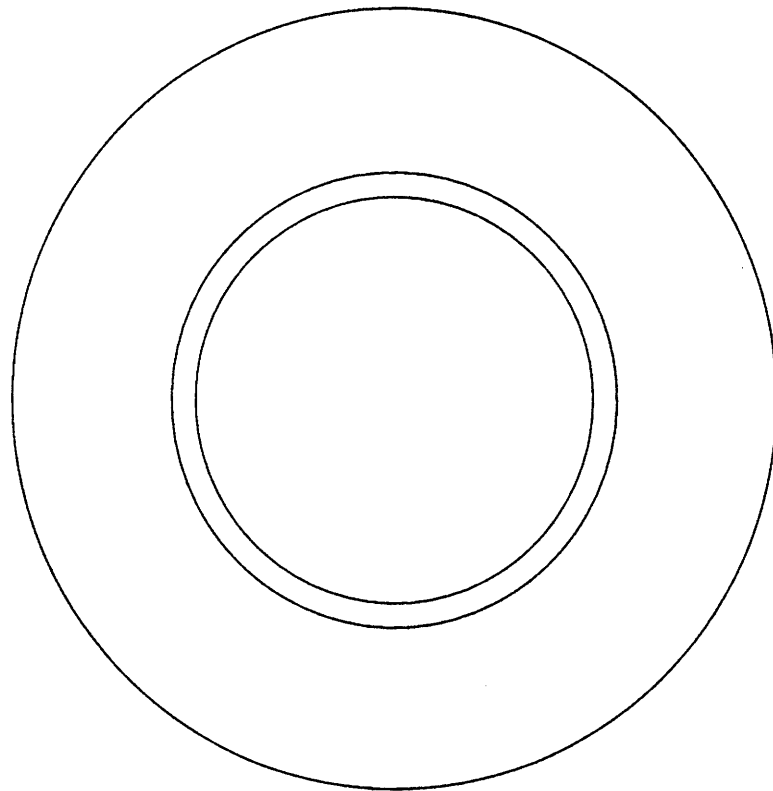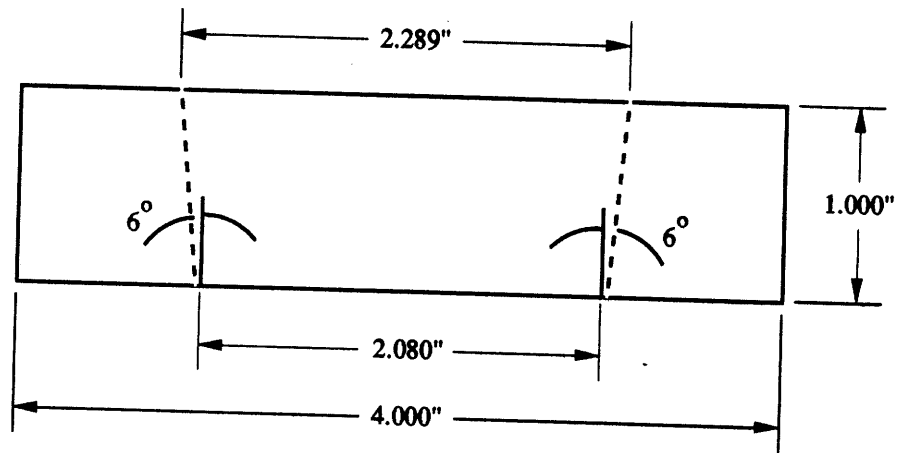
Figure B-4: Endcap Rings
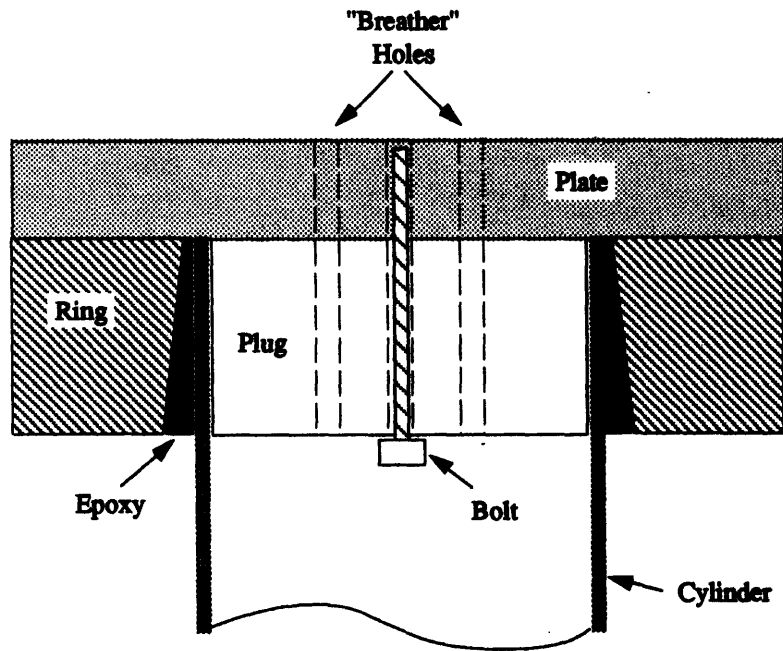
Figure B-5: Assembled Endcap

]

Appendix C

Finite Element Solution

It seemed obvious that a finite element analysis of the filament-wound cylinders should be attempted. However, the software was only available for about a month, so the analysis could not be completed. Some of the preliminary results may be useful for future research, so they are summarized here.

A simple two-dimensional repeating unit was examined under a compressive load. The mesh, loadings, and boundary conditions are shown in Figure C-1. The mosaic model was used, with zero thickness for the crossovers. Eight node quadrilateral and six node triangular composite shell elements were used. Analysis was done with the NISA II/DISPLAY II program.

Two interesting effects were seen on this simple repeating unit:

1. A stress concentration appeared in the center of the unit (Figure C-2[1]).

2. Shear stress was zero along the boundaries between $[\pm\theta]$ and $[\mp\theta]$ layups, where **B** changed signs.

The latter effect was expected, but the former was not. The stress concentration would explain why the cylinders always failed at the major crossovers.

A simple convergence analysis was then performed. As mesh density increased, the size of the stress concentration decreased (though not its magnitude), and the width of the boundary regions between $[\pm\theta]$ and $[\mp\theta]$ layups also decreased. Otherwise, the contours remained fairly constant.

---

[1] Actual stress contour plots were not available for inclusion in this thesis.
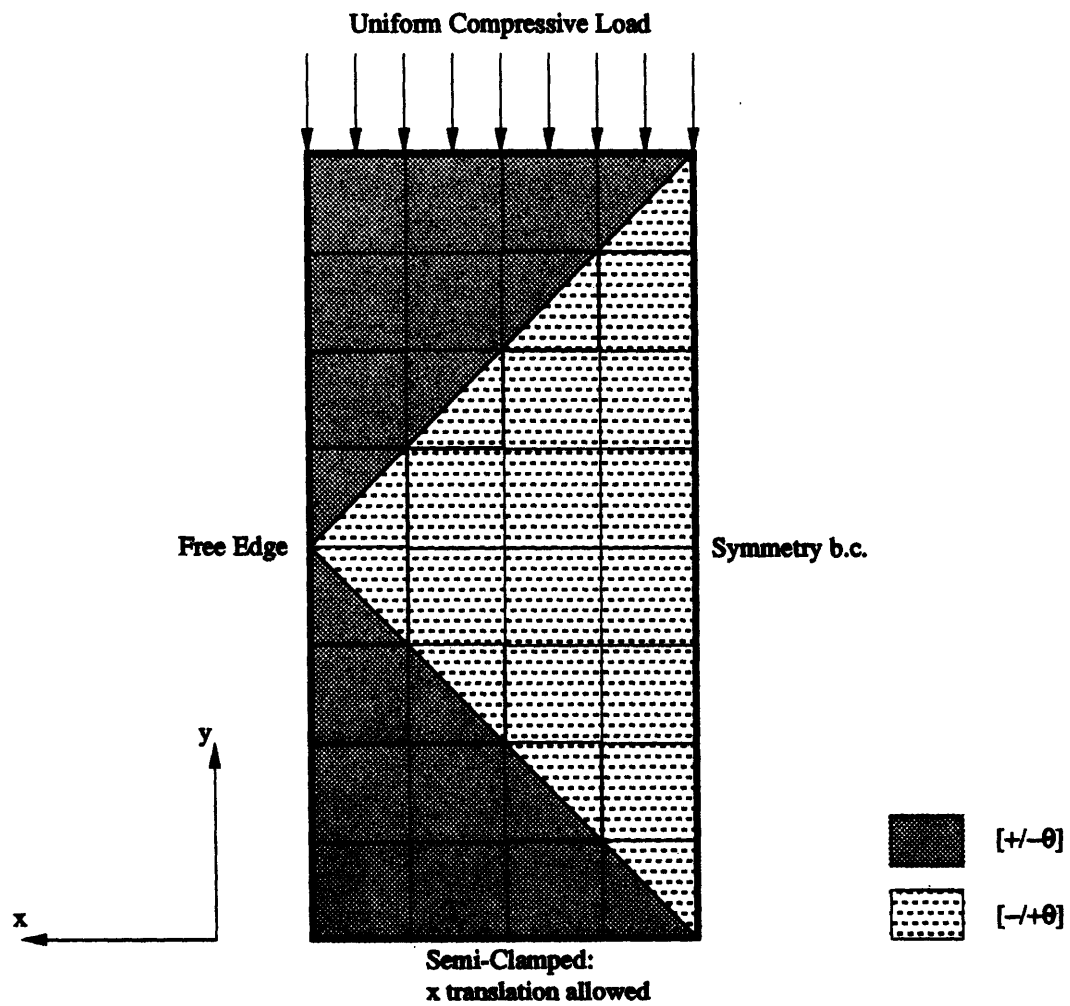
Figure C-1: Repeating Unit Mesh with Boundary Conditions and Loading
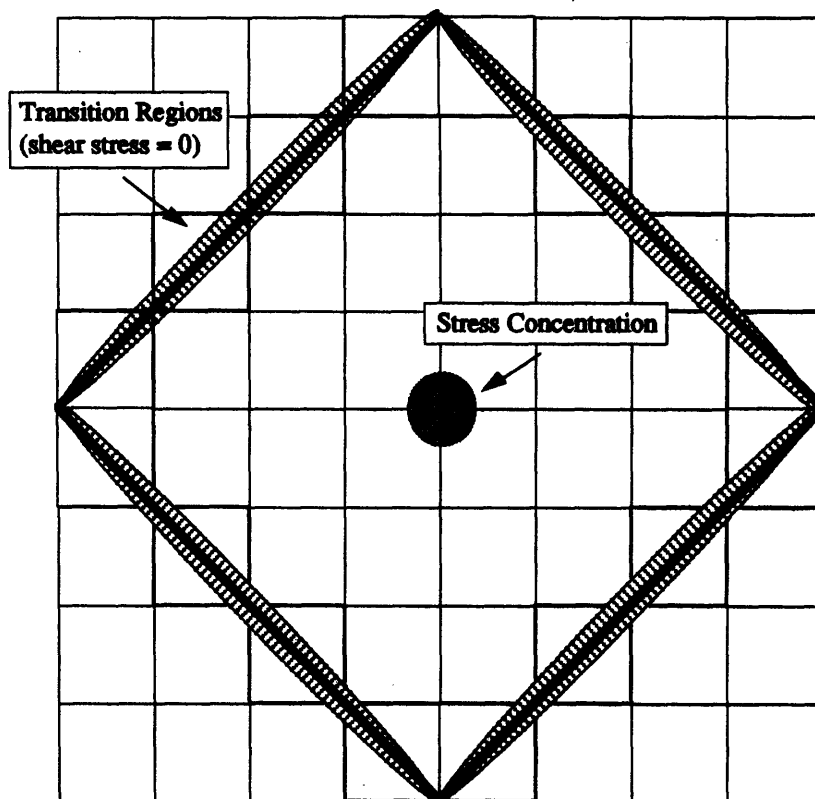
Figure C-2: Simplified Stress Contour of Repeating Unit

To see if the same patterns occurred for higher repeats, a three-by-three "mesh" of repeating units was set up (Figure C-3). Similar contours were observed, with some minor differences along the originally free edges which were now in contact with other repeating units.

Lastly, the three-by-three mesh was mapped onto a cylinder and loaded as in the experiments conducted herein. Surprisingly, the stress concentrations disappeared, and the stress state became almost constant.

At this point, the lease ran out on the software, and no further work could be accomplished[2]. Obviously, much remains to be done with the finite element solution. The meager results presented here at least show the importance of using a cylindrical geometry from the start.

Once a good mesh is developed, it should be possible to create a repeating-unit substructure (or super-element), which can be used for easily meshing different repeats. This was looked at briefly with ABAQUS, using its mapping commands to create a single repeating unit for all wind angles and radii.

The finite element program can then be used to examine the buckling loads of the cylinders. Some programs, such as NISA II, also include composite failure models such as Tsai-Wu and maximum stress.

The finite element method can also be used for micromechanics. If details of the fiber undulations can be determined, then meshed, it may be possible to more accurately model the boundary regions near the crossovers, either with another finite element model or with an analytic model.

---

[2]And just when it was getting interesting!
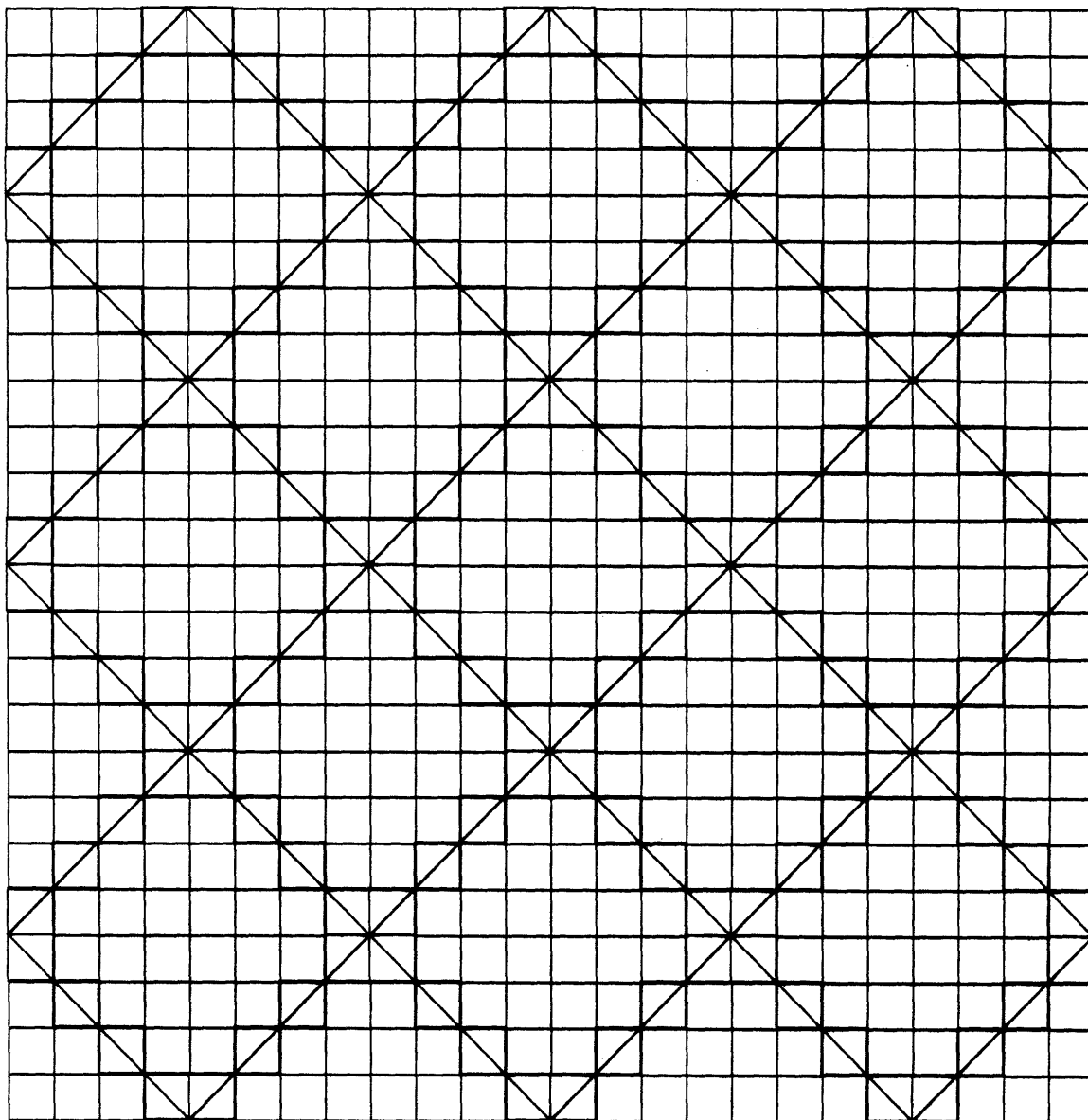
Figure C-3: Mesh for Repeat of Three

Appendix D

FiberGrafiX Software

FiberGrafiX[1] is the name of the software package EnTec distributes with its filament winders. It is used to generate winding patterns with a minimal amount of input.

For this work, the Helical module was used. Winding parameters such as part diameter and wind angle are entered into the program, and FiberGrafiX uses these to generate the fiber path. The program also generates a text file with all of the parameters; a complete listing of these files appears at the end of this appendix.

Some of the parameters, such as turn around distance and headstock dome rotation, are calculated by FiberGrafiX^{TM}, and are not of interest in this work. Other parameters, especially the bandwidth, are entered by the user but may be slightly modified by the program. Table D.1 lists the values of $\mathcal{B}, \mathcal{N}$, and m_2 generated by FiberGrafiX[2].

FiberGrafiX also limits the possible repeats for different bandwidths and wind angles. Wherever possible, programmed angles were kept to the exact values of 30°, 45°, and 60°; in a few cases, however, the angle had to be changed by ±1°. These cases are also listed in table D.1.

---

[1] FiberGrafiX and EnTec are are trademarks of Engineering Technology, Inc.

[2] These are also given in the files at then end of the appendix; they are tabulated here for convenience. Note that FiberGrafiX calls m_2 "K."

138

Tube	$\mathcal{B}$ (in)	$\mathcal{N}$	m_2	$\theta°$
T30R1	0.160041	34	1	30
T30R3	0.160041	34	11	30
T30R5	0.160041	34	7	30
T30R7	0.160041	34	5	30
T30R9	0.160041	34	15	30
T45R1	0.158674	28	1	45
T45R3	0.158674	28	9	45
T45R5	0.158674	28	11	45
T45R7	0.161654	27	23	46
T45R9	0.158674	28	3	45
T60R1	0.179782	18	1	59
T60R3	0.160324	19	6	61
T60R5	0.160324	19	4	61
T60R7	0.160324	19	8	61
T60R9	0.160324	19	2	61

Table D.1: FiberGrafiX$^{\text{TM}}$ Values of $\mathcal{B}$, $\mathcal{N}$, and m_2

D.1 FiberGrafiX Parameter Files

T30R1

```
K (SKIP INDEX) :  1

N (CIRCUITS/LAYER) :  34

NUMBER OF CIRCUITS :  68

NUMBER OF LAYERS :  2

BAND ADVANCE DOMES?(Y/N)   :  YES

M (REVS/CIRC):  7.029412                        DEG


END

BAND WIDTH          :  0.160041                INCHES

BAND THICKNESS      :  0                        INCHES

AXIAL OFFSET (START POSITION) :  10                           INCHES

EYE HEIGHT          :  1                        INCHES

ENVELOPE OFFSET     :  4                        INCHES
```

```
HEADSTOCK DOME ROT :  378.822116                    DEG

TAILSTOCK DOME ROT :  378.822116                    DEG

RADIAL MOTION?(Y/N):  YES

YAW MOTION?(Y/N)   :  NO

Z AXIS MOTION?(Y/N):  NO

WINDING MODE?(P/H)  :  P

FIBER PAYOUT PER SECOND :  18                        INCHES

HEADSTOCK DOME TYPE/FILE :  ELIPSE

TAILSTOCK DOME TYPE/FILE :  ELIPSE

CALC. HEADSTOCK DOME ROT:  478.147908                DEG

CALC. TAILSTOCK DOME ROT:  478.147908                DEG


END

PART DIAMETER  :  2                     INCHES

WIND ANGLE     :  30                     DEG

PART LENGTH :  36                        INCHES

TURN AROUND DISTANCE :  4.60098               INCHES


END
```

T30R3

```
K (SKIP INDEX) :  11

N (CIRCUITS/LAYER) :  34

NUMBER OF CIRCUITS :  68

NUMBER OF LAYERS :  2

BAND ADVANCE DOMES?(Y/N)   :  YES

M (REVS/CIRC):  7.323529                     DEG


END

BAND WIDTH         :  0.160041                    INCHES

BAND THICKNESS     :  0                           INCHES
```

```
AXIAL OFFSET (START POSITION) :  10                        INCHES

EYE HEIGHT          :  1               INCHES

ENVELOPE OFFSET     :  4               INCHES

HEADSTOCK DOME ROT :  431.763292       DEG

TAILSTOCK DOME ROT :  431.763292       DEG

RADIAL MOTION?(Y/N):  YES

YAW MOTION?(Y/N)   :  NO

Z AXIS MOTION?(Y/N):  NO

WINDING MODE?(P/H)   :  P

FIBER PAYOUT PER SECOND :  18               INCHES

HEADSTOCK DOME TYPE/FILE :  ELIPSE

TAILSTOCK DOME TYPE/FILE :  ELIPSE

CALC. HEADSTOCK DOME ROT:  478.147908       DEG

CALC. TAILSTOCK DOME ROT:  478.147908       DEG


END

PART DIAMETER  :  2               INCHES

WIND ANGLE     :  30              DEG

PART LENGTH :  36                 INCHES

TURN AROUND DISTANCE :  4.60098           INCHES


END
```

T30R5

```
K (SKIP INDEX) :  7

N (CIRCUITS/LAYER) :  34

NUMBER OF CIRCUITS :  68

NUMBER OF LAYERS :  2

BAND ADVANCE DOMES?(Y/N)   :  YES

M (REVS/CIRC):  7.205882             DEG
```

END

BAND WIDTH   : 0.160041   INCHES

BAND THICKNESS   : 0   INCHES

AXIAL OFFSET (START POSITION) : 10   INCHES

EYE HEIGHT   : 1   INCHES

ENVELOPE OFFSET   : 4   INCHES

HEADSTOCK DOME ROT : 410.586822   DEG

TAILSTOCK DOME ROT : 410.586822   DEG

RADIAL MOTION?(Y/N): YES

YAW MOTION?(Y/N)   : NO

Z AXIS MOTION?(Y/N): NO

WINDING MODE?(P/H)   : P

FIBER PAYOUT PER SECOND : 18   INCHES

HEADSTOCK DOME TYPE/FILE : ELIPSE

TAILSTOCK DOME TYPE/FILE : ELIPSE

CALC. HEADSTOCK DOME ROT: 478.147908   DEG

CALC. TAILSTOCK DOME ROT: 478.147908   .   DEG

END

PART DIAMETER   : 2   INCHES

WIND ANGLE   : 30   DEG

PART LENGTH : 36   INCHES

TURN AROUND DISTANCE : 4.60098   INCHES

END
_____

T30R7

K (SKIP INDEX) : 5

N (CIRCUITS/LAYER) : 34

NUMBER OF CIRCUITS : 68

NUMBER OF LAYERS : 2

```
BAND ADVANCE DOMES?(Y/N)    :  YES
M (REVS/CIRC):  7.147059                        DEG


END
BAND WIDTH          :  0.160041                 INCHES
BAND THICKNESS      :  0                        INCHES
AXIAL OFFSET (START POSITION) :  10                         INCHES
EYE HEIGHT          :  1                        INCHES
ENVELOPE OFFSET     :  4                        INCHES
HEADSTOCK DOME ROT  :  399.998586               DEG
TAILSTOCK DOME ROT  :  399.998586               DEG
RADIAL MOTION?(Y/N):  YES
YAW MOTION?(Y/N)    :  NO
Z AXIS MOTION?(Y/N):  NO
WINDING MODE?(P/H)    :  P
FIBER PAYOUT PER SECOND :  18                   INCHES
HEADSTOCK DOME TYPE/FILE :  ELIPSE
TAILSTOCK DOME TYPE/FILE :  ELIPSE
CALC. HEADSTOCK DOME ROT:  478.147908           DEG
CALC. TAILSTOCK DOME ROT:  478.147908           DEG


END
PART DIAMETER   :  2                    INCHES
WIND ANGLE      :  30                   DEG
PART LENGTH :  36                       INCHES
TURN AROUND DISTANCE :  4.60098             INCHES


END
```

T30R9

```
K (SKIP INDEX) :  15
```

N (CIRCUITS/LAYER) :   34

NUMBER OF CIRCUITS :   68

NUMBER OF LAYERS :   2

BAND ADVANCE DOMES?(Y/N)   :   YES

M (REVS/CIRC):   7.441176   DEG

END

BAND WIDTH   :   0.160041   INCHES

BAND THICKNESS   :   0   INCHES

AXIAL OFFSET (START POSITION) :   10   INCHES

EYE HEIGHT   :   1   INCHES

ENVELOPE OFFSET   :   4   INCHES

HEADSTOCK DOME ROT :   452.939763   DEG

TAILSTOCK DOME ROT :   452.939763   DEG

RADIAL MOTION?(Y/N):   YES

YAW MOTION?(Y/N)   :   NO

Z AXIS MOTION?(Y/N):   NO

WINDING MODE?(P/H)   :   P

FIBER PAYOUT PER SECOND :   18   INCHES

HEADSTOCK DOME TYPE/FILE :   ELIPSE

TAILSTOCK DOME TYPE/FILE :   ELIPSE

CALC. HEADSTOCK DOME ROT: 478.147908   DEG

CALC. TAILSTOCK DOME ROT: 478.147908   DEG

END

PART DIAMETER   :   2   INCHES

WIND ANGLE   :   30   DEG

PART LENGTH :   36   INCHES

TURN AROUND DISTANCE :   4.60098   INCHES

END
_____

T45R1

K (SKIP INDEX) : 1

N (CIRCUITS/LAYER) : 28

NUMBER OF CIRCUITS : 56

NUMBER OF LAYERS : 2

BAND ADVANCE DOMES?(Y/N) : YES

M (REVS/CIRC): 11.035714   DEG

END

BAND WIDTH   : 0.158674   INCHES

BAND THICKNESS   : 0   INCHES

AXIAL OFFSET (START POSITION) : 10   INCHES

EYE HEIGHT   : 1   INCHES

ENVELOPE OFFSET   : 4   INCHES

HEADSTOCK DOME ROT : 499.030708   DEG

TAILSTOCK DOME ROT : 499.030708   DEG

RADIAL MOTION?(Y/N): YES

YAW MOTION?(Y/N)   : NO

Z AXIS MOTION?(Y/N): NO

WINDING MODE?(P/H)   : P

FIBER PAYOUT PER SECOND : 18   INCHES

HEADSTOCK DOME TYPE/FILE : ELIPSE

TAILSTOCK DOME TYPE/FILE : ELIPSE

CALC. HEADSTOCK DOME ROT: 543.6009   DEG

CALC. TAILSTOCK DOME ROT: 543.6009   DEG

END

PART DIAMETER   : 2   INCHES

WIND ANGLE   : 45   DEG

PART LENGTH : 32   INCHES

TURN AROUND DISTANCE : 3.020005   INCHES

END

_____

T45R3

K (SKIP INDEX) : 9

N (CIRCUITS/LAYER) : 28

NUMBER OF CIRCUITS : 56

NUMBER OF LAYERS : 2

BAND ADVANCE DOMES?(Y/N)   : YES

M (REVS/CIRC): 11.321429   DEG

END

BAND WIDTH   : 0.158674   INCHES

BAND THICKNESS   : 0   INCHES

AXIAL OFFSET (START POSITION) : 10   INCHES

EYE HEIGHT   : 1   INCHES

ENVELOPE OFFSET   : 4   INCHES

HEADSTOCK DOME ROT : 550.45928   DEG

TAILSTOCK DOME ROT : 550.45928   DEG

RADIAL MOTION?(Y/N): YES

YAW MOTION?(Y/N)   : NO

Z AXIS MOTION?(Y/N): NO

WINDING MODE?(P/H)   : P

FIBER PAYOUT PER SECOND : 18   INCHES

HEADSTOCK DOME TYPE/FILE : ELIPSE

TAILSTOCK DOME TYPE/FILE : ELIPSE

CALC. HEADSTOCK DOME ROT: 543.6009   DEG

CALC. TAILSTOCK DOME ROT: 543.6009   DEG

```
END
PART DIAMETER  :  2                                    INCHES
WIND ANGLE     :  45                          DEG
PART LENGTH :  32                             INCHES
TURN AROUND DISTANCE :  3.020005                        INCHES


END
```

T45R5

```
K (SKIP INDEX) :  11
N (CIRCUITS/LAYER) :  28
NUMBER OF CIRCUITS :  56
NUMBER OF LAYERS :  2
BAND ADVANCE DOMES?(Y/N)   :  YES
M (REVS/CIRC):  11.392857                     DEG


END
BAND WIDTH        :  0.158674                 INCHES
BAND THICKNESS    :  0                        INCHES
AXIAL OFFSET (START POSITION) :  10                     INCHES
EYE HEIGHT        :  1                        INCHES
ENVELOPE OFFSET   :  4                        INCHES
HEADSTOCK DOME ROT :  476.799681              DEG
TAILSTOCK DOME ROT :  476.799681              DEG
RADIAL MOTION?(Y/N):  YES
YAW MOTION?(Y/N)   :  NO
Z AXIS MOTION?(Y/N):  NO
WINDING MODE?(P/H)   :  P
FIBER PAYOUT PER SECOND :  18                      INCHES
HEADSTOCK DOME TYPE/FILE :  ELIPSE
TAILSTOCK DOME TYPE/FILE :  ELIPSE
```

CALC. HEADSTOCK DOME ROT: 407.70072   DEG

CALC. TAILSTOCK DOME ROT: 407.70072   DEG

END

PART DIAMETER : 2   INCHES

WIND ANGLE   : 45   DEG

PART LENGTH : 32   INCHES

TURN AROUND DISTANCE : 2.265004   INCHES

END
_____

T45R7

K (SKIP INDEX) : 23

N (CIRCUITS/LAYER) : 27

NUMBER OF CIRCUITS : 54

NUMBER OF LAYERS : 2

BAND ADVANCE DOMES?(Y/N)   : YES

M (REVS/CIRC): 11.851852   DEG

END

BAND WIDTH   : 0.161654   INCHES

BAND THICKNESS   : 0   INCHES

AXIAL OFFSET (START POSITION) : 10   INCHES

EYE HEIGHT   : 1   INCHES

ENVELOPE OFFSET   : 4   INCHES

HEADSTOCK DOME ROT : 593.087757   DEG

TAILSTOCK DOME ROT : 593.087757   DEG

RADIAL MOTION?(Y/N): YES

YAW MOTION?(Y/N)   : NO

Z AXIS MOTION?(Y/N): NO

WINDING MODE?(P/H)   : P

FIBER PAYOUT PER SECOND : 18   INCHES

HEADSTOCK DOME TYPE/FILE : ELIPSE

TAILSTOCK DOME TYPE/FILE : ELIPSE

CALC. HEADSTOCK DOME ROT: 562.915211   DEG

CALC. TAILSTOCK DOME ROT: 562.915211   DEG

END

PART DIAMETER : 2   INCHES

WIND ANGLE   : 46   DEG

PART LENGTH : 32   INCHES

TURN AROUND DISTANCE : 3.020005   INCHES

END
_____

T45R9

K (SKIP INDEX) : 3

N (CIRCUITS/LAYER) : 28

NUMBER OF CIRCUITS : 84

NUMBER OF LAYERS : 2

BAND ADVANCE DOMES?(Y/N)   : YES

M (REVS/CIRC): 11.107143   DEG

END

BAND WIDTH   : 0.158674   INCHES

BAND THICKNESS   : 0   INCHES

AXIAL OFFSET (START POSITION) : 10   INCHES

EYE HEIGHT   : 1   INCHES

ENVELOPE OFFSET   : 4   INCHES

HEADSTOCK DOME ROT : 425.371109   DEG

TAILSTOCK DOME ROT : 425.371109   DEG

RADIAL MOTION?(Y/N): YES

```
YAW MOTION?(Y/N)    :  NO

Z AXIS MOTION?(Y/N):  NO

WINDING MODE?(P/H)    :  P

FIBER PAYOUT PER SECOND :  18                          INCHES

HEADSTOCK DOME TYPE/FILE :  ELIPSE

TAILSTOCK DOME TYPE/FILE :  ELIPSE

CALC. HEADSTOCK DOME ROT:  407.70072                   DEG

CALC. TAILSTOCK DOME ROT:  407.70072                   DEG


END

PART DIAMETER   :  2                      INCHES

WIND ANGLE      :  45                     DEG

PART LENGTH :  32                         INCHES

TURN AROUND DISTANCE :  2.265004              INCHES


END
```

T60R1

```
K (SKIP INDEX) :  1

N (CIRCUITS/LAYER) :  18

NUMBER OF CIRCUITS :  36

NUMBER OF LAYERS :  2

BAND ADVANCE DOMES?(Y/N)    :  YES

M (REVS/CIRC):  17.055556                  DEG


END

BAND WIDTH         :  0.179782                   INCHES

BAND THICKNESS     :  0                          INCHES

AXIAL OFFSET (START POSITION) :  10                      INCHES

EYE HEIGHT         :  1                          INCHES

ENVELOPE OFFSET    :  4                          INCHES
```

```
HEADSTOCK DOME ROT :   539.304115                          DEG

TAILSTOCK DOME ROT :   539.304115                          DEG

RADIAL MOTION?(Y/N):   YES

YAW MOTION?(Y/N)   :   NO

Z AXIS MOTION?(Y/N):   NO

WINDING MODE?(P/H)   :   P

FIBER PAYOUT PER SECOND :   18                      INCHES

HEADSTOCK DOME TYPE/FILE :   ELIPSE

TAILSTOCK DOME TYPE/FILE :   ELIPSE

CALC. HEADSTOCK DOME ROT:   518.346802          .          DEG

CALC. TAILSTOCK DOME ROT:   518.346802                     DEG


END

PART DIAMETER   :   2                            INCHES

WIND ANGLE     :   59                            DEG

PART LENGTH :   30                               INCHES

TURN AROUND DISTANCE :   1.730301                    INCHES


END
```

T60R3

```
K (SKIP INDEX) :   6

N (CIRCUITS/LAYER) :   19

NUMBER OF CIRCUITS :   38

NUMBER OF LAYERS :   2

BAND ADVANCE DOMES?(Y/N)   :   YES

M (REVS/CIRC):   18.315789                      DEG


END

BAND WIDTH         :   0.160324                 INCHES

BAND THICKNESS     :   0                        INCHES
```

```
AXIAL OFFSET (START POSITION) :  10                          INCHES

EYE HEIGHT          :  1                      INCHES

ENVELOPE OFFSET     :  4                      INCHES

HEADSTOCK DOME ROT :   553.615213             DEG

TAILSTOCK DOME ROT :   553.615213             DEG

RADIAL MOTION?(Y/N):  YES

YAW MOTION?(Y/N)   :  NO

Z AXIS MOTION?(Y/N):  NO

WINDING MODE?(P/H)   :  P

FIBER PAYOUT PER SECOND :  18                      INCHES

HEADSTOCK DOME TYPE/FILE :  ELIPSE

TAILSTOCK DOME TYPE/FILE :  ELIPSE

CALC. HEADSTOCK DOME ROT:  561.878214             DEG

CALC. TAILSTOCK DOME ROT:  561.878214             DEG


END

PART DIAMETER   :  2                      INCHES

WIND ANGLE    :  61                       DEG

PART LENGTH :  30                     INCHES

TURN AROUND DISTANCE :  1.730301              INCHES


END
```

T60R5

```
K (SKIP INDEX) :  4

N (CIRCUITS/LAYER) :  19

NUMBER OF CIRCUITS :  38

NUMBER OF LAYERS :  2

BAND ADVANCE DOMES?(Y/N)   :   YES

M (REVS/CIRC): 18.210526                  DEG
```

END

BAND WIDTH	: 0.160324	INCHES
BAND THICKNESS	: 0	INCHES
AXIAL OFFSET (START POSITION) : 10		INCHES
EYE HEIGHT	: 1	INCHES
ENVELOPE OFFSET	: 4	INCHES
HEADSTOCK DOME ROT :	534.667845	DEG
TAILSTOCK DOME ROT :	534.667845	DEG
RADIAL MOTION?(Y/N):	YES	
YAW MOTION?(Y/N) :	NO	
Z AXIS MOTION?(Y/N):	NO	
WINDING MODE?(P/H) :	P	
FIBER PAYOUT PER SECOND :	18	INCHES
HEADSTOCK DOME TYPE/FILE :	ELIPSE	
TAILSTOCK DOME TYPE/FILE :	ELIPSE	
CALC. HEADSTOCK DOME ROT:	561.878214	DEG
CALC. TAILSTOCK DOME ROT:	561.878214	DEG

END

PART DIAMETER :	2	INCHES
WIND ANGLE :	61	DEG
PART LENGTH :	30	INCHES
TURN AROUND DISTANCE :	1.730301	INCHES

END

T60R7

K (SKIP INDEX) : 8

N (CIRCUITS/LAYER) : 19

NUMBER OF CIRCUITS : 38

NUMBER OF LAYERS : 2

```
BAND ADVANCE DOMES?(Y/N)    :  YES
M (REVS/CIRC):  18.421053                        DEG


END
BAND WIDTH           :  0.160324                 INCHES
BAND THICKNESS       :  0                        INCHES
AXIAL OFFSET (START POSITION) :  10                     INCHES
EYE HEIGHT           :  1                       · INCHES
ENVELOPE OFFSET      :  4                         INCHES
HEADSTOCK DOME ROT :  572.562582                 DEG
TAILSTOCK DOME ROT :  572.562582                 DEG
RADIAL MOTION?(Y/N):  YES
YAW MOTION?(Y/N)    :  NO
Z AXIS MOTION?(Y/N):  NO
WINDING MODE?(P/H)   :  P
FIBER PAYOUT PER SECOND :  18                      INCHES
HEADSTOCK DOME TYPE/FILE :  ELIPSE
TAILSTOCK DOME TYPE/FILE :  ELIPSE
CALC. HEADSTOCK DOME ROT:  561.878214             DEG
CALC. TAILSTOCK DOME ROT:  561.878214             DEG


END
PART DIAMETER  :  2                        INCHES
WIND ANGLE     :  61                       DEG
PART LENGTH :  30                       INCHES
TURN AROUND DISTANCE :  1.730301               INCHES


END
```

T60R9

```
K (SKIP INDEX) :  2
```

```
N (CIRCUITS/LAYER) :  19

NUMBER OF CIRCUITS :  38

NUMBER OF LAYERS :  2

BAND ADVANCE DOMES?(Y/N)   :  YES

M (REVS/CIRC):  18.105263                    DEG


END

BAND WIDTH          :  0.160324                    INCHES

BAND THICKNESS    :  0                              INCHES

AXIAL OFFSET (START POSITION) :  10                          INCHES

EYE HEIGHT          :  1                         INCHES

ENVELOPE OFFSET    :  4                          INCHES

HEADSTOCK DOME ROT :  515.720477                 DEG

TAILSTOCK DOME ROT :  515.720477                 DEG

RADIAL MOTION?(Y/N):  YES

YAW MOTION?(Y/N)    :  NO

Z AXIS MOTION?(Y/N):  NO

WINDING MODE?(P/H)    :  P

FIBER PAYOUT PER SECOND :  18                        INCHES

HEADSTOCK DOME TYPE/FILE :  ELIPSE

TAILSTOCK DOME TYPE/FILE :  ELIPSE

CALC. HEADSTOCK DOME ROT:  561.878214                DEG

CALC. TAILSTOCK DOME ROT:  561.878214                DEG


END

PART DIAMETER   :  2                         INCHES

WIND ANGLE    :  61                          DEG

PART LENGTH :  30                            INCHES

TURN AROUND DISTANCE :  1.730301                 INCHES
```

END

Bibliography

[1] Fernando M. Brito. Influence of interwoven configuration on mechanical properties of crossed helicoidal filament winding composites. In F. L. Matthews, N. C. R. Buskell, J. M. Hodgkinson, and J. Morton, editors, *Sixth International Conference on Composite Materials*, pages 1.183–1.189, London and New York, June 1987. ICCM & ECCM, Elsevier Applied Science.

[2] V. N. Bulmanis and Yu. I. Gusev. Tensile strength of wound polyester fiberglass. *Mechanics of Composite Materials*, pages 39–42, July 1983. Translated from *Mekhanika Kompozitnykh Materialov*, Vol. 19, No. 1, January-February, 1983, pp. 47-51.

[3] V. N. Bulmanis, Yu. I. Gusev, A. S. Struchkov, and B. Antokhonov. Experimental examination of the special features of deformation and failure in tensile loading of cross-reinforced wound composites. *Mechanics of Composite Materials*, pages 694–698, January 1986. Translated from *Mekhanika Kompozitnykh Materialov*, Vol. 21, No. 6, November-December, 1985, pp. 1020-1024.

[4] Lee R. Calcote. *The Analysis of Laminated Composite Structures*. Van Nostrand Reinhold Company, New York, 1969.

[5] Christos C. Chamis. Simplified composite micromechanics equations for hygral, thermal, and mechanical properties. *SAMPE Quarterly*, pages 14–23, April 1984.

[6] S. Cheng and B. P. C. Ho. Stability of heterogeneous aeolotropic cylindrical shells under combined loading. *AIAA Journal*, 1(4):892–898, April 1963.

[7] Choon T. Chon. Analysis of tubular lap joint in torsion. *Journal of Composite Materials*,

16:268–284, July 1982.

[8] L. Collatz. *The Numerical Treatment of Differential Equations*. Springer Verlag, 1966.

[9] S. B. Dong, R. B. Matthiesen, K. S. Pister, and T. L. Taylor. Analysis of structural laminates. Technical Report ARL 76, Aeronautical Research Laboratory, Office of Aerospace Research, United States Air Force, Wright-Patterson Air FOrce Base, Ohio, September 1961.

[10] L. H. Donnell. Stability of thin-walled tubes under torsion. Technical Report Report No. 479, N.A.C.A., 1933.

[11] Geoffrey Charles Eckold. *An Investigation into the Strength and Elastic Properties of Filament Wound Composites*. PhD thesis, Victoria University of Manchester, September 1978.

[12] Engineering Technology, Inc., Salt Lake City, Utah. *FiberGrafiX Reference Manual*, 1989.

[13] A. A. Filipenko, A. F. Ermolenko, and V. D. Protasov. Analysis of weight optimization of spiral-annular-wound cylindrical shells with layers having different physicomechanical characteristics. *Mechanics of Composite Materials*, pages 467–475, November 1987. Translated from *Mekhanika Kompozitnykh Materialov*, Vol. 23, No. 3, May-June, 1987, pp. 464-471.

[14] A. N. Garde and S. C. Lakkad. Experimental studies on the instability of axially loaded cylindrical frp shells. In *Proceedings of the V International Congress on Experimental Mechanics*, pages 92–95, Montreal, June 1984. SESA.

[15] Philip J. Hipol. Analysis and optimization of a tubular lap joint subjected to torsion. *Journal of Composite Materials*, 18:298–311, July 1984.

[16] S. V. Hoa, C. W. Yu, and T. S. Sankar. Analysis of filament wound vessel using finite elements. *Composite Structures*, 3:1–18, 1985.

[17] T. Ishikawa and T.-W. Chou. Stiffness and strength behaviour of woven fabric composites. *Journal of Materials Science*, 17:3211–3220, 1982.

[18] T. Ishikawa and T. W. Chou. Stiffness and strength properties of woven composites. In S. Umekawa T. Hayashi, editor, *Progress in Science and Engineering of COmposites*, pages 489–496, Tokyo, 1982. ICCM.

[19] Takashi Ishikawa. Anti-symmetric elastic properties of composite plates of satin weave cloth. *Fibre Science and Technology*, 15:127–145, 1981.

[20] Takashi Ishikawa and Tsu-Wei Chou. Elastic behavior of woven hybrid composites. *Journal of Composite Materials*, 16:2–19, January 1982.

[21] Takashi Ishikawa and Tsu-Wei Chou. One-dimensional micromechanical analysis of woven fabric composites. *AIAA Journal*, 21(12):1714–1721, December 1983.

[22] V. V. Khitrov and Yu. I. Katarzhnov. Effect of the angle of reinforcement on the carrying capacity of wound tubes in compression. *Mechanics of Composite Materials*, pages 372–376, January 1980. Translated from *Mekhanika Kompozitnykh Materialov*, Vol. 15, No. 4, July-August, 1979, pp. 611-616.

[23] N. S. Khot. Buckling and postbuckling behavior of composite cylindrical shells under axial compression. *AIAA Journal*, 8(2):229–235, February 1970.

[24] V. N. Kiselev, S. S. Abramchuk, I. P. Dimitrienko, and V. D. Protasov. Diagnosing the load-bearing capacity of helically tangentially wound cylindrical shells. *Mechanics of Composite Materials*, pages 112–115, July 1985. Translated from *Mekhanika Kompozitnykh Materialov*, Vol. 21, No. 1, January-February, 1985, pp. 138-142.

[25] S. G. Lekhnitskii. *Theory of Elasticity of an Anisotropic Elastic Body*. Holden-Day, Inc., San Francisco, 1963. Translated by P. Fern.

[26] Xian li Li and Dao hai Lin. Non-geodesic winding equations on a general surface of revolution. In F. L. Matthews, N. C. R. Buskell, J. M. Hodgkinson, and J. Morton, editors, *Sixth International Conference on Composite Materials*, pages 1.152–1.160, London and New York, June 1987. ICCM & ECCM, Elsevier Applied Science.

[27] NASA. Buckling of thin-walled circular cylinders. Technical Report NASA SP-8007, National Aeronautics and Space Administration, 1965.

[28] N. J. Pagano, J. C. Halpin, and J. M. Whitney. Tension buckling of anisotropic cylinders. *Journal of Composite Materials*, 2(2):154–167, April 1968.

[29] N. J. Pagano and J. M. Whitney. Geometric design of composite cylindrical characterization specimens. *Journal of Composite Materials*, 4:360–378, July 1970.

[30] S. T. Peters. Filament winding. In *Engineered Materials Handbook Volume 1: Composites*, pages 503–518. ASM International, 1987.

[31] Stanley T. Peters and Brian E. Spencer. Filament winding composite structure fabrication. Technical report, SAMPE, 1989.

[32] Johnny L. Prater and Robert M. Hackett. Viscoelastic/damage modeling of filament-wound cylindrical pressure vessels. In *Composite Materials: Testing and Design (Eighth Conference)*, pages 401–412. ASTM, 1988. STP 972.

[33] V. D. Protasov and A. F. Ermolenko. Problems of the strength of shell designs fashioned from wound composites. *Mechanics of Composite Materials*, pages 756–764, January 1984. Translated from *Mekhanika Kompozitnykh Materialov*, Vol. 19, No. 6, November-December, 1983, pp. 1034-1043.

[34] L. N. Seleznev, V. N. Kinevskii, and Z. I. Miloslavskii. Investigation of the principal dense-winding conditions for wound glass-reinforced plastic pipe. *Polymer Mechanics*, pages 920–925, June 1973. Translated from *Mekhanika Polimerov*, Vol. 6, No. 6, Novembe-December, 1970, pp. 1057-1064.

[35] Robert E. Sherrer. Filament-wound cylinders with axial-symmetric loads. *Journal of Composite Materials*, 1:344–355, 1967.

[36] G. J. Simitses, D. Shaw, and I. Sheinman. Imperfection sensitivity of laminated cylindrical shells in torsion and axial compression. *Composite Structures*, 4:335–360, 1985.

[37] George J. Simitses. Buckling and postbuckling of imperfect cylindrical shells: A review. *Applied Mechanics Reviews*, 39(10):1517–1524, October 1986.

[38] Kiyohisa Takahashi, Kikuo Ban, and Tetsuya Sakai. Mechanical properties of frp-fw pipes. *Composite Strucutres*, 2:91–104, 1984.

[39] Stephen W. Tsai. *Composites Design*. Think Composites, Dayton, 4 edition, 1988.

[40] Stephen W. Tsai and H. Thomas Hahn. *Introduction to Composite Materials*. Technomic Publishing Company, Inc., Lancaster, PA, 1980.

[41] M. Uemura and H. Fukunaga. Probabilistic burst strength of filament-wound cylinders under internal pressure. *Journal of Composite Materials*, 15:462–480, September 1981.

[42] J. R. Vinson and R. L. Sierakowski. *The Behavior of Structures Composed of Composite Materials*. Martinus Nijhoff Publishers, 1987.

[43] G. M. Wells and K. F. McAnulty. Computer aided filament winding using non-geodesic trajectories. In F. L. Matthews, N. C. R. Buskell, J. M. Hodgkinson, and J. Morton, editors, *Sixth International Conference on Composite Materials*, pages 1.161–1.173, London and New York, June 1987. ICCM & ECCM, Elsevier Applied Science.

[44] A. M. Zakrzhevskii and V. V. Khitrov. Effect of interweaving on the load-carrying capacity of wound thick-walled rods of composites in torsion. *Mechanics of Composite Materials*, pages 516–523, January 1989. Translated from *Mekhanika Kompozitnykh Materialov*, Vol. 24, No. 4, July-August, 1988, pp. 676-683.

This thesis was prepared entirely on a Macintosh SE, using LaTeX for typesetting. Body fonts are from the Computer Modern font family; display fonts are Times Roman and Symbol.

⊗*Printed on Southworth 20 lb. Parchment Deed, 100% cotton fiber paper.*